Structural investigation on molecular brushes

Strukturuntersuchung an molekularen Bürsten

Dissertation of

Jia-Jhen Kang

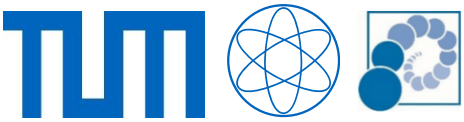

Technische Universität München
Physik-Department
Fachgebiet Physik weicher Materie

Supervised by
Prof. Christine M. Papadakis, Ph.D.

TECHNISCHE UNIVERSITÄT MÜNCHEN

Physik-Department, Fachgebiet Physik weicher Materie

Structural investigation on molecular brushes

Jia-Jhen Kang

Vollständiger Abdruck der von der Fakultät für Physik der Technischen Universität München zur Erlangung des akademischen Grades eines

Doktors der Naturwissenschaften (Dr. rer. nat.)

genehmigten Dissertation.

Vorsitzender:	Prof. Dr. David Egger
Prüfer der Dissertation:	1. Prof. Christine M. Papadakis, Ph.D.
	2. Prof. Dr. Christoph P. Hugenschmidt

Die Dissertation wurde am 26.05.2021 bei der Technischen Universität München eingereicht, und durch die Fakultät für Physik am 15.07.2021 angenommen.

Preface

The research presented in this thesis was conducted under the supervision of Prof. Dr. Christine M. Papadakis in the Soft Matter Physics Group at the Physics Department of Technical University of Munich.

The researches on the poly(oxazoline)-based molecular brushes (MBs) were carried out in collaboration with Prof. Dr. Rainer Jordan and Clemens Sachse in the Chair of Macromolecular Chemistry at the Faculty of Chemistry and Food Chemistry of Dresden University of Technology, Dresden, Germany, who performed the polymer synthesis and the turbidimetry measurements. For the MBs with poly(propylene oxide)-*co*-poly(ethylene oxide) side chains, the research was carried out in collaboration with Dr. Stergios Pispas and Dr. Junpeng Zhao in the Theoretical and Physical Chemistry Institute of National Hellenic Research Foundation, Athens, Greece, who performed the polymer synthesis.

The *cryo*-electron microscopy images were taken in the Laboratory for Biomolecular Design of Prof. Dr. Hendrik Dietz, at the Physics Department of Technical University of Munich, by Fabian Kohler. The small-angle neutron scattering (SANS) data were measured at beamline KWS-1 operated by the Jülich Centre of Neutron Science (JCNS) at the Heinz Maier-Leibnitz Zentrum (MLZ), Garching, Germany, with the support of Dr. Lester C. Barnsley. The small-angle X-ray scattering (SAXS) measurements were conducted at beamline P12 at the European Molecular Biology Laboratory (EMBL) at Deutsches Elektronen Synchrotron (DESY), Hamburg, Germany, with the support of Dr. Martin A. Schroer, Dr. Stefano Da Vela and Dr. Dmitry Molodenskiy.

For the analysis of the SAXS data, the structure factor in the fitting model, implemented in the software SASfit 0.94.12 [1], was programmed by Dr. Joachim Kohlbrecher in the Laboratory for Neutron Scattering and Imaging of Paul Scherrer Institute.

Abstract

Molecular brushes (MBs), being densely-grafted polymers, show physical properties that deviate from linear polymers due to their compact architecture. In this thesis, such effect is studied, focusing on their conformation-concentration relation and the thermoresponsive behavior in solutions. The tools used for this purpose are small-angle scattering (SAS), dynamic light scattering and *cryo*-electron microscopy. The structural details of the MBs under variation of temperature/concentration are traced and resolved.

Zusammenfassung

Molekular Bürsten (MBs) sind dichtgepfropfte Polymere und zeigen physikalische Eigenschaften, die aufgrund ihrer kompakten Architektur von linearen Polymeren abweichen. In dieser Arbeit wird ein solcher Effekt untersucht, wobei der Schwerpunkt auf ihrer Konformations-Konzentrations-Beziehung und dem thermoresponsiven Verhalten in Lösungen liegt. Die dafür verwendeten Werkzeuge sind Kleinwinkelstreuung (SAS), dynamische Lichtstreuung und *Kryo*-Elektronenmikroskopie. Die strukturellen Details der MBs unter Variation von Temperatur/Konzentration werden verfolgt und aufgelöst.

Contents

List of abbreviations

AFM	atomic force microscopy
DESY	Deutsches Elektronen Synchrotron
DLS	dynamic light scattering
EM	electron microscopy
EBML	European Molecular Biology Laboratory
FTIR	Fourier-transform infrared
JCNS	Jülich Centre of Neutron Science
LCST	lower critical solution temperature
MB	molecular brush
MLZ	Heinz Maier-Leibnitz Zentrum
SANS	small-angle neutron scattering
SAS	small-angle scattering
SAXS	small-angle X-ray scattering
SDD	sample-to-detector distance
SEC	size exclusion chromatography
SLD	scattering length density
SLS	static light scattering
P*b*E	$PHOS_{88}$-*g*-(PPO_{132}-*b*-PEO_{121})
PEO	poly(ethylene oxide)
PEtOx	poly(2-ethyl-2-oxazoline)
PHOS	poly(*para*-hydroxystyrene)
P*i*POx	poly(2-isopropenyl-2-oxazoline)
PNIPAM	poly(*N*-isopropyl acrylamide)
P*n*PrOx	poly(2-*n*-propyl-2-oxazoline)
PPO	poly(propylene oxide)
P*r*E	$PHOS_{143}$-*g*-P(PO-*ran*-EO)$_{157}$
UCST	upper critical solution temperature

List of symbols

$\approx$	approximately equal
$\sim$	proportional
$Đ$	polydispersity of molar mass
b	scattering length
b_K	Kuhn length
b_n	neutron scattering length
b_x	X-ray scattering length
C_h	structure coefficient
c	concentration
c^*	overlap concentration
D	translational diffusion coefficient
D_0	translational diffusion coefficient of infinite dilution
D_{avg}	average distance between MBs
$g_2(\tau,q)$	normalized intensity autocorrelation function
$g_1(\tau,q)$	normalized field autocorrelation function
$I(q)$	scattering intensity in dependence on momentum transfer
k_B	Boltzmann's constant
$\boldsymbol{k_i}$	incident wave vector
$\boldsymbol{k_s}$	scattered wave vector
L	cylinder length
L_c	contour length
L_{int}	interaction length
l_p	persistence length
M_n	number-average molar mass
M_w	weight-average molar mass
m	exponent of the Ornstein-Zernike structure factor
N	degree of polymerization
N_{bk}	degree of polymerization of the backbone
N_p	number of particles in the illuminated volume
N_{sc}	degree of polymerization of the side chains
n	refractive index
$p(r)$	pair distance distribution function
q	magnitude of scattering vector, i.e., momentum transfer
$\boldsymbol{q}$	scattering vector
R	cylinder radius
R_0	end-to-end distance of an ideal chain

R_c	cross-sectional radius
R_e	core equatorial radius
R_{ee}	end-to-end distance
R_p	core polar radius
R_F	end-to-end distance of a real chain
R_g	radius of gyration
R_h	hydrodynamic radius
$R_{h,0}$	hydrodynamic radius in infinite dilution
R_{HS}	hard-sphere radius
r	pair distance
$\boldsymbol{r}$	position vector
r_{int}	inter-particle distance
r_{max}	largest inner dimension
T	temperature
T_b	boiling temperature
T_{cp}	cloud point
T_e	shell equatorial thickness
T_p	shell polar thickness
t	time
$U(r_{int})$	potential energy
u_{ps}	interaction energy between a pair of polymer and solvent
u_{pp}	pairwise interaction energy of the polymer
u_{ss}	pairwise interaction energy of the solvent
V	illuminated volume (in DLS or SAS measurements)
V_p	particle volume
X	reduced concentration
z	grafting density
Γ	decay rate
ΔG_{mix}	Gibbs free energy of mixing
ΔH_{mix}	enthalpy of mixing
ΔS_{mix}	entropy of mixing
$\Delta\rho$	scattering contrast
α	Porod exponent
β	interaction factor
β^{coh}	coherence factor
$\gamma(\boldsymbol{r})$	spatial autocorrelation function
η	hard-sphere volume fraction
η_s	viscosity of solvent

2θ	scattering angle
λ	wavelength of the light source in vacuum
μ_2	second moment in the modified cumulant expression
μ_3	third moment in the modified cumulant expression
ξ	correlation length
ρ	scattering length density
ρ_c	scattering length density in the core
ρ_s	scattering length density in the shell
τ	delay time
τ_D	relaxation time
σ	standard deviation of Gaussian distribution
ϕ	polymer volume fraction
χ	Flory-Huggins interaction parameter

1. Introduction

Molecular brushes (MBs) are densely grafted polymers featuring a comb-like shape, as the polymeric main chain is grafted by the side chains with high grafting density [2-6]. By modifying the architectural parameters, e.g., the grafting density and the molar mass of the backbone and the side chains, the molecular structure of the MBs can be easily adjusted. Furthermore, by introducing functional segments to either the side chains or the end groups, the MBs can be designed to bear a wide range of properties and thus become potential candidates for particular applications. The versatile possibilities to add up desired functionalities, in combination with the significant progress on the synthesis strategies in the recent decade [7-10], have made them attractive candidates in diverse systems from drug delivery, antifouling, elastomers, photonic crystals to surface manufacturing [11-23].

Due to the highly-grafted architecture, both the backbone and the side chains of the MBs feature a rather stretched conformation, and the MBs have a compact structure. Their physical properties are thus found to be different from the properties of their linear analogues. Since a better understanding on the changed properties by the compact structure is necessary to facilitate their application in practical use, investigations about the effects of the architectural parameters on the physical behavior of MBs are widely reported. These include the dynamics of the side chains, the conformational behavior in solutions and in melts, and the physical behavior with responsive polymeric segments [24-36].

A solution behavior of MBs that attracts fundamental interests is their conformation evolution with increasing polymer concentration, i.e., with an enhanced mutual interaction between MBs. In dilute solutions, the MBs interact by their full dimension, i.e., the backbone length, and the interaction therefore follows the rules as for linear polymers. When the concentration increases to semi-dilute condition, the interaction at smaller segmental length scales, e.g., the persistence length or the side chain length, dominates, making their solution behavior deviates from the linear polymer solution systems. Based on the molecular architecture, predictions have been made by theoretical and simulation work in terms of the relation between the end-to-end distance R_{ee} of the MBs and the solution concentration c [37, 38], where R_{ee} and c display scaling behavior in double-log plots with different scaling

exponents in distinct interaction regimes. As for experimental work, there are only few studies on this topic, where the conformation of the MBs is characterized by small-angle scattering (SAS) at varying solution concentration [32, 39, 40]. This concerns the analysis of SAS data using appropriate models for the scattering of the MBs as well as the scattering of the mutual interaction between the MBs. For MBs with short backbone, the mutual interaction in SAS could be described by the simple correlation scattering, e.g., the hard-sphere structure factor; whereas for MBs with long backbones, the simple correlation model is invalid, as the MBs resemble large linear polymers with rigid main chain. In this case, i.e., for long MBs, the inter-correlation is supposed to depend on the conformation of the MB itself. While a proper description of the correlation scattering would facilitate a much better understanding on the conformation of MBs and their mutual interactions, this, however, has not been realized by any of the experimental work using SAS to the best of our knowledge.

Another interesting topic about the solution behavior of MBs is their thermoresponsive property, when they are composed of segments with lower critical solution temperature (LCST) behavior. Compared to linear polymers, MBs with LCST segments show a lowered phase transition temperature due to the compact structure. Furthermore, their thermoresponsive behavior is found tunable by the arrangements of the side chains on the backbone, the composition of the side chains and the architecture of the side chains when the side chains are copolymers [41, 42]. Thus, a series of studies on thermoresponsive MBs have been delivered by research groups, in the attempt to understand the impact from the complex structure while aiming for a controllable phase transition process. In most of the studies, this is characterized by the transition temperature, where the MB solutions turns from one-phase to two-phase state upon heating. It is measured by turbidimetry, which records the transmission of the solution versus temperature, and the cloud point T_{cp} is determined to be the transition temperature where the transmission shows a drastic drop. To further gain information about the transition process, in some studies, the hydrodynamic size of the MBs is measured using dynamic light scattering (DLS), which is a quick and efficient method to monitor the size-dependence of MBs on temperature. It provides an indirect proof to the conformational change of the thermoresponsive side chains, ether chain collapsing or expanding. However, using turbidimetry and DLS, the information is limited to the resulting transition temperature and an overall hydrodynamic size of the MBs, respectively, while a detailed picture of the process of the phase transition in terms of the inner structural variation is necessary for a deeper understanding on the thermoresponsive behavior. Moreover, from the above-mentioned two techniques, the information regarding the

two-phase state, i.e., the micro phase separation behavior and the structure of the aggregates, are unavailable due to the high opacity of the solutions. Thus, there are unclear parts in the thermoresponsive process in the one-phase state, and the aggregation behavior in the two-phase state of MB solutions is also left unsolved.

In the present thesis, a series of structural investigations on MBs are delivered, focusing on the concentration-conformation relation and the thermoresponsive behavior of MBs in solutions. The main techniques used are small-angle X-ray scattering (SAXS) and small-angle neutron scattering (SANS). By model fitting the SAXS/SANS data, detailed information on the inner structure of the MBs is revealed, providing a deeper understanding on their physical properties. Besides, complementary information is obtained from DLS, giving the diffusional behavior and the hydrodynamic size, and *cryo*-electron microscopy, making images of the MBs in real space available.

The thesis is organized in the following manner: the background knowledge about MBs is introduced in chapter 2, with a brief literature review on the concentration effect and the thermoresponsive behavior in solutions. In chapter 3, the strategy of the present work is given, with the specific systems under investigation. In chapter 4, the basic principles of the experimental techniques used are described, with a focus on the situations for measurements on MB solutions. Later, from chapter 5 to chapter 7, experimental results are presented and discussed, which is followed by a summary and outlook in chapter 8.

2. Background information

In this chapter, the background knowledge for the present thesis is given. In the first section, the concentration effect on the chain size of linear polymers as well as the thermodynamics of polymer solutions are briefly explained. Subsequently, molecular brushes (MBs) are introduced. Next, the concentration effect for MBs in solutions is discussed with both the theoretical point of view and the experimental results. Later, a literature review on the thermoresponsive behavior of MBs exhibiting the lower critical solution temperature (LCST) behavior in aqueous solutions is given, focusing on the structural variation of the MBs.

2.1 Polymer solutions: chain size and thermodynamics

Polymers are macromolecules consisting of repeating elementary units, called monomers, which are covalently bonded together. The total number of monomers along the polymer chain is referred to as the degree of polymerization, *N*. When the monomers are chemically of the same type, the polymer is called homopolymer. In cases when there are two or more types of constituent monomers, the polymer is called copolymer. In copolymers, the different types of monomers could be arranged in a block sequences, gradient sequence, or random sequence, resulting in different chain architecture, as shown schematically in Figure 2.1.

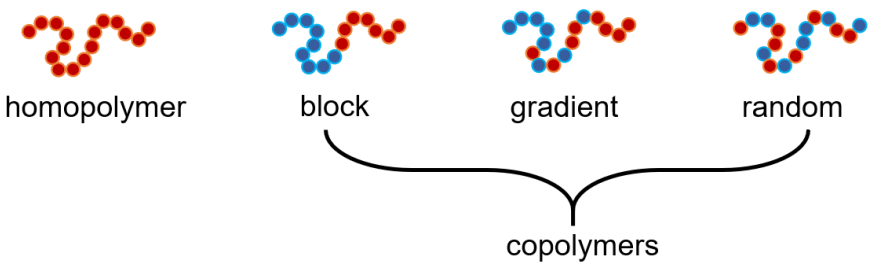

Figure 2.1 Schematic representation of homopolymer and copolymers with different arrangements of the monomer sequences. The circles indicate individual monomers, where the red and blue colors indicate the two different types of monomers.

2.1.1 Polymer chain size in solutions

As dissolved in a good solvent at low concentration, polymer chains are far apart and isolated from each other (Figure 2.2a). Their confirmation is described by the self-avoiding walk model, resulting in a fractal structure in space with a fractal dimension of 5/3 ≈ 1.67 [43, 44]. The chains are swollen in the solution, and the end-to-end distance R_{ee} is predicted by the Flory theory to be the one of the real chain, R_F:

$$R_{ee} = R_F \approx b_K N^{0.6} \text{ for } c < c^* \tag{2.1}$$

where b_K is the Kuhn length of the polymer. With increasing polymer concentration c, R_{ee} is unchanged with c until the polymer chains begin to overlap. This is called the overlap concentration c^*, above which the polymer chains are space-filling and interpenetrating (Figure 2.2b). The concentration dependence of R_{ee} was derived by de Gennes scaling theory as [45]:

$$R_{ee} \approx b_K N^{0.5} c^{-0.12} \text{ for } c^* < c < c^{**} \tag{2.2}$$

Thus, R_{ee} decreases upon increasing c, until the chain conformation shrinks to the one of an ideal chain at c^{**}, $R_{0:}$

$$R_{ee} = R_0 \approx b_K N^{0.5} \text{ for } c > c^{**} \tag{2.3}$$

Namely, above c^{**}, the polymer chains feature a conformation as in theta solvent (Figure 2.2c). Based on the description above, the dependence of R_{ee} on c is drawn in Figure 2.2d for linear polymers, where R_{ee} shows a scaling relation with an exponent of -0.12 between c^* and c^{**}.

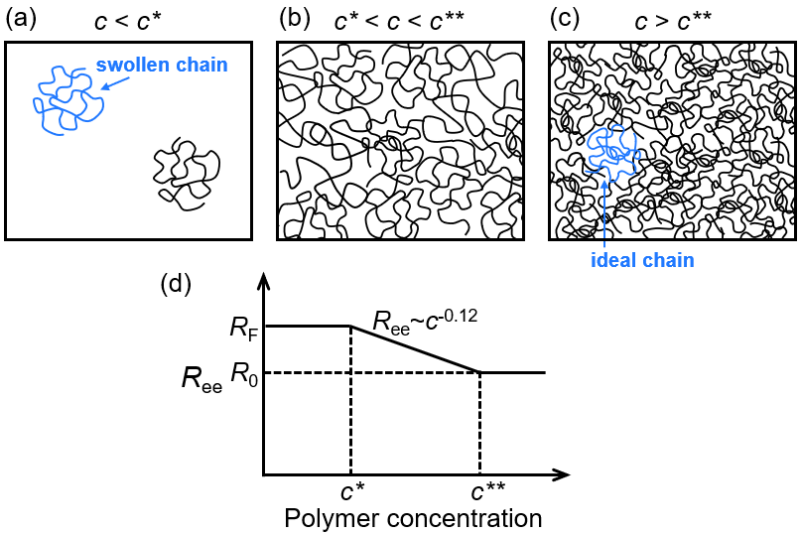

Figure 2.2 Schematic representation of polymer solutions in good solvent in (a) dilute (b) semi-dilute and (c) concentrated solutions. (d) The relation between R_{ee} and the polymer concentration accordingly.

2.1.2 Thermodynamics of mixing

For polymer solutions, the stability and the thermodynamic equilibrium state is governed by the free energy of mixing of the polymer with the solvent. By Flory-Huggins theory, the Gibbs free energy of mixing, ΔG_{mix}, contributed by an enthalpic and an entropic term, can be expressed as a function of the polymer volume fraction ϕ [46]:

$$\Delta G_{mix} = \Delta H_{mix} - T\Delta S_{mix} \tag{2.4}$$

$$\Delta G_{mix} = k_B T[\frac{\phi}{N}\ln\phi + (1-\phi)\ln(1-\phi) + \chi\phi(1-\phi)] \tag{2.5}$$

where ΔH_{mix} is the enthalpy of mixing, ΔS_{mix} is the entropy of mixing, and T is the absolute temperature. k_B is Boltzmann's constant and χ is the Flory-Huggins interaction parameter. The first and the second term in equation 2.5 originate from ΔS_{mix}, giving always negative contributions to ΔG_{mix}. The third term originates from ΔH_{mix}, and it could give positive or negative contribution to ΔG_{mix}, depending on the sign of χ. By definition, χ is characterized by the differences of interaction energy between the species in the system, i.e., the polymer and the solvent, and is dependent on T, as:

$$\chi \sim \frac{(2u_{ps} - u_{pp} - u_{ss})}{k_B T} \tag{2.6}$$

where u_{ps} is the interaction energy between a pair of polymer and solvent molecules, u_{pp} is the pairwise interaction energy of the polymer, and u_{ss} is the pairwise interaction energy of the solvent. Thus, χ provides indication to the question whether the two species have higher affinity to their own kind, or they like to stay with the other kind.

At a given T, the concentration-dependent curve of ΔG_{mix} shows convex curvature at both dilute and concentrated regimes and concave curvature at intermediate concentrations, as shown in Figure 2.3a. When the polymer solution has concentrations above or below the two local minima, i.e., $c < c'$ or $c > c''$, the system is thermodynamically stable, as it stays at the lowest free energy at the corresponding concentration. On the other hand, solutions with concentrations between c' and c'' are not stable as mixtures, as a lower free energy can be reached by a decomposition of the solution. In $c' < c < c''$, the unstable regime and the meta-stable regime are further defined by the two inflection points, c_{sp1} and c_{sp2}. Within $c_{sp1} < c < c_{sp2}$, the second derivative of ΔG_{mix} is negative, and any small fluctuations in concentration could induce a decomposition. Thus, the system is unstable, and such phase separation is called spinodal decomposition. In the concentration range of $c' < c < c_{sp1}$ and $c_{sp2} < c < c''$, the solution stays homogeneous under small concentration fluctuation, while it could phase separate when large concentration fluctuation occurs. Under this circumstance, the system is considered meta-stable, and the phase separation is called binodal decomposition. With c_{sp1}, c_{sp2}, c' and c'' values determined in dependence on T, phase diagram of polymer solutions is constructed, where the one-phase (stable), meta-stable, and the two-phase (unstable) regions are separated by the spinodal and the binodal curves, as demonstrated in Figure 2.3b.

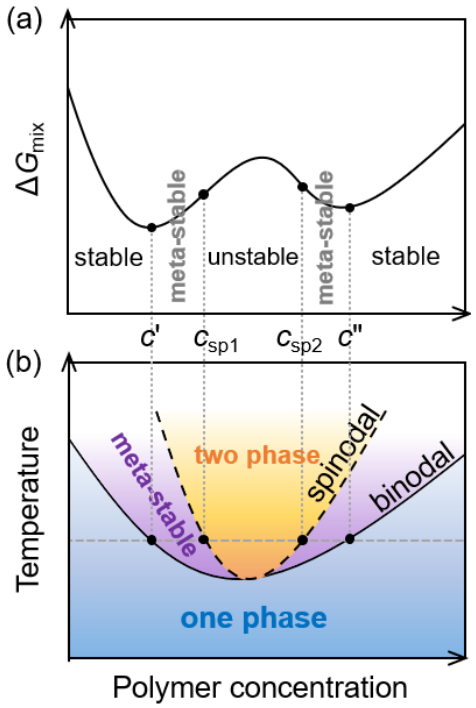

Figure 2.3 (a) Free energy of mixing, ΔG_{mix}, of polymer solutions in dependence on concentration, with the two local minima, *c*' and *c*", and the inflection points, c_{sp1} and c_{sp2}. (b) The corresponding phase diagram constructed by *c*' and *c*" (the spinodal curve, dashed line) and c_{sp1} and c_{sp2} (the binodal curve, solid line) at different temperatures.

As indicated by equation 2.6, the interaction between polymer and solvent leads to different temperature-dependence of χ. This results in two different thermoresponsive behavior of polymers in aqueous solutions: one is called the upper critical solution temperature (UCST) behavior and the other the lower critical solution temperature (LCST) behavior. The solubility of the two kinds of polymers react to the variation of temperature inversely, which often reflects on the polymer chain conformation.

For UCST-type polymers, $(2u_{ps} - u_{pp} - u_{ss}) > 0$, meaning χ decreases with increasing *T*. Thus, they feature low solubility at low temperatures, and become fully soluble as temperature is increased. A typical phase diagram of the UCST polymer is shown in Figure 2.4a, with the binodal curve splitting the diagram into the two-phase and the one-phase region. In the two-phase state, polymer-polymer interaction is favored, so the chain conformation is collapsed; whereas in the one-phase state, polymer-water interaction is favored, so the chain is swollen by water molecules. Therefore, upon increasing temperature, the polymer chain undergoes a conformational transition from globule-like to coil-like, as depicted in Figure 2.4a. The phase transition temperature is often determined experimentally by measuring the transparency of the

solution, which turns turbid in the two-phase region due to the formation of aggregates. The temperature where a drastic change in the transmission occurs is determined to be the phase transition temperature, referred to as the cloud point T_{cp}.

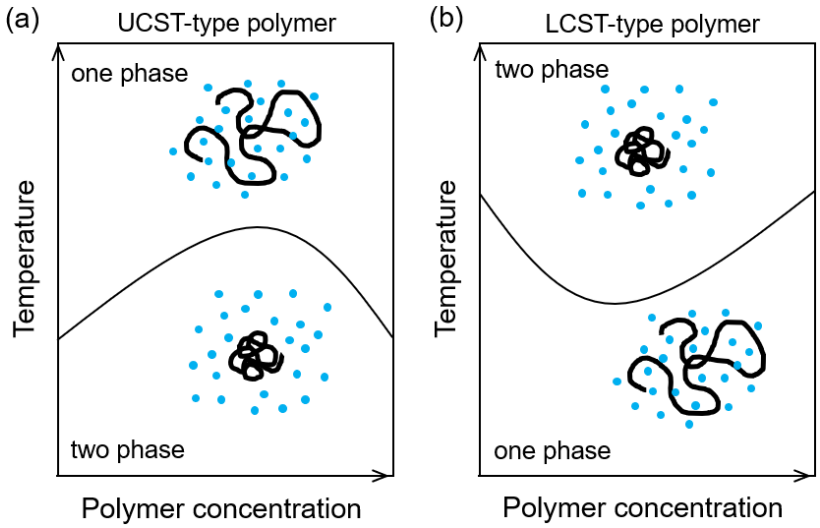

Figure 2.4 Typical phase diagrams of polymer solutions exhibiting the (a) UCST behavior and the (b) LCST behavior, where the diagrams are separated into the one-phase region and the two-phase region by the binodal curves (solid lines). The cartoons in the diagrams demonstrate the confomation of polymer chains (black curled lines) and the water molecules (blue dots).

Opposite to the UCST-type polymers, $(2u_{ps} - u_{pp} - u_{ss}) < 0$ for LCST-type polymers, meaning χ increases with increasing T. Thus, they are soluble in water at low temperatures, and their solubility decreases as the temperature is increased. A typical phase diagram is shown in Figure 2.4b. The decrease of solubility upon heating is due to the unfavorable positive entropy contribution to ΔG_{mix} from the H-bonding between water and polymer, which becomes dominant at high temperatures [47]. Thus, with increasing temperature, the polymer-water interaction is weakened, while the polymer-polymer interaction becomes more favorable. As a result, water molecules are released from the polymer during heating, and the polymer chains gradually contract and collapse. At T_{cp}, the dehydration induces a coil-to-globule conformational transition of the polymer chain [48, 49], and the transparency of the aqueous solution shows a significant decrease [50].

2.2 Molecular brushes (MBs)

MBs are composed of a backbone and numerous polymeric side chains [2-4, 6]. Due to the high grafting density, the steric hindrance between the side chains results in a high stiffness of the backbone, compared to the bare linear polymers, and a stretched conformation of both the backbone and the side chains, as schematically shown in Figure 2.5. The architecture of MBs is characterized by the degree of polymerization of the backbone, N_{bk}, the degree of polymerization of the side chains, N_{sc}, and the grafting density, z, defined as the number of side chains grafted on each backbone monomer. z is generally larger than 0.5.

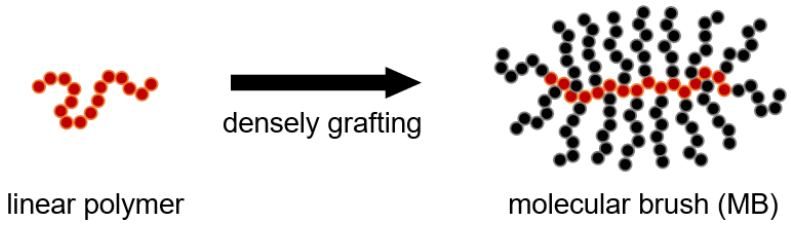

Figure 2.5 Schematic representation of the variation of the chain conformation from a linear polymer to a MB via the dense grafting of the side chains. The red circles represent the monomers of the backbone, while the black circles are those of the side chains.

While the high grafting density leads to a comb-like shape, changing the relative length ratio between the backbone and the side chains leads to various molecular structures (Figure 2.6) [51-53], which can be characterized experimentally. When the side chains are much longer than the backbone, the MB has a structure close to the one of a star-like polymer and therefore assumes a spherical or ellipsoidal shape. In contrast, when the backbone is significantly longer than the side chains, the NB resembles a large worm-like chain. Rich studies addressing the relation between the architectural parameters and the conformation of MBs have been reported in terms of theoretical predictions [37, 54], simulations [38, 55-63] and experimental results [64-67].

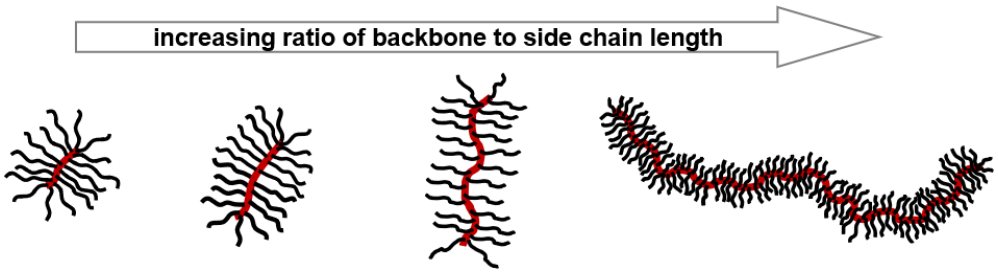

Figure 2.6 Schematic representation of the various structures of MBs, by adjusting the length ratio between the backbone and the side chains. The red lines represent the backbones, and the black lines the side chains.

Because of the compact structure and the stretched conformation, the physical properties of MBs usually deviate from the ones of their linear analogues, for example, the responsive properties, concentration effects, crystallization behavior, conductivity and modulus, which furthermore depend on the architecture of the MBs. In the present thesis, two aspects are focused on: the concentration effect on the MB conformation, and the thermoresponsive behavior of MBs having LCST-type side chains. The background knowledge on the two topics is given in the following sections.

2.3 Concentration effects on MBs in solutions

Since the structure of MBs resembles a large linear polymer chain with a finite cross section [68-70], especially for MBs with long backbone, their structure is often characterized by parameters that are used for linear polymers chains. As schematically depicted in Figure 2.7a for linear polymers, the contour length L_c is the total length of the chain, and the persistence length l_p is the segmental length below which the chain features a stiff rod, serving as a measure of the chain stiffness. (l_p is linked to b_K by $b_K = 2l_p$). For MBs, as shown in Figure 2.7b, L_c and l_p can be determined, where l_p of MBs is typically larger than the value of linear polymers due to the enhanced backbone rigidity by the high grafting density. Besides, the densely-grafting side chains form a cross section perpendicular to the chain longitudinal direction, and the cross-sectional radius R_c can be estimated by theoretical prediction [71], or experimentally determined using X-ray or neutron scattering [67, 72, 73].

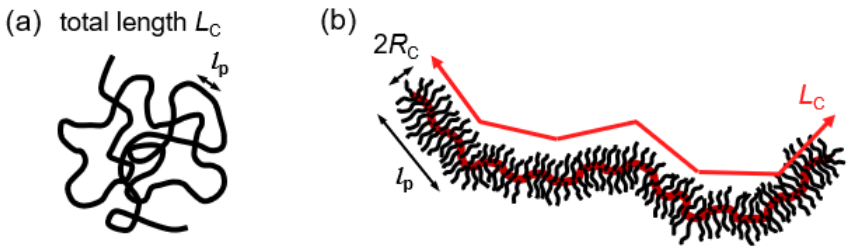

Figure 2.7 Schematical representation of (a) linear polymer and (b) MB, shown along with the structural parameters including the contour length L_c, the persistence length l_p and the cross-sectional radius R_c.

Due to the similarity to linear polymers, the conformational behavior of MBs in solutions is predicted and compared with the one of linear polymers in theoretical and simulation work. The theoretical work by Borisov et al. addresses the relation between the end-to-end distance R_{ee} of MB and the solution concentration c, from dilute to semi-dilute to concentrated solution [37]. In this study, extensive parameters are considered, including the solvent quality for the backbone and the side chains, the molar mass of the backbone and the side chains and the grafting density of the MB. In dilute solutions, the MBs assume their unperturbed conformation, which stays unchanged with increasing concentration, until the overlap concentration c^* is reached. Above c^*, the mutual interaction affects the conformation of the MBs, and quantitative scaling laws between R_{ee} and c are predicted according to the dominant mutual interaction. When the solvent quality is good for both the backbone and the side chains, right above c^*, the interaction between the backbones dominates, and the scaling relation of $R_{ee} \sim c^{-0.125}$ is valid, which is the same as for linear polymers in solutions. Upon further increasing the solution concentration, the interaction between the side chains is involved, and a scaling relation of $R_{ee} \sim c^{-0.304}$ is predicted in this second regime. Since the interacting length scales decrease to the level of the local segmental lengths, the persistence length l_p as well as the cross-sectional radius R_c are both predicted to depend on concentration. Thus, in the second interaction regime, the rigidity of the backbone and the side chains, which are of stretched conformation at dilute condition, gradually decreases with increasing concentration. Finally, in the last interaction regime, R_{ee} does not show dependence on concentration, with both the backbone and the side chains featuring Gaussian conformation as ideal chains.

In the simulation work by Paturej and Kreer, similar findings as in the theoretical work [37] are reported, with a detailed description on the different regimes of mutual interactions between MBs in good solvent [38]. Figure 2.8a shows the relation between R_{ee}^2 and c, where

four interaction regimes are defined above the overlap concentration $c^* = c_1$: (1) the backbone interaction regime, yielding $R_{ee} \sim c^{-0.125}$, (2) the persistence length interaction regime, yielding $R_{ee} \sim c^{-0.25}$, (3) the inter-side chain interaction regime, yielding $R_{ee} \sim c^{-0.308}$ and (4) the inter- and intra- side chain interaction regime, yielding $R_{ee} \sim c^{-0.4}$. In regimes (3) and (4), the term "inter-" refers to the interaction between side chains on the adjacent MBs, while the term "intra-" refers to the interaction between side chains grafted on the same MB. Thus, in addition to regime (1), where the MBs behave like linear polymers, three more regimes accounting for the mutual interactions on subsequently smaller length scales are recognized for MBs, which are shown schematically in Figure 2.8a.

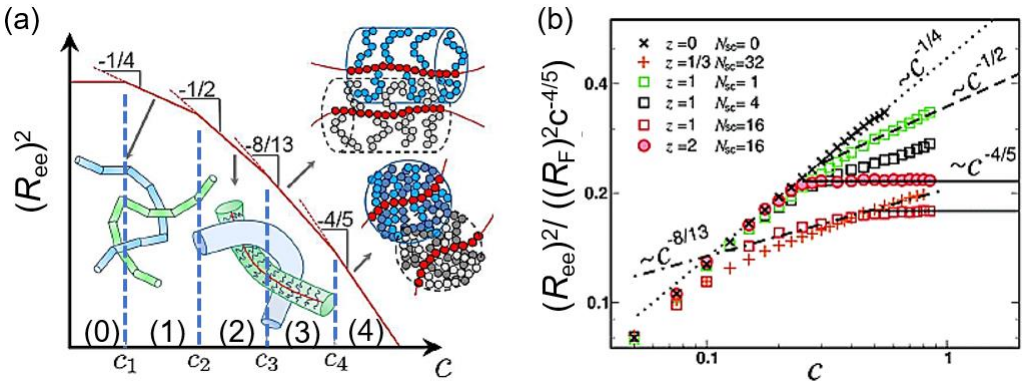

Figure 2.8 (a) Dependence of R_{ee}^2 on concentration c for MB solutions, as predicted theoretically, shown in double-logarithmic scaling. (b) R_{ee}^2 of MB, normalized by the value in dilute solution R_F^2 and $c^{-4/5}$, as a function of c. Lines represent theoretical scaling laws for R_{ee}^2 in the corresponding regime that are defined in (a): regime 1 (dotted), regime 2 (dashed), regime 3 (dash-dotted) and regime 4 (solid). Data are shown for MBs with different N_{sc} and z, as indicated in the legend, while N_{bk} is fixed to 100. Reprinted with permission from ref [38]. Copyright (2017) Royal Society of Chemistry. The numbers of regimes are marked by the author of the present thesis for a better understanding.

In the same work by Paturej and Kreer, the role of the architectural parameters, i.e., N_{sc} and z, on the relation between R_{ee} and c is demonstrated by several examples [38]. In one extreme case, where N_{sc} is set to be 1 (Figure 2.8b, green open squares), the relation of R_{ee} vs. c shows the behavior of regime 1 followed by regime 2, which lasts to higher concentration. Namely, no interaction between side chains is observed in this case, presumably due to the very short side chain length. In another case, z is set to 2 and N_{sc} is 16 (Figure 2.8b, red filled circles), the relation of R_{ee} vs. c the shows the behavior of regime 1 directly followed by regime 4, while

regime 2 and regime 3 are skipped. This is explained by the high grafting density combined with the long side chains, resulting in the dominant side chain interaction between MBs. From these simulation results, it is revealed that, the occurrence of each interaction regime depends heavily on the MB architecture.

As for experimental studies, in dilute solutions, the MB conformation can be resolved using small-angle scattering (SAS), and the relation between the architectural parameters and the conformation has been widely investigated [64-66, 74-76]. In SAS data, different length scales in real space are reflected in different ranges of momentum transfer q. The flexible cylinder model is usually used, giving structural parameters of L_c, l_p and R_c. However, the structural behavior of MBs upon varying concentration is much less studied. One of the challenges arises from modeling the SAS data, since the data in semi-dilute solutions concern the interplay between several length scales, including the ones within a MB as well as the correlation lengths between MBs, making it difficult for the fitting software to determine the parameters distinctively [77]. Furthermore, it is another challenge to precisely describe the scattering coming from the mutual interaction in the SAS data. As indicated by theoretical and simulation work, the conformation of individual MBs changes with polymer concentration in semi-dilute solutions, and their correlation might need to be altered correspondingly to address such conformational evolution, which has not been considered in any of the related work yet.

In the work by Bolisetty et al., the conformation of a long MB (N_{bk} = 1600, N_{sc} = 61) was traced from dilute to semi-dilute solution in a good solvent [39, 40], using small-angle neutron scattering (SANS). The scattering of the MBs was modeled by the flexible cylinder form factor. The scattering from the mutual interaction was described by a viral series of c, which has been proved applicable for systems like flexible polymers, anisotropic particles and dendrimers [78-85]. Despite of the limited number of data points, the radius of gyration, R_g, of the MBs was found to follow the theoretical prediction by Borisov et al., showing firstly $R_g \sim c^{-0.125}$ and subsequently $R_g \sim c^{-0.304}$ upon increasing solution concentration. Meanwhile, l_p of the MBs steadily decreases, implying a decreasing stiffness of the backbone.

Sunday et al. also investigated the scaling relation between R_g and c in a good solvent using SANS, covering a broad range of concentration. To avoid the ambiguity raised from the overlapping length scales to the SANS analysis results, the data were described by the generalized Guinier-Porod model [86]. This allowed a precise determination of the radii of gyration in the longitudinal direction ($R_{g,2}$) and the perpendicular direction ($R_{g,1}$) of the anisotropic MB (Figure 2.9), whereas the exact values of the overall R_g and the structural

parameters (l_p and R_c) were calculated therefrom. As for the mutual interaction between MBs, the Percus-Yevick hard-sphere structure factor was used, which is the simplest correlation model for interacting particles. From dilute to semi-dilute condition, three interaction regimes are distinguished, from $R_g \sim c^{-0.11}$ to $R_g \sim c^{-0.35}$ and $R_g \sim c^{-0.10}$ at the highest concentration. Thus, compared to the experimental studies by Bolisetty et al. and the theoretical prediction by Paturej and Kreer, different scaling exponents for the interaction regimes were found. Plotting $R_{g,2}/R_{g,1}$ against c, it was found that the overall shape of the MBs become less anisotropic upon increasing concentration, which corresponds well to the decreasing rigidity of the backbone at high concentrations found by Bolisetty et al.

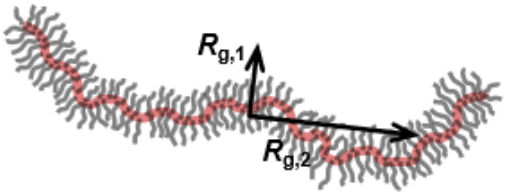

Figure 2.9 Schematical representation of a MB, where the structure is characterized by the radii of gyration in the longitudinal direction ($R_{g,2}$) and the perpendicular direction ($R_{g,1}$).

Although rich and interesting experimental observations about the concentration effect on the MB conformation have been reported as discussed in the previous paragraphs, the idea that the mutual interaction between MBs may depend correspondingly on the conformation of individual MBs has not yet been realized in the SAS data analysis. Namely, the scattering contribution from the MB interaction should include the conformational information from the scattering of the individual MBs in the fitting model, in order to account for the conformational evolution upon variation of the solution concentration.

2.4 Thermoresponsive MBs

When LCST polymers are grafted on a backbone polymer with a high grafting density, a MB exhibiting LCST behavior is obtained. It also undergoes an overall dehydration as the temperature is increased, accompanied with a phase transition. The dehydration mechanism of MBs with LCST side chains is investigated in the study by Zhou et al., using Fourier-transform infrared (FTIR) spectroscopy, and the results show that a large fraction of water is expelled out

of the MBs upon heating, attributed to the increased intra-molecular association [87]. Regarding the transition temperature of MBs in aqueous solutions, there could be two scenarios: the side chains belong to the so-called type 1 LCST, or they belong to the type 2 LCST. In the former situation of type 1 LCST, T_{cp} of the side chain polymer is strongly dependent on the molar mass and the solution concentration, for example, poly(2-ethyl-2-oxazoline) (PEtOx) [88-90], poly(ethylene oxide) (PEO) [91, 92] and poly(propylene oxide) (PPO) [93]. In this case, T_{cp} of the MB solutions will be suppressed from the one of the linear side chains due to the compact architecture. This phenomenon was reported by Zhou et al. [87] and by Weber et al. [94], where the MBs under investigation have poly(oxazoline)-based side chains. In the latter case of type 2 LCST, T_{cp} of the side chain polymer is unchanged in a wide range of molar mass and concentrations, and the most famous example is poly(*N*-isopropyl acrylamide) (PNIPAM), which typically shows $T_{cp} \approx 32$ °C for its aqueous solutions [95, 96]. In the studies by Li et al. [97] and by Li et al. [98], where the MBs under investigation have PNIPAM side chains, despite of the largely different molecular architecture, T_{cp} of the MB aqueous solutions were found to be around 32 °C, meaning T_{cp} is not influenced by the compact structure of MB.

For the structural variation of thermoresponsive MBs, the coil-to-globule transition as seen in linear polymer solution is not easily possible. Since the molecular structure of MBs is determined by the architectural parameters, namely the backbone length and the side chain length [64, 74-76, 99-101] (Figure 2.6), this further influences the structural evolution of MBs with LCST side chains.

When the MBs have a long backbone and short LCST side chains, upon heating, the structure changes from a worm-like shape to a globular shape, which is very similar to the observation on the conformational transition of LCST-type linear polymers. In this case, the side chains are so short that they do not hinder the coiling of the long backbone, thus the hydrophobicity at high temperatures leads to the collapse of the whole MB. In the work by Li et al., the shape change of a long MB (N_{bk} = 558 and N_{sc} = 13) with LCST side chains was investigated using atomic force microscopy (AFM) and light scattering [97]. In the AFM images, the MBs are worm-like below T_{cp} (Figure 2.10a), while they feature a spherical shape above T_{cp} (Figure 2.10b). Thus, it is concluded that the MBs exhibit a cylinder-to-globule transition upon heating. This is further supported by the light scattering measurements, where the hydrodynamic radius R_h and the radius of gyration R_g of the MBs in aqueous solutions were traced upon increasing temperature, showing a gradual decrease followed by a sharp drop at T_{cp} (Figure 2.10c). Such shape transition is also reported in a similar system of a long MB having

short pH-responsive side chains by Nese et al., where a cylinder-to-globule shape transition is induced by a change in the pH value of the MB solution [24].

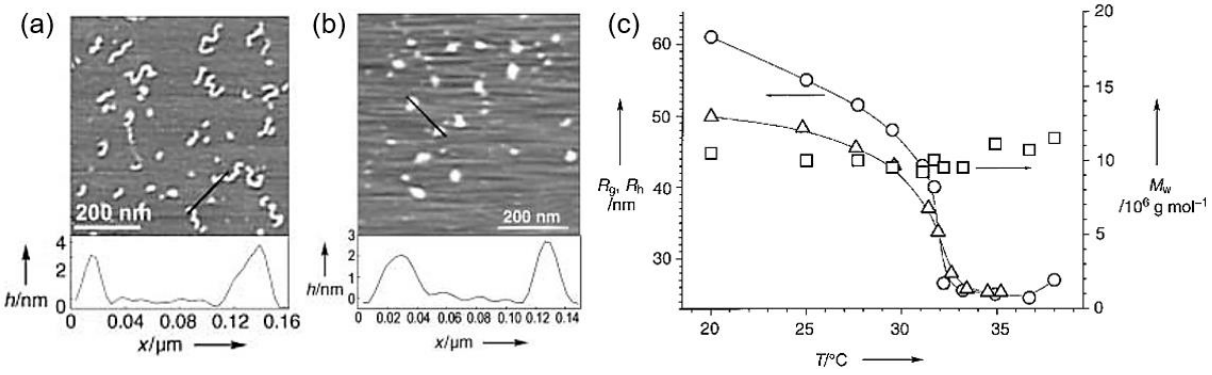

Figure 2.10 AFM images of the MB with PNIPAM side chains in water at (a) 20 °C and (b) 38 °C. (c) R_g (triangles, left axis), R_h (spheres, left axis), and weight-average molar mass M_w (squares, right axis) as a function of T, obtained by light scattering. The solid lines serve as guidance to the eye. Reprinted with permission from ref [97]. Copyright (2004) John Wiley and Sons.

When the backbone and the LCST side chains are of similar lengths, the size of MB hardly changes with temperature. It is reported in the work by Li et al. [98], where the structure of two MBs having similar degrees of polymerization for the side chains and the backbone was investigated using SANS (Figure 2.11a for P(4K-PNIPAM) with N_{bk} = 39 and N_{sc} = 31, and Figure 2.11b for P(6K-PNIPAM) with N_{bk} = 36 and N_{sc} = 45). The analysis results show that their size hardly changes upon variation of temperature (Figure 2.11d). This is supposedly due to the dense MB central region, which limits the contraction of the side chains above T_{cp}. In the same work, another MB with the backbone much longer than the side chains (P(9K-PNIPAM) with N_{bk} = 33 and N_{sc} = 73) was investigated (Figure 2.11c), and a steady decrease in the size upon increasing temperature was observed (Figure 2.11d). Such shrinkage of MB was attributed to the collapse of the side chains above T_{cp}, which is possible due to the larger space at the periphery region of the MB.

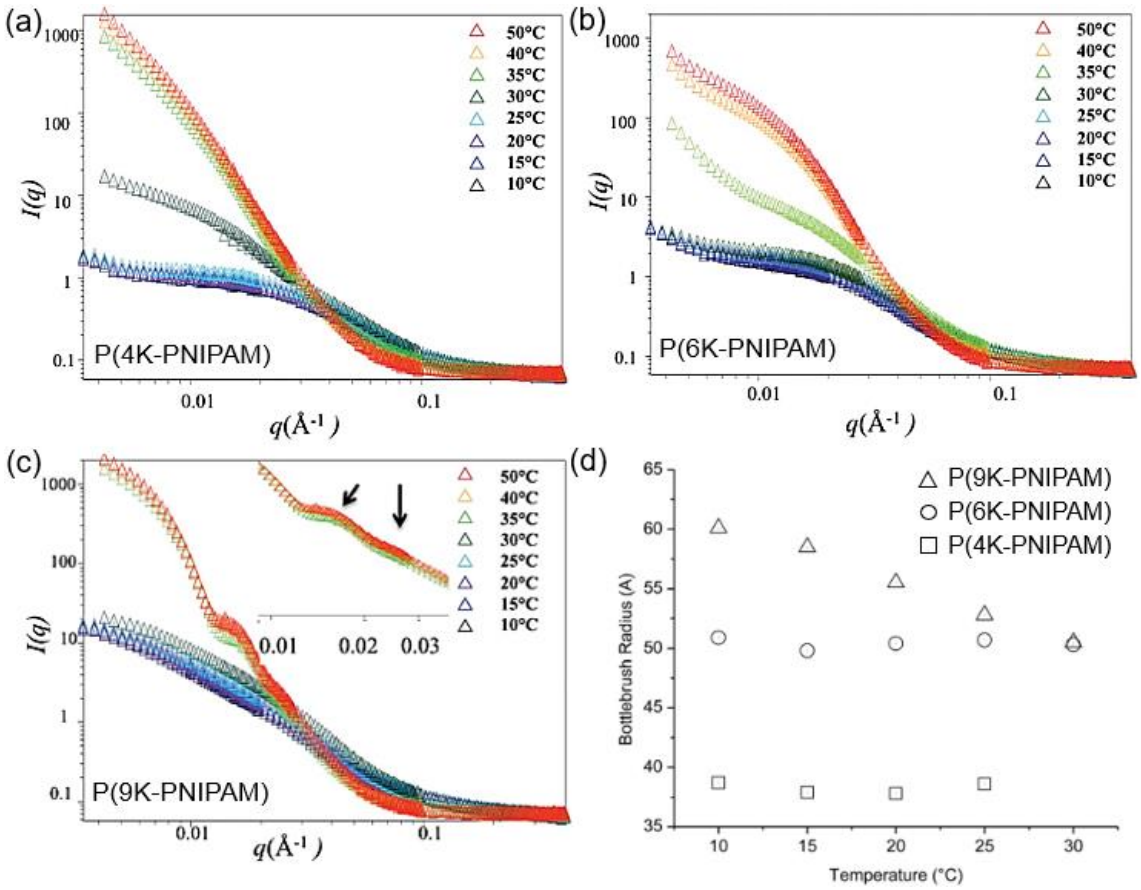

Figure 2.11 Temperature-resolved SANS data of 1 wt% solutions in D_2O for (a) P(4K-PINPAM), (b) P(6K-PNIPAM) and (c) P(9K-PNIPAM). (d) Radius of the MB obtained from model fitting from 10 °C to 30 °C. Reprinted with permission from ref [98]. Copyright (2014) Royal Society of Chemistry. The sample names are added by the author of the present thesis for a better understanding.

Based on the above-mentioned studies, the structural changes of MBs with LCST side chains are summarized schematically in Figure 2.12. With long backbone and short side chains, the increasing hydrophobicity upon heating leads to an overall collapse of the MB (Figure 2.12a). With similar lengths of the backbone and the side chains, the collapse of the side chains is hindered by the high density around the backbone region, and thus the LCST behavior is hardly reflected on a change in size (Figure 2.12b). When the side chain is longer than the backbone, the collapse of the side chains is significant, thus a shrinkage of the MB can be detected upon heating (Figure 2.12c).

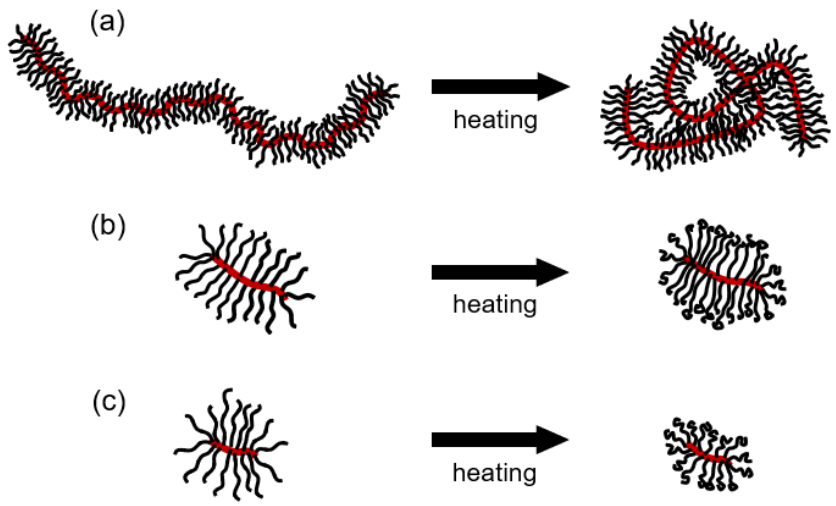

Figure 2.12 Schematic representation of the structural change of MBs with LCST side chains (red curled line: the backbone; black curled lines: the side chains). The arrows indicate the heating process. (a) MBs with long backbone and short side chains (b) MBs with similar backbone and side chain lengths. (c) MBs having shorter backbone than the side chains.

2.4.1 Copolymer side chains with LCST behavior

For MBs with LCST side chains, the temperature-dependent structural variation is influenced not only by the molecular architecture, as described in the previous paragraphs, but also by the side chain architecture. This is similar to the principle that different architectures of thermoresponsive linear copolymers, i.e., random- , gradient- or block- copolymer, will result in different phase transition behavior [102-106]. Thus, when the side chains are copolymers, where one or both of the components are of LCST-type, the behavior of the MB depends on the monomer sequence in the side chains.

For MBs with random copolymer side chains, composed of LCST polymers, it is reported in several work that the MBs exhibit the intermediate characteristics of the constituent components [41, 42, 107], as T_{cp} of their aqueous solution can be easily tailored by altering the composition of the constituents on the side chains. In the systems investigated by Yamamoto et al. [41] and Zhang et al. [42], T_{cp} shows an almost linear dependence on the composition of the LCST constituents, which hints at the ease of the tunability. The observation implies that, the physical properties of MBs with random copolymers follow the general principle of random copolymerization of monomers with different properties, resulting in a polymer exhibiting a

mixed property [108].

As for MBs with block copolymer side chains of LCST-type, the behavior of the MBs reflects the properties of both the constituent blocks. Regarding T_{cp}, in the work by Yamamoto et al. [41] and Zhang et al. [42], it was found to be either the same or close to T_{cp} of the outer polymeric block. This is considered to be a result from the dominant interaction between the outer block and aqueous environment. In the work by Yamamoto et al. [41], the hydrodynamic size of the MBs was traced with increasing temperature, where two stages of shrinkage were found. The first stage, up to T_{cp}, was attributed to the collapse of the block with lower T_{cp}, while the second stage (above T_{cp} of the MB solution) was assigned to the collapse of the other block with higher T_{cp}. Thus, it could be concluded that the dehydration of the two constituent blocks was observed subsequently upon heating.

Based on the previous studies, it is indicated that the choice of the side chain architecture provides the opportunity to control the thermoresponsive behavior of MBs. The above-mentioned investigations were carried out using turbidimetry and dynamic light scattering (DLS), which provide T_{cp} and the hydrodynamic size of MB, respectively, while the process of the phase transition is not revealed. It is supposed, that a detailed structural characterization during heating is necessary to disclose the dehydration process of the MBs and to clarify the role of the side chain architecture on their thermoresponsive behavior.

2.4.2 Aggregation in the two-phase state

For aqueous solutions of LCST polymers, above T_{cp}, aggregation of polymers is observed in semi-dilute solutions due to the high hydrophobicity and thus the favored polymer-polymer interaction. Compared to linear polymers, MBs feature enhanced intra- and inter-molecular interactions, namely the interactions between the neighboring side chains and between different MBs, respectively [109]. Thus, the aggregation behavior of thermoresponsive MBs above T_{cp} is yet another aspect to investigate.

For linear LCST polymers, upon heating, the chains gradually interpenetrate and finally form large homogeneous aggregates. For MBs, on the other hand, they form aggregates mainly by agglomerating [110], and they can only interpenetrate at the outermost periphery (if the side chains are long enough to allow such mobility). Thus, the aggregates formed by MBs may be inhomogeneous and possibly have a certain inner structure, which concerns their interaction.

In the work by Li et al. [98], MBs with PNIPAM side chains were investigated in aqueous solutions, and aggregates were formed above T_{cp}. The SANS data collected above T_{cp} show correlation peaks (inset of Figure 2.6c), implying that the aggregates are composed of densely packed MBs. However, as model fitting was not carried out for those data, the inner structure of the aggregates was not quantitatively determined. Further, in the cases of MBs with LCST copolymer side chains, we are not aware of any study addressing the aggregation behavior above T_{cp} and the inner structure of the aggregates.

3. Systems under investigation

In this chapter, the strategy for the present thesis is given, and the MBs that are under investigation in the present thesis are introduced, including the chemical structures and the physical properties revealed in previous studies.

3.1 Strategy for the present study

As discussed in chapter 2.3, the concentration-dependent conformation of MBs in solutions is often investigated using small-angle scattering (SAS), while it remains a challenge to model the scattering contribution from the interaction between MBs. In the present thesis, we try to address the problem by including the structure factor for rigid polymer chains with defined conformational parameters into the SAS fitting model, so that the mutual interaction between MBs corresponds to the structure of individual MBs. The MB under investigation is a chain-like MB, P*i*POx$_{239}$-*g*-P*n*PrOx$_{14}$, introduced in detail in chapter 3.2. Its structure is investigated at a series of concentrations from dilute to semi-dilute condition. Using the above-described fitting model for the SAS data, the concentration-dependent conformation is nicely disclosed, which is then compared with theoretical predictions. The results are presented in chapter 5.

In chapter 2.4, the thermoresponsive behavior of MBs with LCST side chains is discussed in terms of their structural changes. It is known that their structural evolution upon heating strongly depend on their architecture (Figure 2.12), and there has been studies on chain-like MBs as well as ellipsoidal MBs (see ref [97] and ref [98], respectively). In the present thesis, the structural evolution of a cylindrical MB, P*i*POx$_{100}$-*g*-PEtOx$_{17}$ (described in chapter 3.3 in details), featuring a unique length ratio between the backbone and the side chains, is investigated. As temperature varies from below to above T_{cp}, the structural evolution of the MBs and their aggregates in the aqueous solution are revealed in the one-phase and the two-phase states. The results are presented in chapter 6.

As for MBs having LCST copolymer side chains, the monomer sequence in the side chains is proven to affect the thermoresponsive behavior of the MBs, while a detailed structural trace upon variation of temperature has not been reported to the best of our knowledge. To resolve this unclear issue, the LCST behavior of two MBs, P*b*E and P*r*E, which have LCST block- or random- copolymer side chains, respectively (see chapter 3.4 for details), are investigated. The

phase transition process in the one-phase state and the aggregation behavior in the two-phase state are disclosed for their aqueous solutions. The analysis results from the two systems are compared, in order to determine the effects on the thermoresponsive behavior by different arrangements of the monomer sequence in the side chains, which are presented in chapter 7.

3.2 A chain-like MB: P*i*POx$_{239}$-*g*-P*n*PrOx$_{14}$

The MB P*i*POx$_{239}$-*g*-P*n*PrOx$_{14}$ features a poly(2-isopropenyl-2-oxazoline) (P*i*POx) backbone and poly(2-*n*-propyl-2-oxazoline) (P*n*PrOx) side chains, having degrees of polymerization of N_{bk} = 239 and N_{sc} = 14, respectively. On the dangling ends of each side chain, the *tert*-butyloxycarbonyl group, NBocPip, was added for the sake of polymer characterization. The chemical structure of the MB is shown in Figure 3.1. The grafting-from method was used to synthesize the MB. As determined by size exclusion chromatography (SEC), the weight-average molar mass of the backbone, $M_{w,bk}$, is 29.4 kg mol^{-1} with a polydispersity $Đ$ = 1.09. For its overall molecular weight, M_w is 413.1 kg mol^{-1} with $Đ$ = 1.01. The synthesis strategy was a modified method based on ref [111].

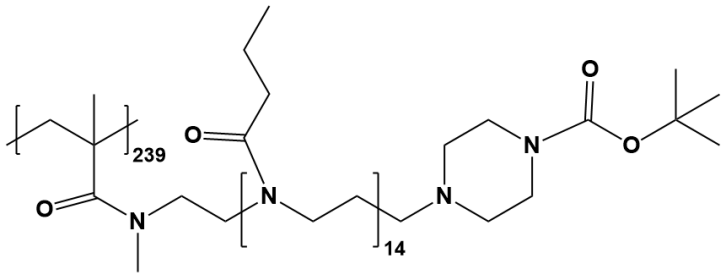

Figure 3.1 Chemical structure of P*i*POx$_{239}$-*g*-P*n*PrOx$_{14}$

Due to the long backbone and the short side chains, P*i*POx$_{239}$-*g*-P*n*PrOx$_{14}$ resembles a large linear polymer, and thus is chosen to be the material for the investigation on the concentration-conformation relation of MB systems. It is dissolved in ethanol into solutions, where ethanol is a good solvent for both the backbone and the side chains.

3.3 A thermoresponsive MB with homopolymer side chains: P*i*POx$_{100}$-*g*-PEtOx$_{17}$

The MB P*i*POx$_{100}$-*g*-PEtOx$_{17}$ features a poly(2-isopropenyl-2-oxazoline) (P*i*POx) backbone and poly(2-ethyl-2-oxazoline) (PEtOx) side chains, which have degrees of polymerization of N_{bk} = 100 and N_{sc} = 17, respectively. The side chains are end-capped with the *tert*-butyloxycarbonyl group, NBocPip, to facilitate the polymer characterization. Its chemical structure is shown in Figure 3.2. The MB was synthesized using the grafting-from method. The P*i*POx$_{100}$ backbone has $M_{w,bk}$ = 12.7 kg mol^{-1} and $Đ$ = 1.14, determined by SEC. For its overall molecular weight, M_w = 150.5 kg mol^{-1} with $Đ$ = 1.14. The synthesis strategy was a modified method based on ref [111].

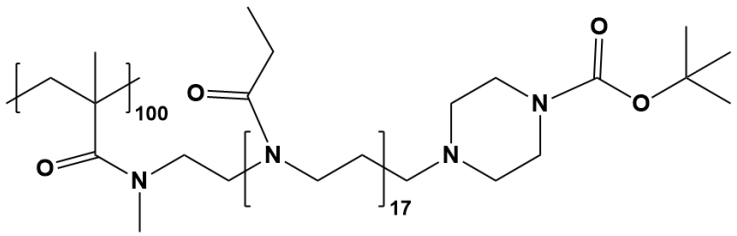

Figure 3.2 Chemical structure of P*i*POx$_{100}$-*g*-PEtOx$_{17}$.

The PEtOx side chains. Poly(2-alkyl-2-oxazoline)s, with the alkyl substituents being methyl-, ethyl- and propyl- groups, exhibit the LCST behavior, which are attractive candidates in biomedical applications due to the biocompatibility as well as the tunable thermoresponsivity [112-120]. With the ethyl substituent, the T_{cp} of poly(2-ethyl-2-oxazoline) (PEtOx) in aqueous solutions was found to range between 61 – 70 °C, depending on the molar mass and the polymer concentration [88, 89], while solutions of PEtOx with N < 100 do not show a phase transition up to 100 °C [90, 121]. Nevertheless, altering the molecular structure from linear chain to grafted/branched structure, several studies have reported that star-like or comb-like polymers with short PEtOx arms (N_{sc} < 100) exhibit LCST behavior in aqueous solutions [94, 122-124].

The thermoresponsive behavior of MBs with PEtOx side chains was investigated in previous studies [94, 124], where T_{cp} of the aqueous solutions were reported to be in the range of 55 – 70 °C. Besides, large aggregates were detected to coexist with the individually dissolved MBs below T_{cp}. In the work by Weber et al. [94], the structural evolution of the MBs (N_{bk} = 95,

N_{sc} = 5) upon varying temperature was revealed using SANS, where the MBs were found to be of cylindrical shape. Heating to temperatures above T_{cp}, they show a shrinkage in the longitudinal direction.

LCST behavior of P*i*POx$_{100}$-*g*-PEtOx$_{17}$. The LCST behavior of the MB, which is composed of a water-soluble P*i*POx backbone [119] and short PEtOx side chains, was firstly characterized by turbidimetry measurements. Figure 3.3a shows the temperature-resolved light transmission of its solution in H_2O at 30 g L^{-1}, recorded for two cycles of heating and cooling scans. The light transmission slightly decreases in the beginning of heating, and sharply drops at around 41 °C, which was reproduced during the second heating scan. T_{cp} of the solution is determined to be 40.5 ± 0.1 °C, as the temperature where the transmission drops to 90 % of the original value. Upon cooling, a hysteresis of about 1 °C is observed, which is also reproducible. The concentration dependence of T_{cp} is demonstrated in Figure 3.3b. It is clearly seen that T_{cp} decreases with increasing concentration, which is a typical behavior of type 1 LCST polymers in aqueous solutions. Such dependence diminishes as the concentration is above 10 g L^{-1}.

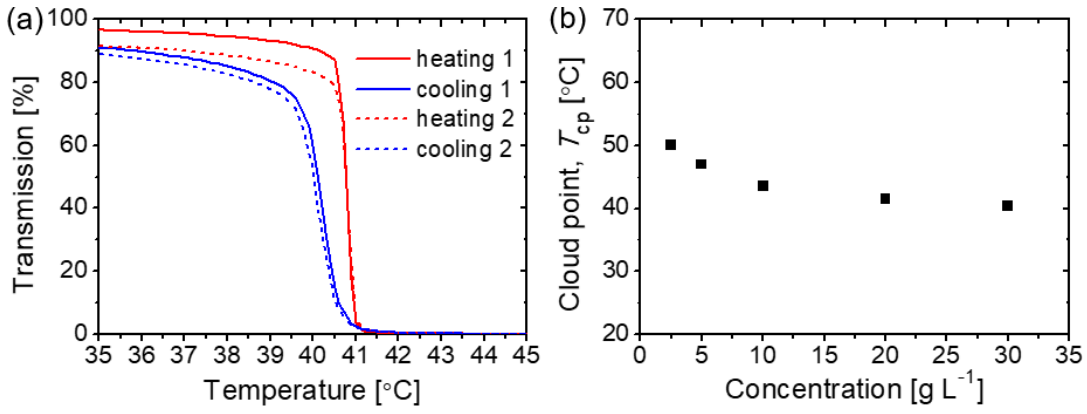

Figure 3.3 (a) Light transmission versus temperature of an P*i*POx$_{100}$-*g*-PEtOx$_{17}$ solution in H_2O at 30 g L^{-1}, measured during two heating and cooling runs, as indicated. (b) Dependence of the resulting T_{cp} of the P*i*POx$_{100}$-*g*-PEtOx$_{17}$ solution in H_2O on the concentration, determined by turbidimetry measurements.

Comparing T_{cp} of P*i*POx$_{100}$-*g*-PEtOx$_{17}$ solution with the one of a linear PEtOx polymer with similar molar mass (T_{cp} > 100 °C), the former shows significantly lower values, which is supposedly due to the close proximity of the side chains [125].

Compared to the T_{cp} values reported by similar systems [94, 124], i.e., polymers with

highly-grafted PEtOx chains (T_{cp} = 55 – 70 °C), the P*i*POx$_{100}$-*g*-PEtOx$_{17}$ solutions have lower T_{cp} values. It is thus concluded that, the hydrophobic NBocPip end groups [126] seem to be also responsible for the reduced T_{cp} of its aqueous solution [98].

3.4 Thermoresponsive MBs with copolymer side chains: P*b*E and P*r*E

Two MBs with thermoresponsive copolymer side chains are under investigation, having different side chain architecture. The backbone is the hydrophobic poly(*para*-hydroxystyrene) (PHOS) [127], and the side chains are composed of poly(propylene oxide) (PPO) and poly(ethylene oxide) (PEO), where both PPO and PEO are LCST-type polymers. While T_{cp} of PPO homopolymers is lower than 8 °C [128], T_{cp} of PEO homopolymers is higher than 100 °C [91, 129]. The two MBs have either PPO-*b*-PEO or P(PO-*ran*-EO) side chains [130, 131]. The total weight fraction of PPO in the MB is 59.2 % for both. In the following content, the MB with PPO-*b*-PEO side chains is given the sample name P*b*E, and the one having P(PO-*ran*-EO) side chains is named P*r*E.

For P*b*E, $M_{w,bk}$ is 10.5 kg mol^{-1} with $Đ$ = 1.18, determined by SEC. It gives a backbone degree of polymerization N_{bk} = 88. The overall weight-average molar mass M_w is 1135 kg mol^{-1}, determined by static light scattering (SLS). Calculated from M_w and $M_{w,bk}$, weight-average molar mass of the PPO-*b*-PEO side chains is $M_{w,sc}$ = 13.0 kg mol^{-1}, giving a side chain degree of polymerization N_{sc} = 253. The PPO blocks are attached to the PHOS backbone, leaving the PEO blocks dangling at the periphery of the MB. The chemical structure of P*b*E is shown in Figure 3.4a.

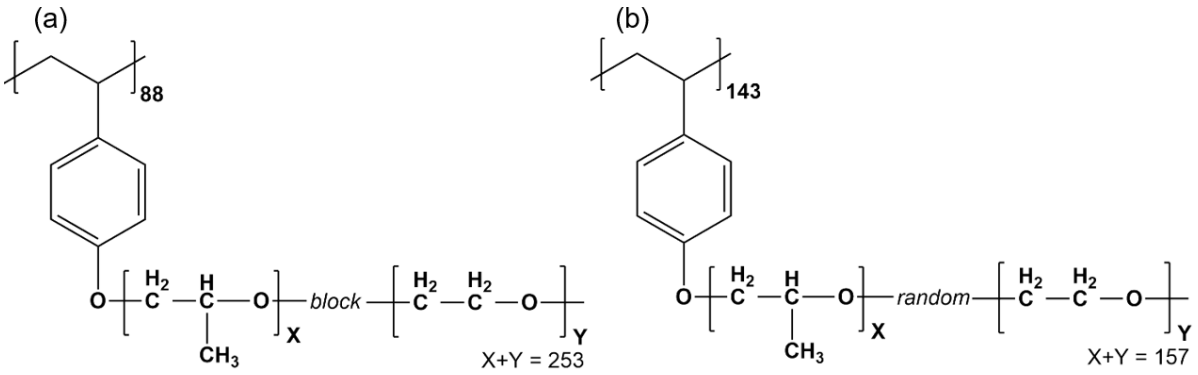

Figure 3.4 Chemical structures of the MBs under investigation. (a) MB with PPO-*b*-PEO side chains, P*b*E (b) MB with P(PO-*ran*-EO) side chains, P*r*E.

For P*r*E, the backbone features $M_{w,bk}$ = 17 kg mol^{-1} and $Đ$ = 1.22, from SEC, giving N_{bk} = 143. The overall M_w = 1166 kg mol^{-1} was determined by SLS. From M_w and $M_{w,bk}$, $M_{w,sc}$ = 8.2 kg mol^{-1} and N_{sc} = 157 for the P(PO-*ran*-EO) side chains are calculated. The chemical structure of P*r*E is shown in Figure 3.4b.

Both MBs were synthesized using the grafting-from method. The detailed description about the synthesis process and strategies is given in ref [130] for P*b*E, and in ref [131] for P*r*E.

Micelles formed by PPO-*b*-PEO vs. MBs with PPO-*b*-PEO/P(PO-*ran*-EO) side chains. As PPO is essentially hydrophobic while PEO is hydrophilic at ambient temperature, copolymers of PPO and PEO form micelles in aqueous solutions at concentrations above the critical micelle concentration of the system, featuring a core-shell structure with PPO protected in the inner part by the water-swollen PEO in the outer part [132]. Since such a structure features a hydrophobic nanodomain for drug storage, in combination with the good biocompatibility and the tunable LCST behavior of PPO-*b*-PEO, the system is considered suitable for drug delivery applications [133-135].

With a similar structure, the MB with PPO-*b*-PEO side chains, where the PPO block is attached to the backbone, is also considered as potential candidates as drug carriers. Moreover, the MB with P(PO-*ran*-EO) side chains may serve the same purpose, as the high polymer density in the core part makes it a space with low water content. In this case, the hydrophobicity of the core domain can supposedly be controlled by the composition of PO and EO on the side chains. It provides an opportunity to optimize the MB in terms of the drug loading capacity as well as the stability of the system, which was already realized in an amphiphilic block copolymer system [136, 137].

LCST behavior of P*b*E and P*r*E. In previous research, the LCST behavior of P*b*E and P*r*E was investigated in dilute aqueous solutions at 1 g L^{-1} [130, 131]. (Their crystallization behavior in the melt was also addressed, see ref [138].) The apparent weight-average molar mass $M_{w,app}$, the scattering intensity (I) and the hydrodynamic radius (R_h) were traced upon increasing temperature by SLS and DLS, where these parameters increase at high temperatures due to the formation of aggregates in the solution (Figure 3.5 for P*b*E, Figure 3.6 for P*r*E). The temperature where the aggregates appear was considered to be T_{cp} of the solution, which is 50 °C for P*b*E and 37.5 °C for P*r*E. (Note that the increase in $M_{w,app}$ and R_h is not obvious in the case of P*b*E (Figure 3.5), which hints that T_{cp} of the P*b*E solution could possibly be higher than 50 °C.) Thus, even though having the same PPO/PEO composition in the MB, P*b*E and P*r*E exhibit different LCST behavior as a result of the different monomer sequences in the copolymer side chains.

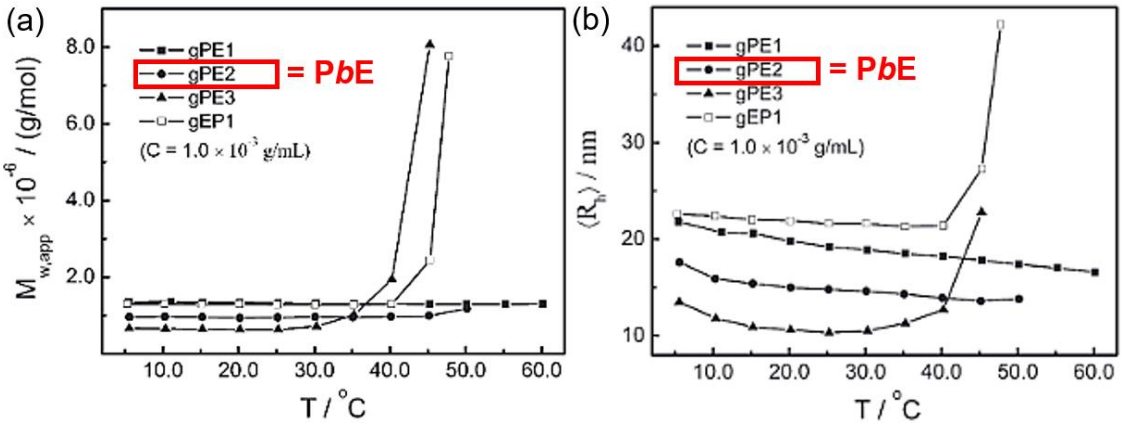

Figure 3.5 Temperature dependence of the (a) apparent weight-average molar mass $M_{w,app}$ and (b) hydrodynamic radius (R_h) of a P*b*E solution at 1 g L^{-1} in H_2O, indicated by the sample name of "gPE2" in the graphs. Reprinted with permission from ref [130]. Copyright (2010) American Chemical Society. The red squares and the indication in red words are added by the author of the present thesis.

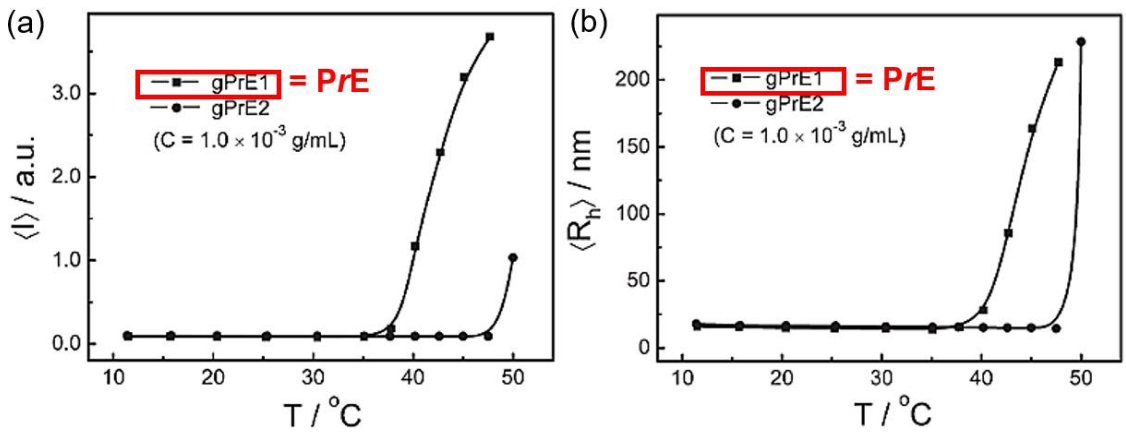

Figure 3.6 Temperature dependence of the (a) average scattering intensity ⟨*I*⟩ and (b) hydrodynamic radius $\langle R_h \rangle$ of a P*r*E solution at 1 g L^{-1} in H_2O, indicated by by the sample name of "gPrE1" in the graphs. Reprinted with permission from ref [131]. Copyright (2010) John Wiley and Sons. The red squares and the indication in red words are added by the author of the present thesis.

4. Experimental techniques

In the present thesis, the methods used for the structural investigation on the MBs include dynamic light scattering (DLS), small-angle X-ray/neutron scattering (SAXS/SANS) and *cryo*-electron microscopy (*cryo*-EM). The principles as well as the experimental setups of these techniques are introduced in this chapter.

4.1 Dynamic light scattering (DLS)

This section is written based on ref [139].

DLS is a technique for the determination of the hydrodynamic size of nanoparticles in solutions, making use of the temporal fluctuations of the scattering intensity of the sample solution. In a DLS setup (Figure 4.1a), a monochromatic coherent light source is aligned to illuminate on the sample, which is usually solutions containing colloidal particles, and the intensity of the scattered light is recorded by a detector positioned at a scattering angle 2θ. The detector is connected to a correlator. Indicated in the top view of the DLS setup (Figure 4.1b), the scattering vector $\boldsymbol{q}$ is defined as the difference of the incident wave vector $\boldsymbol{k}_\mathbf{i}$ and the scattered wave vector $\boldsymbol{k}_\mathbf{s}$ to be:

$$\boldsymbol{q} = \boldsymbol{k}_\mathbf{s} - \boldsymbol{k}_\mathbf{i} \tag{4.1}$$

Assuming elastic scattering, the magnitude of both $\boldsymbol{k}_\mathbf{i}$ and $\boldsymbol{k}_\mathbf{s}$ is $2\pi n/\lambda$, where n is the refractive index of the solvent, and λ is the wavelength of the incident light in vacuum. The magnitude of $\boldsymbol{q}$, which is essentially the momentum transfer, is thus given as:

$$|\boldsymbol{q}| = q = \frac{4\pi n \sin(\theta)}{\lambda} \tag{4.2}$$

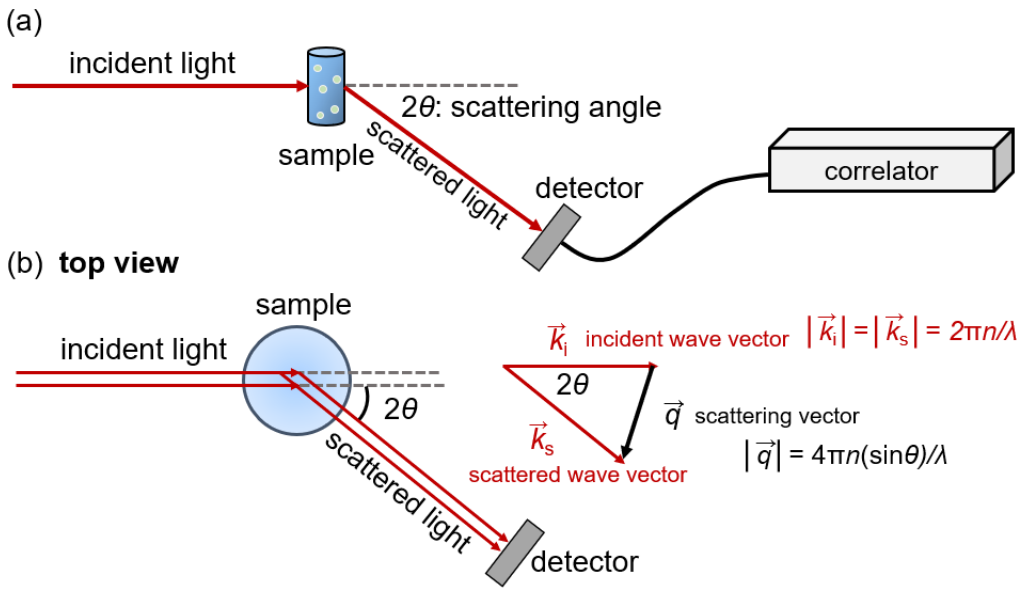

Figure 4.1 Schematic drawing of a DLS setup. (a) An overview, showing the light source scattered by the scattering objects (spheres in the sample), and the signal recorded by a detector at a scattering angle 2θ. (b) A top view, indicating the relation between the incident wave vector $\boldsymbol{k}_i$, the scattered wave vector $\boldsymbol{k}_s$ and the scattering vector $\boldsymbol{q}$.

With the correlator, the time dependence of the scattering intensity $I(t,q)$ is transformed to the normalized intensity autocorrelation function, $g_2(\tau,q)$, by:

$$g_2(\tau, q) = \frac{\langle I(t,q)I(t+\tau,q)\rangle_t}{\langle I(t,q)\rangle_t^2} \tag{4.3}$$

$g_2(\tau,q)$ expresses the correlation between $I(t,q)$ and $I(t+\tau,q)$, where τ is the delay time and the brackets denote the time-average. It reveals the diffusional information of the Brownian motion of the scattering objects, which is related to their hydrodynamic size. For example, small objects diffuse faster than large ones, thus the correlation between $I(t,q)$ and $I(t+\tau,q)$ decays at smaller τ-values (at the same temperature and in the same solvent), characterized by the relaxation time τ_D.

By the Siegert relation, $g_2(\tau,q)$ is linked to the normalized field autocorrelation function, $g_1(\tau,q)$, by:

$$g_2(\tau, q) - 1 = \beta^{coh}[g_1(\tau, q)]^2 \tag{4.4}$$

where β^{coh} is the coherence factor of the scattered light and is dependent on the instrument. Typically, $\beta^{coh} \leq 1$ applies, with $\beta^{coh} = 1$ for the spatially coherent scattered light [140].

When the scattering objects in the sample solution are monodisperse particles, $g_1(\tau,q)$ shows a single exponential decay:

$$g_1(\tau, q) = \exp(-\tau/\tau_D) = \exp(-\Gamma\tau) \tag{4.5}$$

The decay rate Γ, defined as τ_D^{-1}, gives the translational diffusional coefficient D of the particles by:

$$\Gamma = Dq^2 \tag{4.6}$$

Thus, D is independent of q, and it can be obtained by Γ/q^2, when the DLS data are collected at only one q value. When DLS data are collected at multiple q values, D can be obtained by the slope of the Γ vs. q^2 plot, setting the y-intercept to zero. From D, the hydrodynamic radius R_h of the particle is calculated using the Stokes-Einstein equation:

$$R_h = \frac{k_B T}{6\pi\eta_s D} \tag{4.7}$$

where k_B is Boltzmann's constant, T is the solution temperature and η_s is the viscosity of the solvent. Particles like hard spheres are the ideal case for the above-described monodisperse system. They have an isotropic shape, and a compact inner structure. In this case, the detected motion is the translational diffusion of the scattering objects.

When the scattering objects feature a size distribution, $g_1(\tau,q)$ can be expressed as [141]:

$$g_1(\tau, q) = \exp(-\Gamma\tau) \times (1 + \frac{\mu_2}{2}\tau^2 - \frac{\mu_3}{6}\tau^3) \tag{4.8}$$

Such expression is referred to as the modified cumulant method to the third-order, where Γ represents the mean decay rate. μ_2 and μ_3 are the second and third moments, respectively, providing hints to the standard deviation of Γ in the system.

When there are more than one kind of scattering objects with distinctly different sizes in the system, $g_1(\tau,q)$ can be assumed as an integral of τ_D:

$$g_1(\tau, q) = \int G(\tau_D) \exp(-\tau/\tau_D) d\tau_D \text{ with } \int G(\tau_D)\, d\tau_D = 1 \tag{4.9}$$

Here, the multiplicity of the particle size is expressed by a relaxation time distribution $G(\tau_D)$, which is referred to as the regularized positive exponential sum (REPES) method. It yields the t_D distribution and thus D, from which the R_h distribution is further obtained. Using the Gendist analysis software, the R_h distribution is expressed in the equal-area representation $R_h A(R_h)$ vs.

log(R_h). Typically, the R_h distribution features one or more peaks, and the center of mass of the peak is taken as the R_h value from the corresponding measurement.

Scattering objects with complex inner structure. When the scattering objects are polymer chains, branched polymers or cross-linked polymers, where the segmental chains show certain degrees of mobility, the DLS data reveal not only the translational motion of the total center of mass, but also the internal modes of motion from the mobile segments [142, 143]. In such systems, the Γ vs. q^2 plot is no longer linear as expressed in equation 4.6. Rather, Γ/q^2 is q - dependent:

$$\Gamma = D(1 + C_h R_g^2 q^2) q^2 \tag{4.10}$$

R_g is the radius of gyration of the scattering object, and C_h is a structure coefficient. Comparing equation 4.10 with equation 4.6, the additional term of $C_h R_g^2 q^2$ accounts for the contribution from the internal motions. The Γ vs. q^2 plot deviates from the linear relation, especially at high q. Thus, for samples featuring motions of segmental chains, D should be extracted from low q, where the translational motion of the center of mass is reflected. Depending on the geometry of the scattering objects, different values of C_h are found. The simplest case is a hard sphere, which has a C_h value of zero [144]. C_h is 0.03 for thin rods [145], 0.2 for random coils [146], whereas C_h is found to be 0.1 – 0.2 for branched polymers [147, 148]. The geometry-dependent C_h values are schematically shown in Figure 4.2.

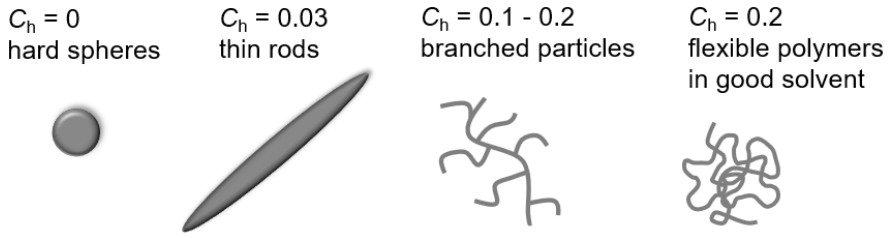

Figure 4.2 Schematic representation of the particles featuring different geometries with the corresponding structure coefficient C_h.

As MBs are highly-branched, and supposedly have an isotropic overall shape, it is of interest to determine the effect of the architecture on the Γ vs. q^2 plots, and whether the internal modes of motion can be detected in the DLS data of their solutions. It is also important to note that the internal modes of motion are expected to be strongest for chain-like MBs, but not for

spherical or ellipsoidal MBs, as the former resemble polymer chains while the latter resemble hard spheres.

Concentration effect on diffusion coefficient. The diffusion coefficient D measured by DLS is dependent on the solution concentration c, which can be approximated by the virial expression:

$$D(c) = D_0[1 + k_D c] \tag{4.11}$$

where D_0 is the diffusion coefficient as c approaches zero. The virial coefficient k_D gives indication on a repulsion ($k_D > 0$) or an attractive ($k_D < 0$) interaction between the diffusing objects. From D_0, the hydrodynamic radius of infinite dilution, $R_{h,0}$, can be calculated using the Stokes–Einstein equation (equation 4.7).

Instrument. All the DLS measurements in the present thesis were performed using a LS Spectrometer (LS Instruments, Fribourg, Switzerland). It is equipped with a goniometer, two avalanche photodiode detectors and a polarized HeNe laser (λ = 632.8 nm) (Thorlabs, Dachau, Germany) with a maximum power of 21 mW. The sample was loaded in cylindrical glass cuvettes with 5 mm outer diameter and 0.4 mm wall thickness. The cuvettes were then mounted in a decalin bath, whose temperature was controlled by a Julabo CF31 *Cryo*-Compact Circulator (JULABO, Seelbach, Germany). From a two channel multi tau correlator, the recorded scattering intensity $I(t,q)$ was converted to the autocorrelation functions $g_2(\tau,q)$.

Measurement and data analysis. For a typical measurement, the scattering intensity of the sample solution is traced with time at a controlled temperature with a duration of 30 s, at one or a wide range of q. Subsequently, the correlator transforms the signal into $g_2(\tau,q)$, which is then analyzed by the modified cumulant method or by the REPES method. The analysis results give D of the scattering objects in the sample solution, from which R_h can be calculated. In the present thesis, the DLS results are obtained by repeating the measurement for 20 times, giving an average R_h value and an uncertainty from the standard deviation of R_h.

4.2 Small-angle X-ray/neutron scattering (SAXS/SANS)

This section is written based on ref [149], ref [150] and ref [151].

Small-angle scattering (SAS) of X-rays and neutrons are fundamental tools for the structural investigation of macromolecules having dimensions from few nanometers to several hundred nanometers, as the wavelength is in the same order of magnitude as the characteristic length scales between atoms composing the molecules. In a typical SAS setup (Figure 4.3), a well-aligned X-ray/neutron beam with a finite wavelength distribution illuminates on the sample, and the scattering intensity is collected by a 2D detector. Generally, the refractive index n is slightly less than (and very close to) 1. In this context, applying $n = 1$ in equation 4.2, as sufficient for the present purpose, gives the momentum transfer q as:

$$|\boldsymbol{q}| = q = \frac{4\pi\sin(\theta)}{\lambda} \tag{4.12}$$

As demonstrated in Figure 4.3, the available q-range depends not only on the beam wavelength λ, but also on the sample-to-detector distance (SDD) and the geometry of the detector. From sample to detector, the system is located in an evacuation tube, to reduce the scattering and absorption by air.

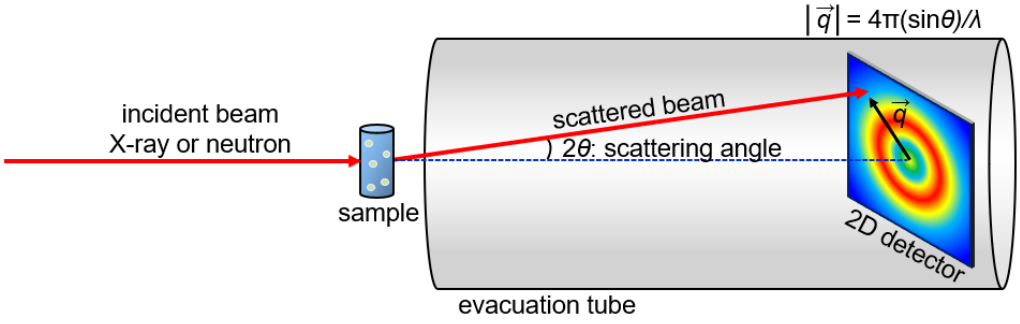

Figure 4.3 Representation of a small-angle scattering setup, where the incident beam is either an X-ray or a neutron beam. The scattered beam from the sample is recorded in a range of scattering vectors $\boldsymbol{q}$ by a 2D detector.

The beam is incident on the sample and interacts with the electrons (X- rays) or nuclei (neutrons). The scattering efficiency of elements is characterized by the scattering length b. As X-rays interact with electrons of the atoms, the X-ray scattering length b_x is positively related to the atomic number; whereas this is not the case for neutron scattering length b_n, which

concerns the nuclear structure and depends on the nucleus under question. Table 4.1 lists b_x and b_n values of the elements typically present in organic compounds.

Table 4.1 X-ray and neutron scattering lengths of selected atoms [152].

Atom	**H**	**D**	**C**	**N**	**O**	**P**	**S**
Atomic mass [g mol^{-1}]	1	2	12	14	16	30	32
Number of electrons	1	1	6	7	8	15	16
b_x[(a)] [10^{-12} cm]	0.282	0.282	1.69	1.97	2.16	3.23	4.51
b_n[(b)] [10^{-12} cm]	-0.374	0.667	0.665	0.940	0.580	0.510	0.280

[(a)]X-ray scattering length. [(b)]Neutron scattering length.

The scattering length density (SLD), ρ, is introduced as the total scattering length per unit volume. When the light source illuminates on the sample, the scattering amplitude from an illuminated volume V is expressed with ρ as:

$$A(\boldsymbol{q}) = \int_V \rho(\boldsymbol{r}) \exp(-i\boldsymbol{q}\boldsymbol{r})\, \mathrm{d}\boldsymbol{r} \tag{4.13}$$

where $\rho(\boldsymbol{r})$ is the SLD distribution as a function of the position vector $\boldsymbol{r}$ of the electrons/nuclei. equation 4.13 illustrates that the scattering intensity in the reciprocal space is related to the SLD distribution in the real space by a Fourier transformation.

Usually, the scattering particles under investigation are embedded in a homogeneous matrix, e.g., the solvent. Thus, $\rho(\boldsymbol{r})$ can be written as $\rho(\boldsymbol{r}) = \Delta\rho(\boldsymbol{r}) + \rho_0$, where ρ_0 is the SLD of the matrix and $\Delta\rho(\boldsymbol{r})$ the excess SLD that leads to a scattering contrast. A schematic representation of $\rho(\boldsymbol{r})$ in one dimension is shown in Figure 4.4, where $\Delta\rho$ represents the average excess SLD over the particle volume. As SAS arises from such scattering contrast in the system, the scattering amplitude from one particle in a homogeneous matrix can be rewritten from equation 4.13 as:

$$A(\boldsymbol{q}) = \int_{V_p} \Delta\rho(\boldsymbol{r}) \exp(-i\boldsymbol{q}\boldsymbol{r})\, \mathrm{d}\boldsymbol{r} \tag{4.14}$$

with an integral over the particle volume V_p.

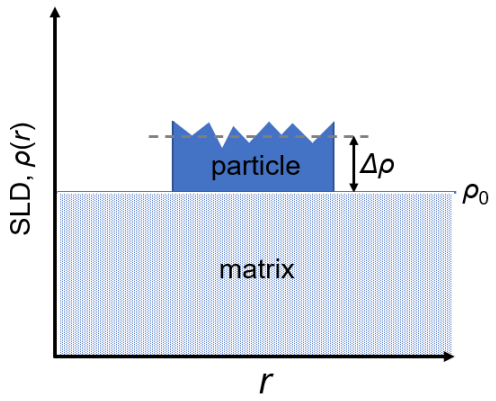

Figure 4.4 Representation of SLD distribution in one dimension, $\rho(r)$, of a particle embedded in a matrix. ρ_0 is the SLD of the matrix, and $\Delta\rho$ is the average excess SLD

From the square of the absolute amplitude value, the scattering intensity of an individual particle in one dimension, $I_p(q)$, is:

$$I_p(q) = |A(\boldsymbol{q})|^2 = {V_p}^2 \Delta\rho^2 P(q) \tag{4.15}$$

where $P(q)$ is the normalized scattering form factor, characterizing the size, shape and inner structure of the particle. Note that, V_p times the excess SLD, $\Delta\rho$, is the total scattering length of the particle. With the expression in equation 4.15, SAS data can be commonly expressed in the form of:

$$I(q) = N_p {V_p}^2 \Delta\rho^2 P(q) S(q) \tag{4.16}$$

where N_p is the total number of particles in the illuminated volume. $S(q)$ is the structure factor, accounting for the spatial correlation between the particles. For dilute systems where particles are uncorrelated, $S(q) = 1$; whereas for semi-dilute or concentrated systems, $S(q) \neq 1$.

For solution samples, the scattering particles are randomly oriented, therefore the collected 2D scattering intensity is isotropic (like the 2D intensity pattern shown on the detector in Figure 4.3). After azimuthally averaged, the one-dimensional scattering intensity is plotted as a function of q.

Concerning the instrumental aspects, the finite beam size, wavelength spread and detector resolution lead to a smearing of $I(q)$ [153, 154]. The smearing effects can be accounted for by applying a standard deviation of the momentum transfer, Δq. For SAXS, the beam is highly monochromatic and Δq is usually small, especially under pinhole collimation, thus the smearing effects can be neglected. For SANS, on the other hand, the wavelength spread is significantly large ($\Delta\lambda/\lambda$ between 10 % and 30 % by velocity selectors, and $\Delta\lambda/\lambda$ between 0.1 % and 5 % by crystal monochromations) [155, 156], which should be taken into account during the data

analysis.

Choice of the form factor for MBs. As discussed in chapter 2.2, the overall shape of MBs depends on their architectural parameters. With high grafting densities, the shape could be spherical, ellipsoidal, cylindrical or chain-like, relying on the length ratio between the backbone and the side chains. Thus, the scattering form factor is chosen according to the architectural parameters to be the one of a sphere, an ellipsoid, a cylinder or a flexible cylinder, as depicted in Figure 4.5. Besides the overall appearance, the inner structure should be considered as well. As the grafting structure results in a SLD gradient at the interface between the MB and the solvent, a fuzziness of the particle surface may be assumed. Or, in case of spherical/ellipsoidal MBs, where the side chain length is comparable to the backbone length, a core-shell structure is assumed to account for the significant density difference between the inner and the outer part of the MB.

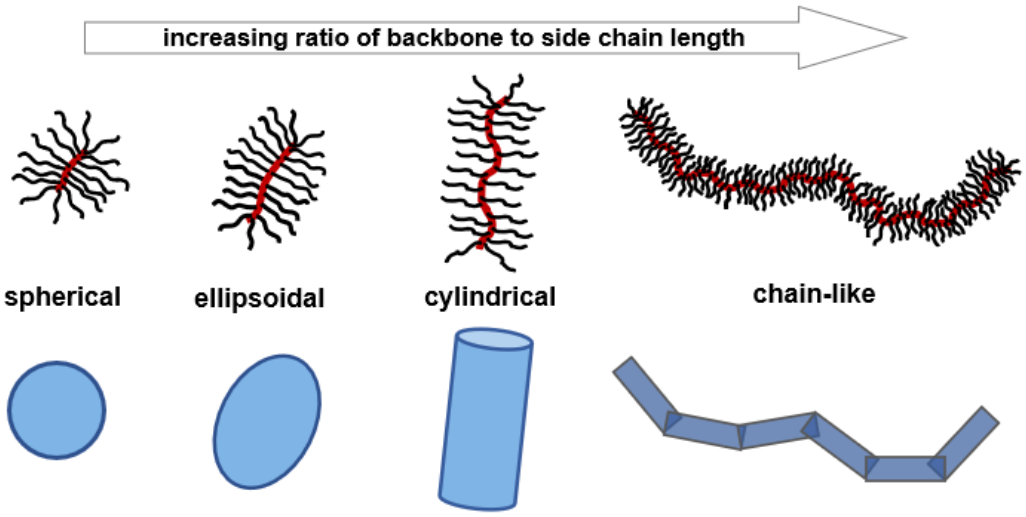

Figure 4.5 Schematic representation of the overall shape of MBs with increasing length ratio of backbone to side chain (upper row), and the corresponding choice of the scattering form factor (bottom row).

The mathematical expression of the form factors used in the present thesis are listed below:

(i) Fuzzy sphere form factor $P_{fz}(q)$ [157]:

$$P_{fz}(q) = I_0 \left\{ \frac{3[\sin(qR_{fz}) - qR_{fz}\cos(qR_{fz})]}{(qR_{fz})^3} \exp\left(-\frac{(fq)^2}{2}\right) \right\}^2 \qquad (4.17)$$

I_0 is a scaling factor. R_{fz} is the fuzzy sphere radius, and f is the fuzziness. The SLD profile along

the radial direction of a fuzzy sphere is shown in Figure 4.6, where the SLD is homogeneous in the central region and starts to decrease at R_{fz} - 2f until it reaches zero at R_{fz} + 2f.

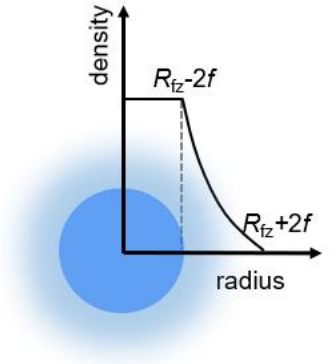

Figure 4.6 SLD profile of the fuzzy sphere form factor $P_{fz}(q)$, in the radial direction. The blue sphere has a constant SLD in the core region, and the bluish corona indicates a gradual decrease of SLD at the sphere surface, which is characterized by the fuzzy sphere radius R_{fz} and the fuzziness f.

Example curves of $P_{fz}(q)$ are given in Figure 4.7. At fixed f, the sharp fringes in the SAS data shift towards low q with increasing R_{fz} (Figure 4.7a). At fixed R_{fz}, the fringes smear with increasing f (Figure 4.7b).

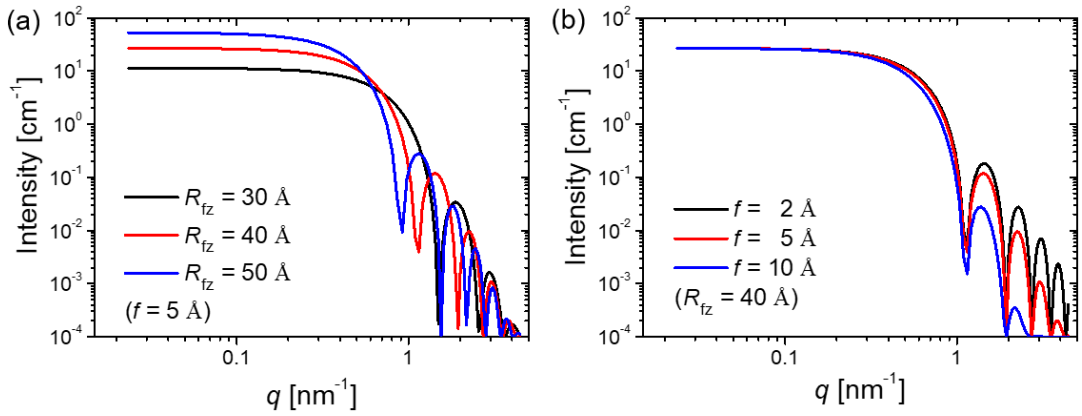

Figure 4.7 Example curves of the fuzzy sphere form factor $P_{fz}(q)$. (a) Curves with selected values of R_{fz} at fixed f. (b) Curves with selected values of f at fixed R_{fz}.

(ii) Core-shell ellipsoid form factor $P_{cs}(q)$ [158, 159]:

$$P_{cs}(q) = I_0 \int_0^{\frac{\pi}{2}} \left[\mathrm{f}\left(q, R_p, R_e, a\right) + \mathrm{f}\left(q, R_p{+}T_p, R_e{+}T_e, a\right)\right]^2 \sin(a)\,\mathrm{d}a \qquad (4.18)$$

and

$$\mathrm{f}(q, R_p, R_e, a) = \frac{3\Delta\rho V_p\{\sin[qr(R_p, R_e, a)] - \cos[qr(R_p, R_e, a)]\}}{[qr(R_p, R_e, a)]^3} \qquad (4.19)$$

$$\text{with } r(R_p, R_e, a) = \left\{[R_e \sin(a)]^2 + [R_p \cos(a)]^2\right\}^{0.5}$$

I_0 is a scaling factor. R_p and R_e are the radii in the core part along the polar and the equatorial axes, respectively. T_p and T_e are the shell thicknesses along the polar and the equatorial axes, respectively. a is the angle between the polar axis and q. $\Delta\rho$ is the scattering contrast. In f(q, R_p, R_e, a), $\Delta\rho$ is the SLD difference between the core and the shell, i.e., (ρ_c - ρ_s); while in f(q, R_p+T_p, R_e+T_e, a), it is the SLD difference between the shell and the solvent, i.e., (ρ_s - ρ_0).

Example curves of $P_{cs}(q)$ are given in Figure 4.8. Changing the core radii and the shell thicknesses, the curves shift towards low q or high q when the particle size increases or decreases, respectively (Figure 4.8a,b). At fixed core radii and shell thicknesses, large $\Delta\rho$ between the shell and the solvent leads to higher absolute scattering intensity (Figure 4.8c).

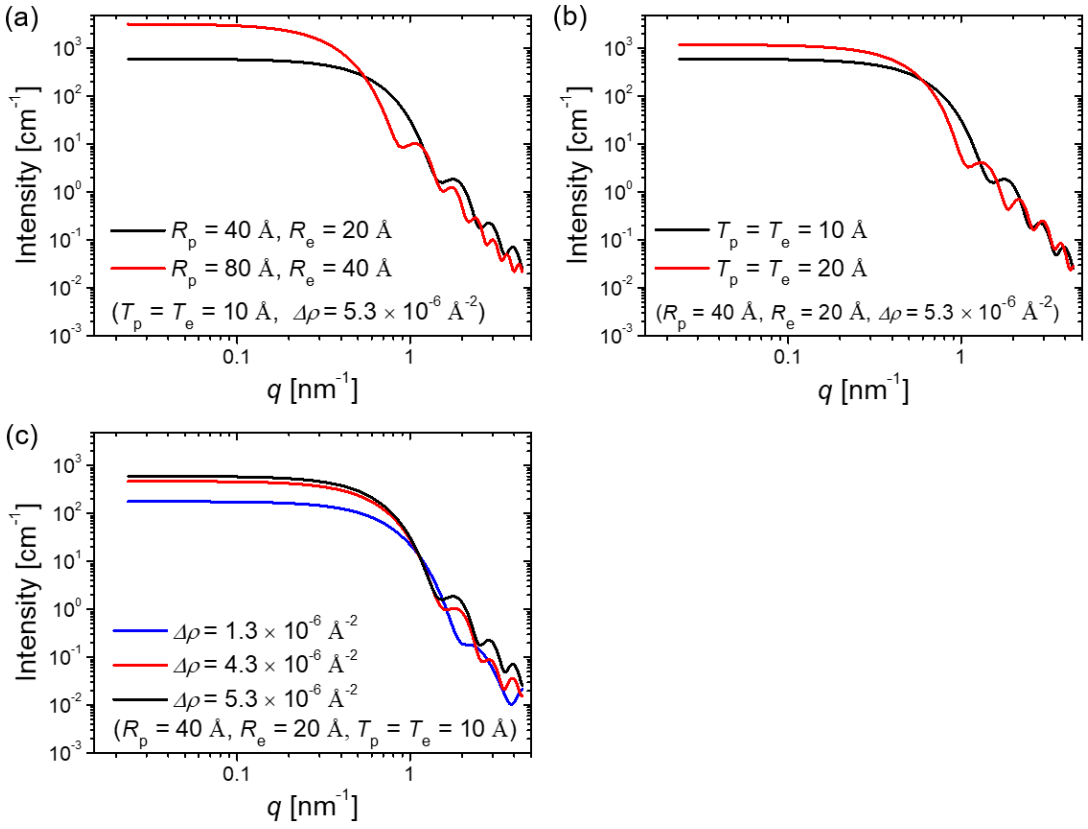

Figure 4.8 Example curves of the core-shell ellipsoid form factor $P_{cs}(q)$. (a) Curves with selected values of R_p and R_e, at fixed shell thicknesses and $\Delta\rho$ between the shell and the solvent. (b) Curves with selected values of T_p and T_e, at fixed core radii and $\Delta\rho$. (c) Curves with selected values of $\Delta\rho$ at fixed core radii and shell thicknesses.

(iii) Cylinder form factor $P_{cyl}(q)$ [160-162]:

$$P_{cyl}(q) = I_0 \int_0^{\pi/2} \left\{ \frac{2J_1[qR\sin(a)]}{qR\sin(a)} \frac{sin\left[\frac{1}{2}qL\cos(a)\right]}{\frac{1}{2}qL\cos a} \right\}^2 \sin(a)\,da \qquad (4.20)$$

I_0 is a scaling factor. J_1 is the Bessel function of the first kind, and a is the angle between the longitudinal axis of the cylinder and q. R and L are the cross-sectional radius and the length of the cylinder, respectively.

Example curves of $P_{cyl}(q)$ are given in Figure 4.9, which all feature $I(q) \sim q^{-1}$ between the range of $1/L < q < 1/R$. At fixed R, a variation of L is reflected at low q of the curve (Figure 4.9a), since L determines the largest length of the scattering particle. With a larger L value, the curve starts obeying $I(q) \sim q^{-1}$ at a lower q. At fixed L, the curve shifts towards low q with increasing R (Figure 4.9b).

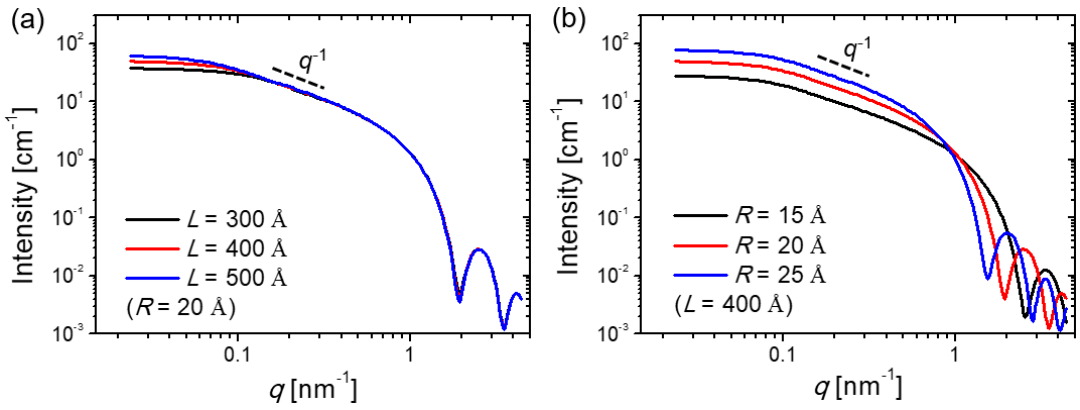

Figure 4.9 Example curves of the cylinder form factor $P_{cyl}(q)$. (a) Curves with selected L at fixed R. (a) Curves with selected R at fixed L. The dashed line corresponds to $I(q) \sim q^{-1}$.

(iv) Flexible cylinder form factor $P_{fc}(q)$: This form factor was developed by Monte Carlo simulation to describe the scattering of a worm-like chain with a finite cross section [163-165]:

$$P_{fc}(q) = P_{wlc}(q)S_{xs}(qR_c) \qquad (4.21)$$

$P_{wlc}(q)$ is the scattering of a single worm-like chain, featuring the contour length L_c and the persistence length l_p, as schematically shown in Figure 4.10. The detailed expression of $P_{wlc}(q)$ is given in Method 3 of ref [163]. $S_{xs}(qR_c)$ accounts for the cross section of the segmental cylinder, providing the cross-sectional radius R_c. It reads:

$$S_{xs}(qR_c) = \left[\frac{2J_1(qR_c)}{qR_c}\right]^2 \tag{4.22}$$

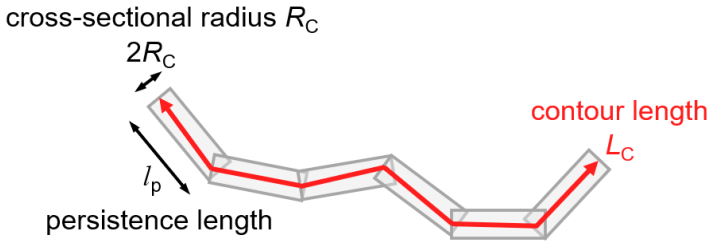

Figure 4.10 Schematic representation of the flexible cylinder form factor $P_{fc}(q)$, composed of continuously connected rigid cylinders (greyish rectangles) with a length l_p and a cross-sectional radius R_c, resulting in a total length of L_c (red line).

Example curves of $P_{fc}(q)$ are given in Figure 4.11. The curves all feature $I(q) \sim q^{-5/3}$ between the range of $1/L_c < q < 1/R_c$, i.e., around $1/l_p$, except for the case when these values are very close (see the red curve with l_p = 25 Å and R_c = 20 Å in Figure 4.11b). Different from the cylinder length L from $P_{cyl}(q)$ mentioned above, L_c from $P_{fc}(q)$ concerns a wider length scale in the particle, thus, a variation of L_c is reflected from low to intermediate q range (Figure 4.11a). With increasing l_p, the q-range featuring $I(q) \sim q^{-5/3}$ shifts towards low q (Figure 4.11b). With increasing R_c, the curves shift towards low q (Figure 4.11c).

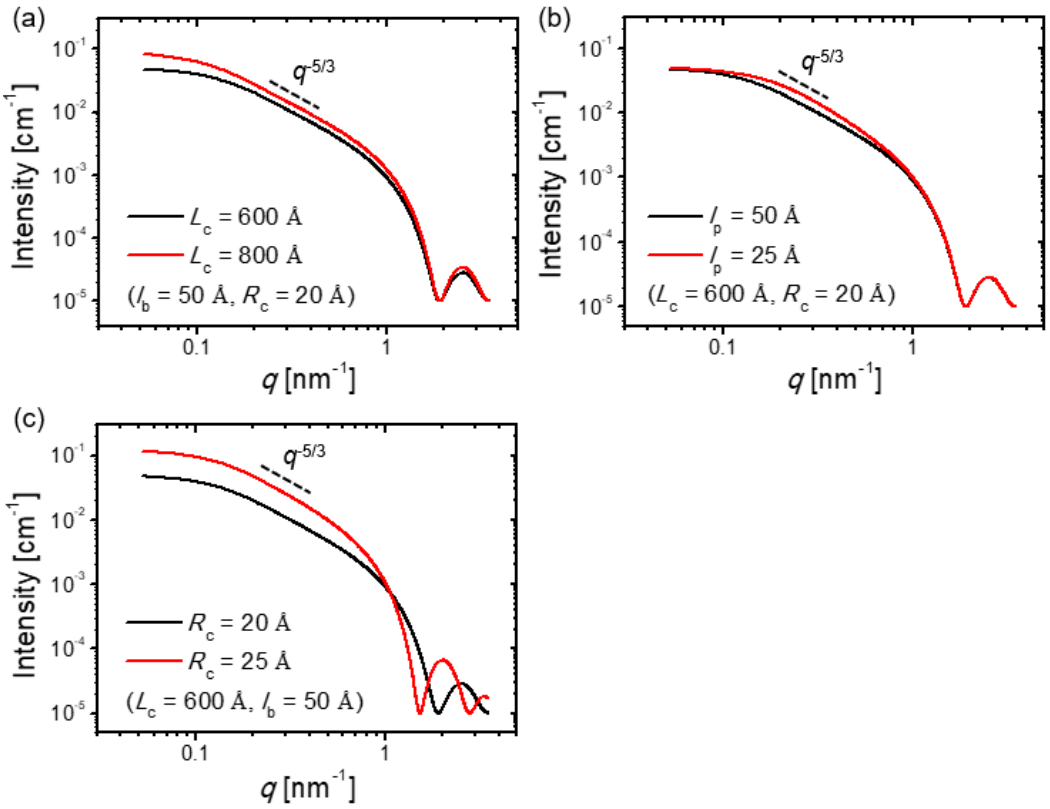

Figure 4.11 Example curves of the flexible cylinder form factor $P_{fc}(q)$. (a) Curves with selected values of L_c at fixed l_p and R_c. (b) Curves with selected values of l_p at fixed L_c and R_c. (c) Curves with selected values of R_c at fixed L_c and l_p. The dashed line corresponds to $I(q) \sim q^{-5/3}$.

Choice of the structure factor for MBs. For semi-dilute or concentrated systems, a structure factor is often needed to describe the correlation between the MBs, and the suitable choice of the structure factor is related to the shape of the MBs. For MBs featuring an overall spherical, ellipsoidal or cylindrical shape, the Percus-Yevick hard-sphere structure factor, $S_{HS}(q)$, is the simplest way to describe their spatial correlation, which assumes the potential energy, $U(r_{int})$, between neighboring MBs as a function of the distance r_{int} between their center of masses to be [166]:

$$U(r_{int}) = \begin{cases} \infty & \text{for } r_{int} < 2R_{HS} \\ 0 & \text{for } r_{int} \geq 2R_{HS} \end{cases} \tag{4.23}$$

where R_{HS} is the hard-sphere radius. Since the relation between MBs is modeled as the one between hard spheres, the value of $2R_{HS}$ provides an estimate of the average distance between the correlated MBs in the system. This is schematically represented in Figure 4.12.

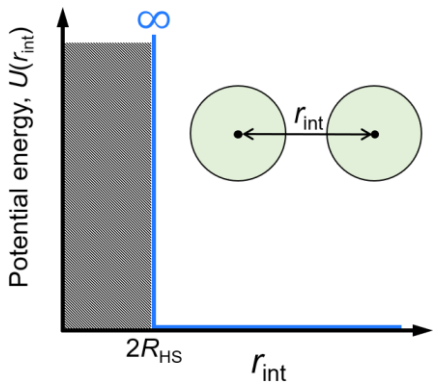

Figure 4.12 The potential energy (blue line), $U(r_{int})$, as a function of the inter-particle distance r_{int} in the Percus-Yevick hard-sphere structure factor $S_{HS}(q)$. The cartoon demonstrates two hard spheres separated by a distance r_{int}.

It has the mathematical expression of:

$$S_{HS}(q) = \frac{1}{1 + 24\eta G(x)/x} \text{ with } x = 2qR_{HS} \tag{4.24}$$

and

$$\begin{aligned} &G(x) \\ &= \gamma \frac{\sin(x) - x\cos(x)}{x^2} + \delta \frac{2x\sin(x) + (2 - x^2)\cos(x) - 2}{x^3} \\ &+ \varepsilon \frac{-x^4\cos(x) + 4[3x^2 - 6\cos(x) + (x^3 - 6x)\sin(x) + 6]}{x^5} \\ &\text{with } \gamma = \frac{(1 + 2\eta)^2}{(1 - \eta)^4}, \delta = \frac{-6\eta(1 + \eta/2)^2}{(1 - \eta)^4} \text{ and } \varepsilon = \frac{\gamma\delta}{2} \end{aligned} \tag{4.25}$$

where η is the hard-sphere volume fraction. It is the volume fraction occupied by the hard spheres with a radius of R_{HS}.

Example curves of $S_{HS}(q)$ are given in Figure 4.13. The curves feature peaks which originate from a spatial ordering in the system. The peaks shift towards low q with increasing R_{HS} (Figure 4.13a), and they become sharper with increasing η (Figure 4.13b).

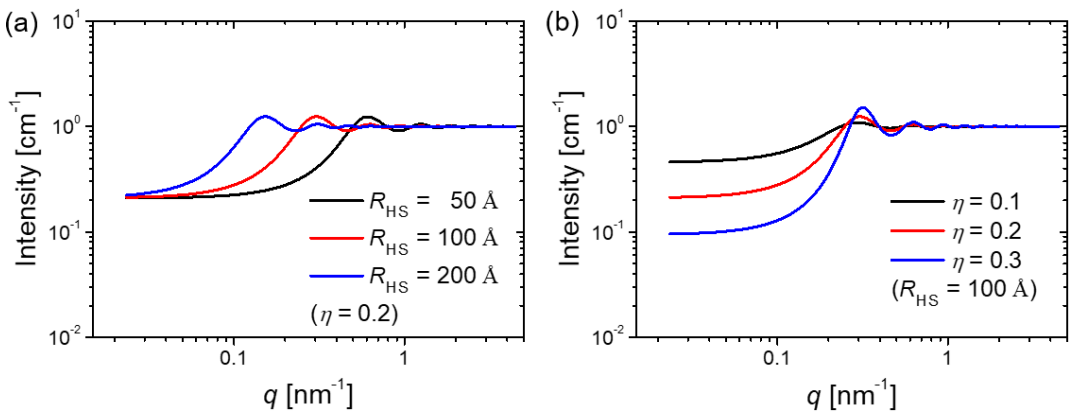

Figure 4.13 Example curves of the Percus-Yevick hard-sphere structure factor $S_{HS}(q)$. (a) Curves with selected values of R_{HS} at fixed η. (b) Curves with selected values of η at fixed R_{HS}.

For chain-like MBs, their interaction is better described by the one between polymer chains, instead of hard spheres. The closest case is the interaction between rigid polymers, which feature large persistence lengths. Such a structure factor was developed using Monte Carlo simulation by Pedersen and Schurtenberger, and was successfully applied to similar systems including worm-like micelles and rigid polymers in solutions [167-174]. It reads [174]:

$$S_{wlc}(q) = \frac{1}{1 + \beta c(q) P_{wlc}(q)} \tag{4.26}$$

where β is the interaction factor, reflecting the interaction strength. For β = 0, there is no interaction, and $S_{wlc}(q)$ = 1; whereas β > 0 hints at the presence of mutual interaction. The relation of β = [1- $S_{wlc}(0)$]/$S_{wlc}(0)$ is fulfilled for the scattering intensity of polymer solutions. $S_{wlc}(0)$, being the structure factor at zero scattering, can be expressed as a function of the reduced concentration $X \approx c/c^*$, where c is the polymer concentration and c^* the overlap concentration of the solution:

$$S_{wlc}{}^{-1}(0) = 1 + \frac{1}{8}\left(9X - 2 + \frac{2\ln(1+X)}{X}\right) \exp\left\{\frac{1}{2.565}\left[\frac{1}{X} + \left(1 - \frac{1}{X^2}\right)\ln(1+X)\right]\right\} \tag{4.27}$$

$c(q)$ in equation 4.26 is the direct correlation function in a multi-particle system, which is chosen to be in the form of the scattering from an infinitely thin rod with a rod length L_{int}:

$$c(q) = 2\frac{\mathrm{Si}(qL_{int})}{qL_{int}} - 4\frac{\sin^2(qL_{int}/2)}{(qL_{int})^2} \tag{4.28}$$

Si(qL_{int}) is the sine integral. The physical meaning of L_{int} in the model is a characteristic interaction length in the system, having a length between the overall chain size and the cross-sectional radius.

Example curves of $S_{wlc}(q)$ are given in Figure 4.14. Different from $S_{HS}(q)$ mentioned above, the curves do not feature peaks from spatial ordering, but a suppressed intensity at low q. The q-range with suppressed intensity shifts towards low q with increasing L_{int} (Figure 4.14a), and the suppression is enhanced with increasing β (Figure 4.14b).

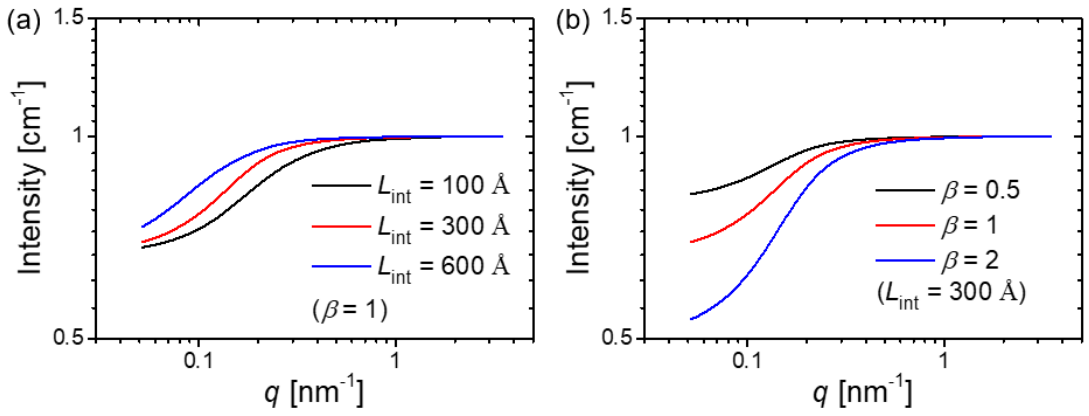

Figure 4.14 Example curves of the structure factor of worm-like chains $S_{wlc}(q)$. (a) Curves with selected values of L_{int} at fixed β. (a) Curves with selected values of β at fixed L_{int}.

Other scattering contributions in MB solutions. Apart from the scattering of MBs and their interaction, scattering contributions from aggregates are often seen in the SAS data of MB solutions. Usually, aggregates do not feature a well-defined shape like a sphere or a cylinder, and their inner structure may resemble a fractal (Figure 4.15). The scattering of aggregates, $I_{agg}(q)$, may be described by the Guinier-Porod empirical model as [175]:

$$I_{\mathrm{agg}}(q) = \begin{cases} \dfrac{I_{\mathrm{G}}}{q^{s}} \exp\left[\dfrac{-(qR_{\mathrm{g,agg}})^{2}}{3-s}\right] \text{ for } q \le q_1 \\ \dfrac{I_{\mathrm{D}}}{q^{\alpha}} \text{ for } q \ge q_1 \end{cases} \tag{4.29}$$

The regions in aggregates that are described by the Guinier term and the Porod term, respectively, are depicted in Figure 4.15. The Guinier term, having a scaling factor of I_G, describes the low q region, giving the radius of gyration of the aggregate, $R_{g,agg}$, and the shape factor, s. s reveals the geometric symmetry of the aggregates with s = 0 for spheres, s = 1 for thin rods, and s = 2 for flat disks. The Porod term, with a scaling factor of I_D, accounts for the

high q region, giving the Porod exponent α. With $1.67 < \alpha < 3$, it describes the mass fractal, and a higher α value indicates a more compact inner structure. For $3 < \alpha < 4$, it refers to the surface fractal, and $\alpha = 3$ stands for rough surfaces, whereas $\alpha = 4$ for smooth surfaces. Furthermore, $\alpha > 4$ could imply a concentration gradient at the surface [176, 177]. During model fitting, q_1 and I_D in equation 4.29 are automatically adjusted by the fitting software to achieve a continuous curve in the full q range, following the equations:

$$q_1 = \frac{1}{R_{g,agg}}\left[\frac{(\alpha - s)(3 - s)}{2}\right]^{1/2}$$
$$I_D = I_G \exp\left[\frac{-(q_1 R_{g,agg})^2}{3 - s}\right] {q_1}^{(\alpha - s)} \qquad (4.30)$$

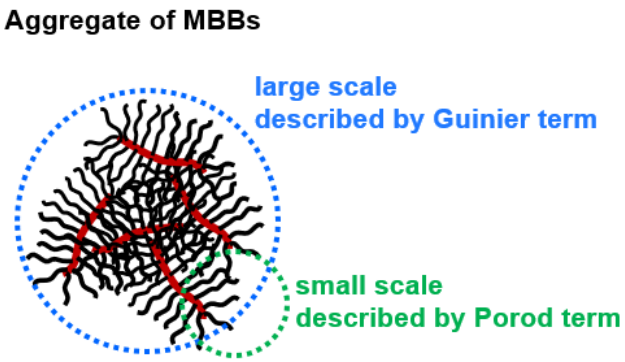

Figure 4.15 Schematic representation of an aggregate of MBs. The regions described by the Guinier term (blue circle) and the Porod term (green circle) are marked out, respectively.

When the aggregates are larger than the detectable length scales of the q range, the SAS data just show the feature of the fractal structure, thus only the Porod term is used. Namely, only the information on the interior structure is acquired, while the overall size and shape of the aggregates cannot be determined in such cases.

Example curves of the Guinier-Porod model are given in Figure 4.16 and Figure 4.17. In the intermediate q range, a decay is present in the curves, which shifts towards low q with increasing $R_{g,agg}$ (Figure 4.16a). For $s = 0$, the curves show no q-dependence at low q, while for $s \neq 0$ they show a linear q-dependence, which becomes steeper with increasing s (Figure 4.16b). α determines the q-dependence at intermediate q, which becomes steeper with increasing α (Figure 4.17).

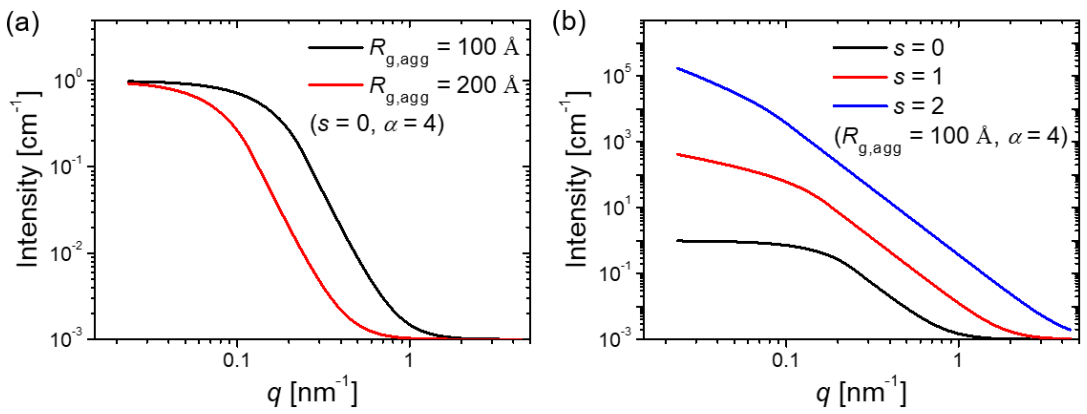

Figure 4.16 Example curves of the Guinier-Porod model with varying parameters from the Guinier term. (a) Curves with selected values of $R_{g,agg}$ at fixed s and α. (b) Curves with selected values of s at fixed $R_{g,agg}$ and α.

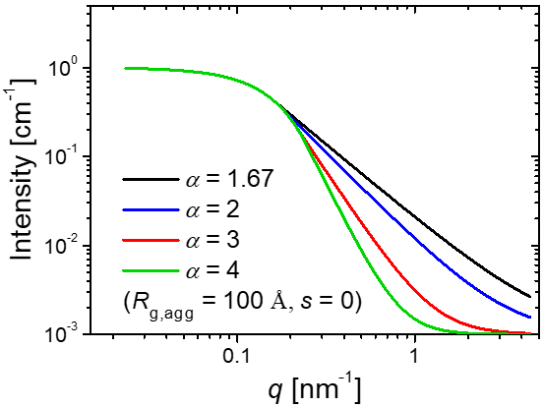

Figure 4.17 Example curves of the Guinier-Porod model with selected values of the Porod exponent α at fixed $R_{g,agg}$ and s.

In the SAS data of MB solutions, the scattering contribution from the local concentration fluctuation, $I_{fluct}(q)$, is often observed at high q. This is attributed to the scattering of the dissolved side chains. As schematically depicted in Figure 4.18, the side chains dangling at the periphery of the MBs are dissolved in the solvent, resulting in a local SLD fluctuation. Such chain scattering can be described by the modified Ornstein-Zernike structure factor [178, 179]:

$$I_{fluct}(q) = \frac{I_{oz}}{1 + (q\xi)^m} \tag{4.31}$$

I_{oz} is a scaling factor. ξ is the characteristic correlation length of the SLD fluctuations. The exponent m is related to the chain conformation and thus provides an indication of the solvent

quality. As $m = 5/3$ is expected for swollen chains in a good solvent, $m = 2$ implies the Gaussian chain conformation in a theta solvent, and $m = 3$ stands for collapsed chains in a poor solvent.

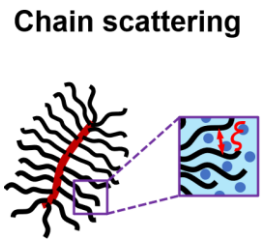

Figure 4.18 Schematic representation of the chain scattering of MBs. The large purple square shows an enlarged view of the periphery region of MB, where the side chains (black curled lines) are dissolved in the solvent (blue dots and blueish background). The red double headed arrow marks the approximate length scale of ξ.

Example curves of the modified Ornstein-Zernike structure factor are given in Figure 4.19. The curves feature a plateau at low q, followed by a smooth decay at high q. The decaying q-position shifts towards low q with increasing ξ (Figure 4.19a), and the decay becomes steeper with increasing m (Figure 4.19b).

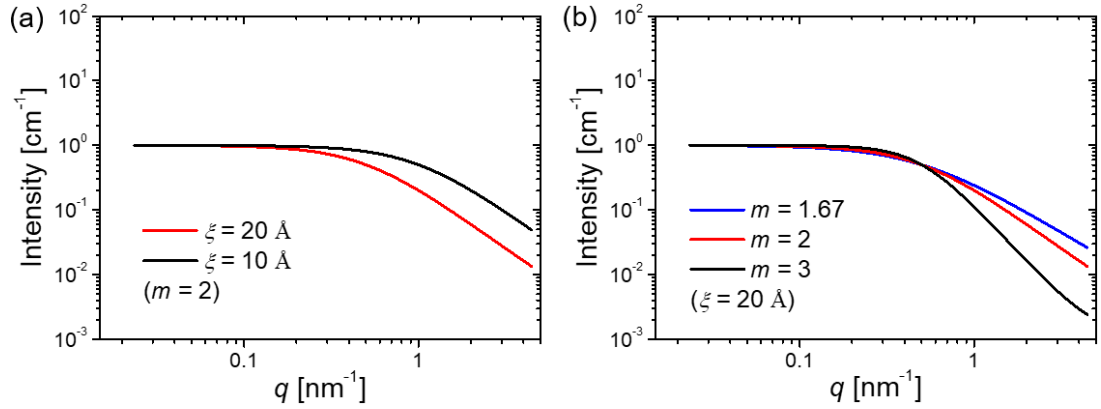

Figure 4.19 Example curves of the modified Ornstein-Zernike structure factor. (a) Curves with selected values of ξ at fixed m. (b) Curves with selected values of m at fixed ξ.

Pair distance distribution function $p(r)$ [149]. In systems containing identical non-interacting particles, e.g., in dilute solutions, $p(r)$ can be calculated from the SAS data, giving the geometrical information of the particles. The principle is introduced as followed. Considering the scattering intensity by a single particle, the scattering amplitude in equation 4.14 can be rewritten by introducing $\boldsymbol{r} = \boldsymbol{r}_1 - \boldsymbol{r}_2$, giving:

$$I_{\mathrm{p}}(\boldsymbol{q}) = |A(\boldsymbol{q})|^2 = \iint_{V_p} \Delta\rho(\boldsymbol{r}_1)\Delta\rho(\boldsymbol{r}_1 - \boldsymbol{r}) \exp(-i\boldsymbol{q}\boldsymbol{r})\, \mathrm{d}\boldsymbol{r}_1 \mathrm{d}\boldsymbol{r}$$

$$= \int \gamma(\boldsymbol{r}) \exp(-i\boldsymbol{q}\boldsymbol{r})\, \mathrm{d}\boldsymbol{r} \tag{4.32}$$

$$\text{with } \gamma(\boldsymbol{r}) = \int_{V_p} \Delta\rho(\boldsymbol{r}_1)\Delta\rho(\boldsymbol{r}_1 - \boldsymbol{r})\mathrm{d}\boldsymbol{r}_1$$

$\gamma(\boldsymbol{r})$ is the spatial autocorrelation function of the particle. Its physical meaning is the probability of finding another point inside the particle at a distance $|\boldsymbol{r}|$ from an arbitrary starting point. Therefore, at a distance $|\boldsymbol{r}|$ larger than the maximum dimension $r_{\max}$ of the particle, $\gamma(\boldsymbol{r}) = 0$. Averaging over all possible directions of $\boldsymbol{r}$, the relation between $I(q)$ and $\gamma(r)$ in one dimension is given to be:

$$I_{\mathrm{p}}(q) = 4\pi \int_0^{\infty} \gamma(r) r^2 \frac{\sin(qr)}{qr} \mathrm{d}r \tag{4.33}$$

The pair distance distribution function, $p(r)$, is introduced as:

$$p(r) = \gamma(r) r^2 \tag{4.34}$$

The value of $p(r)$ at a given r is proportional to the number of pair distances r found within the particle. Thus, the geometry, the symmetry and the dominant lengths of the particle are revealed by $p(r)$. Furthermore, R_{g} of the particle is obtained from $p(r)$ by:

$$R_{\mathrm{g}}{}^2 = \frac{\int_0^{r_{\max}} p(r) r^2 \, \mathrm{d}r}{2\int_0^{r_{\max}} p(r) \, \mathrm{d}r} \tag{4.35}$$

From equation 4.32, it is clearly seen that, the scattering intensity of individual particles is the Fourier transform of its spatial autocorrelation function in terms of the SLD contrast $\Delta\rho(\boldsymbol{r})$. Therefore, it is possible to obtain $p(r)$ from the experimentally measured $I(q)$ by an inverse Fourier transformation:

$$p(r) = \frac{1}{2\pi^2} \int_0^{\infty} I(q) qr \sin(qr)\, \mathrm{d}q \tag{4.36}$$

However, in the practical SAS measurements, the available q range is limited, so p(r) is usually obtained via:

$$p(r) = \frac{1}{2\pi^2}\int_{q_{\min}}^{q_{\max}} I(q)qr\sin(qr)\,\mathrm{d}q \tag{4.37}$$

where q_{max} and q_{min} are the maximum and the minimum q of the experiment data, respectively. Ideally, this q range covers the full length scale of the particle, with the longest dimension r_{max} obeying the condition $r_{max} \times q_{min} < \pi$. Another concern for the $p(r)$ analysis comes from the prerequisite in equation 4.32, that the scattering intensity is exclusively due to the particle scattering $I_p(q)$. However, the measured $I(q)$ in equation 4.37 sometimes contains other scattering contributions, which could be the correlation scattering, i.e., the structure factor, or the scattering of other kinds of particles, e.g., large aggregates. Thus, to gain the geometrical information of individual particles, their scattering, i.e., the form factor, should be isolated from the total scattering.

Instruments and measurement. SAXS measurements were conducted at the high brilliance synchrotron SAXS beamline – P12 at the Deutsches Elektronen Synchrotron (DESY), Hamburg, Germany [180]. The wavelength of the X-ray source was l = 0.124 nm, and the sample-to-detector distance (SDD) was 3.0 m, together providing a q-range of 0.03 – 7 nm^{-1}. The 2D Pilatus 6M detector was used, recording the scattering as 2D intensity pattern. The illumination time for each measurement was 45 ms. During data acquisition, the solution flowed continuously through a thermo-controlled capillary (50 μm in wall thickness and 1.7 mm in inner diameter) for X-ray illumination, using a robotic sample changer [181]. The data were corrected by the transmission, brought to absolute scale using water as a standard. After the 2D intensity being azimuthally averaged, the 1D SAXS data of the solvent is subtracted from that of the sample, delivered by the automated data processing pipeline SASFLOW [182].

SANS measurements were performed at the KWS-1 instrument of the Jülich Centre for Neutron Science (JCNS) at the Heinz Maier-Leibnitz Zentrum (MLZ), Garching, Germany [183, 184]. The neutron wavelength λ was 5 Å ($\Delta\lambda/\lambda$ = 10 %), and the SDDs were 1.5 m, 8.0 m and 20 m, yielding a q-range of 0.02 – 4.5 nm^{-1}. The exposure times were 8 min, 15 min and 30 min at the 3 SDDs, respectively. The samples were loaded in quartz glass cuvettes (Hellma Analytics) with 2 mm neutron path length and 1.25 mm wall thickness, mounted in a Peltier-controlled thermostat. The scattering data were recorded by a scintillation detector having an active area of 60 cm × 60 cm and a spatial resolution of 5.3 mm × 5.3 mm. The scattering intensities were corrected by the transmission and the dark current, and then brought to absolute value using poly(methyl methacrylate). The corrected intensities were azimuthally averaged to

give an intensity plot versus *q*. Finally, the SANS data of the solvent-filled cuvette was subtracted from that of the sample solutions. All the above-described data reduction were carried out with the QtiKWS software by JCNS.

Data analysis. The scattering contributions from different scattering objects, e.g, aggregates or MBs, in the system are added up in the fitting model. These contributions could be a form factor, a form factor multiplied with a structure factor, or the chain scattering. As introduced in the previous paragraphs, the type of form factor and structure factor is chosen according to the structure of the MB under study. Thus, the fitting models used to describe the SAS data for different systems are explained correspondingly in the respective chapters. For model fitting, the software SASfit 0.94.12 [1] was used for the SAXS data analysis, and the software SasView 4.2.2 [185] was used for the SANS data. The $p(r)$ plots were calculated using the software ATSAS 3.0 [186].

4.3 *Cryo*-electron microscopy (*cryo*-EM)

This section is written based on ref [187] and ref [188].

cryo-EM is a type of transmission electron microscopy. It is applied on samples that are prepared to be thin films of sample solution by delicate procedures and cooled to cryogenic temperatures. In a typical *cryo*-EM instrument (Figure 4.20a), the high voltage electron beam, emitted from an electron gun, is controlled by a series of lenses and directed to transmit the sample, enabling the projection images of particles with size as small as few nanometers. The resolution of *cryo*-EM images is generally several tens of angstroms, with the highest resolution being as low as 3 – 4 angstroms [189].

During imaging, the electron beam passes through two condenser lenses, and the condenser aperture filters out the rays that are far from the optical axis. This results in a coherent beam with a narrow energy spread and a small spot size, which then strikes on the sample and is elastically scattered by the atoms composing the particles under investigation. Thus, only a portion of the incident beam is transmitted, which is then focused by the objective lens into an image, while the scattered beam is blocked out by the objective aperture. The image is further enlarged by the projection lens and is visible to the users on the image screen. The *cryo*-EM column is maintained to be evacuated (ideally at ultrahigh vacuum, $< 10^{-9}$ mbar) [190], to

reduce the scattering of the electron beam from the atmospheric environment.

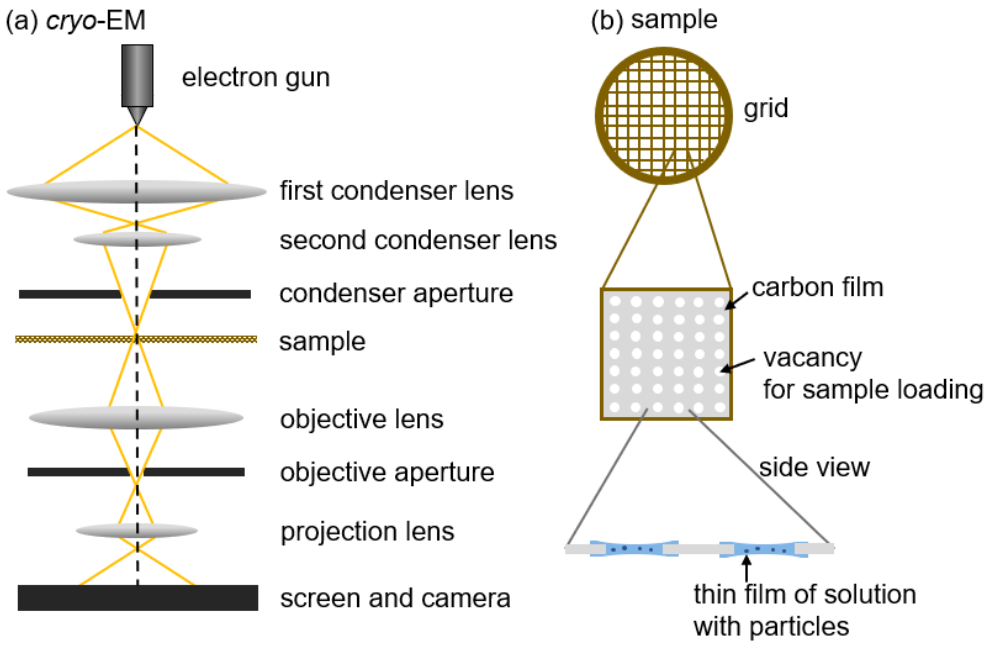

Figure 4.20 (a) Representation of a *cryo*-EM setup. The yellow lines indicate the electron beam. The vertical dashed line indicates the optical axis. (b) Schematic representation of the grid, serving as the sample holder for *cryo*-EM. An enlarged view of the indicated region is drawn and marked out, to show further details in the grid.

Based on the above-described imaging procedure, the brighter region on the image marks the region with lower electron density, whereas the darker region on the image is the region with higher electron density (under bright field mode). Namely, the contrast in a *cryo*-EM image originates from the atomic density and provides information about the appearance and the structure of the particles in the sample.

To account for the vacuum environment, the sample solution is prepared as a free-standing thin film in frozen state with a thickness of few hundred nanometers to few micrometers. During the sample preparation, a small amount of the solution is applied to a metal grid (Figure 4.20b), which supports a holey carbon film. After removing the excess amounts of solution, the grid is dipped into liquid ethane (boiling temperature T_b = -89 °C) for vitrification, where the liquid ethane environment is kept by a liquid nitrogen (T_b = -196 °C) bath. Thus, a thin film of the solution is obtained, in which the particles under investigation are embedded. As a result, under *cryo*-EM, the structure of the nanoparticles is observed, being at the frozen state in solution.

Instrument and measurement. The *cryo*-EM images were taken using a Titan Krios G2

electron microscope, operated at 300 kV. This is equipped with a Falcon 3EC direct detector, a Volta Phase Plate (FEI, now Thermo Scientific), and a Cs Corrector (CEOS GmbH), where the EPU software is used for automated data and the TIA software for manual data collection (FEI, now Thermo Scientific). For the image acquisition, micrograph movies comprising 9-20 frames were recorded in linear and in electron counting mode for high precision. A calibrated magnification of 120k was achieved, with a corresponding magnified pixel size of 0.53 Å, namely a total dose of around 100 electrons per $Å^2$. A few hundred nanometer defocus was applied, using the phase plate for contrast enhancement. The image processing was performed using RELION 2.1 and RELION 3.0 [191, 192], where the MotionCor2 program [193] facilitates the micrograph movie-alignment.

To prepare a frozen thin film of the sample solution for imaging, the samples were applied on the copper grid (trade name: C-Flat 1.2/1.3 4C, Protochips, Morrisville, USA), and were subsequently plunge-frozen with no waiting time. The blot time was set for 2 s, the blot force parameter -1 and the drain time 0 s. The whole procedure was performed in the Vitrobot Mark V (FEI, now Thermo Scientific) environment which allows controlled temperature at 22 °C and humidity of 100 %.

Data analysis. The Fiji image processing package was used for the c*ryo*-EM image analysis [194]. The images were adjusted to show optimized contrast for better recognition of the backbone and side chains of the MBs. Scale bars were labeled, and the real distance between two defined points on the image was calculated.

5. Concentration effect on the structure of a chain-like MB

In the present chapter, the structure of a chain-like MB is studied from dilute to semi-dilute solution in a good solvent.

5.1 Introduction

As discussed in chapter 2.3, the solution concentration *c* systematically affects the end-to-end distance R_{ee} of MBs, where R_{ee} and *c* shows different scaling relations in different concentration regimes. Such effects are especially observable for chain-like MBs, as their overall shape resembles linear polymer chains while the local structure is brush-like.

In the present work, the conformation of a chain-like MB is resolved in dependence on the MB concentration in a good solvent. DLS measurements were carried out on the MB solutions from dilute to semi-dilute condition, so that the diffusional behavior of the MBs is revealed. Furthermore, SAXS data collected in a wide range of concentration disclose the conformational change of the MBs, and the different interaction regimes are resolved.

5.2 Experimental details

Sample preparation. The six samples for DLS measurements are P*i*POx$_{239}$-*g*-P*n*PrOx$_{14}$ solutions in ethanol, where the concentrations are 0.5, 1, 2.5, 5, 10 and 20 g L^{-1}. To prepare solutions with a series of concentrations, the dry polymer powder was firstly dissolved in ethanol at a concentration of 20 g L^{-1}. The as prepared solution was place on the shaker overnight for homogeneous mixing. Then, a portion of the solution at 20 g L^{-1} was taken for further dilution to get the solution at 10 g L^{-1}. The rest of the diluted samples were prepared subsequently in the same manner.

The seven samples for SAXS measurements are solutions at 1.25, 2.5, 10 g L^{-1} in ethanol-d_6 (99.00 %, Deutero GmbH, Kastellaun, Germany), and solutions at 5, 20, 30, 46 g L^{-1} in ethanol. Although different solvent was used, it has been reported that the resulting SAXS curve

will not be heavily affected by the deuteration of ethanol, meaning the overall conformation of the species in the sample does not significantly differ [195]. The preparation procedure is the same as the samples for DLS measurement. Namely, the most concentrated solution was firstly made, and it was later used to prepare the diluted samples.

Before the solution preparation, the solvents had been filtered previously with a syringe filter (pore size 0.8 mm, mixed cellulose ester membrane). The solutions were placed on a shaker for at least two weeks before the measurements to ensure equilibrium.

Dynamic Light Scattering (DLS). For all the sample solutions, DLS data at 17 scattering angles from 30° to 120° were collected, with 3° per step between 30° – 60° and 10° per step between 60° – 120°. At each angle, 20 measurements were performed, and the duration for each was 30 s. The temperature was fixed at 20 °C. The normalized intensity autocorrelation functions, $g_2(\tau,q)$, were analyzed using the modified cumulant method to the third-order, where the normalized field autocorrelation function, $g_1(\tau,q)$, is expressed as equation 4.8.

Small-Angle X-ray Scattering (SAXS). The SAXS data of the MB solutions were collected at 20 °C. For dilute solutions, i.e., 1.25 – 5 g L^{-1}, the fitting model reads:

$$I(q) = P_{\mathrm{fc}}(q) + I_{\mathrm{bk}} \tag{5.1}$$

where $P_{\mathrm{fc}}(q)$ is the flexible cylinder form factor (equation 4.21). I_{bk} is the scattering background.

$P_{\mathrm{fc}}(q)$ is chosen to describe the scattering of a single MB. As the MB studied in this work, P*i*POx$_{239}$-*g*-P*n*PrOx$_{14}$, features a long backbone and relatively short side chains, its conformation in the solution is expected to resemble a semi-flexible polymer chain with a large cross section. From $P_{\mathrm{fc}}(q)$, the contour length L_{c}, the persistence length l_{p} and the cross-sectional radius R_{c} of the MB are obtained. Figure 5.1a shows how each term in equation 5.1 contributes to the total scattering $I(q)$, taking data from the solution at 1.25 g L^{-1} as an example.

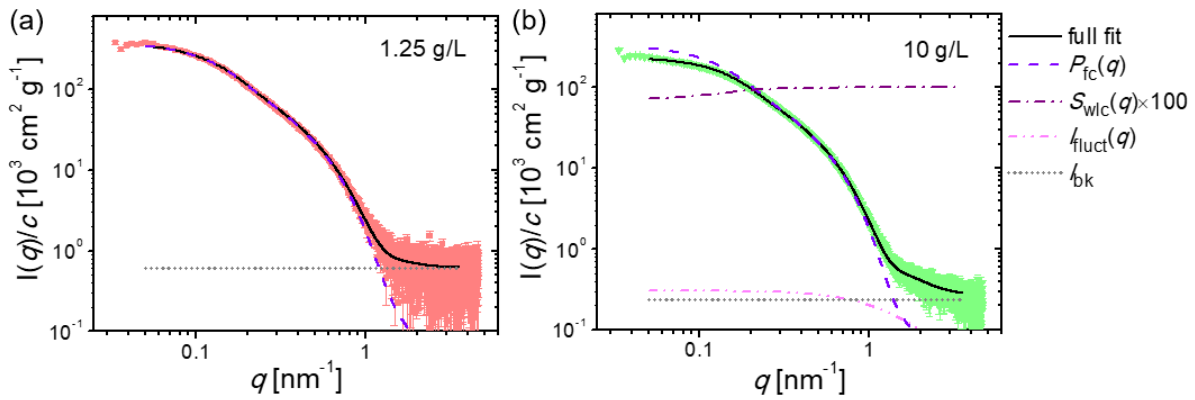

Figure 5.1 Demonstration of model fits to the SAXS data (symbols) of P*i*POx$_{239}$-*g*-P*n*PrOx$_{14}$ solutions in ethanol. (a) Dilute solutions, taking 1.25 g L^{-1} for example, using equation 5.1. (b) Semi-dilute solutions, taking 10 g L^{-1} for example, using equation 5.2.

As for the semi-dilute solutions, i.e., 10 – 46 g L^{-1}, the contribution from the interaction between the MBs and the chain scattering are additional included in the fitting model:

$$I(q) = P_{\mathrm{fc}}(q)S_{\mathrm{wlc}}(q) + I_{\mathrm{fluct}}(q) + I_{\mathrm{bk}} \tag{5.2}$$

where $S_{\mathrm{wlc}}(q)$ is the structure factor describing the interaction between worm-like chains (equation 4.26), and $I_{\mathrm{fluct}}(q)$ is the scattering from the local density fluctuation (equation 4.31).

$S_{\mathrm{wlc}}(q)$ is multiplied with $P_{\mathrm{fc}}(q)$ to account for the correlation between the chain-like MBs, giving the interaction factor β, and a characteristic interaction length L_{int}. As $S_{\mathrm{wlc}}(q)$ is defined to contain $P_{\mathrm{fc}}(q)$, it is thus dependent on the MB conformation. The contribution from the local concentration fluctuation, $I_{\mathrm{fluct}}(q)$, is described by the Ornstein-Zernike structure factor, with the exponent fixed at 2. It presumably accounts for the scattering from the side chains, giving the correlation length ξ of the concentration fluctuation. Figure 5.1b demonstrates the contributions from each term in equation 5.2 to the SAXS data, taking data from the solution at 10 g L^{-1} as an example. I_{bk} is taken as a free fitting parameter for the dilute solutions, i.e., 1.25 – 5 g L^{-1}, while it is fixed at 2.36 × 10^{-4} cm^2 g^{-1} for the semi-dilute solutions, i.e., 10 – 46 g L^{-1}. The software SASfit 0.94.12 was used for model fitting [1].

5.3 Diffusional behavior

To investigate the diffusional behavior of P*i*POx$_{239}$-*g*-P*n*PrOx$_{14}$ from dilute to semi-dilute

condition, DLS measurements were performed on its six solutions at 20 °C in ethanol, where the concentration ranges from 0.5 to 20 g L^{-1}. For each solution, data were collected at a total of seventeen scattering angles 2θ between 30° – 120°. The normalized intensity autocorrelation curves at four selected scattering angles, 2θ = 30°, 60°, 90° and 120°, are shown in Figure 5.2 along with the fitting lines. It is clearly demonstrated that, the relaxation time τ_D, defined by the decay position of the curve, is dependent on 2θ.

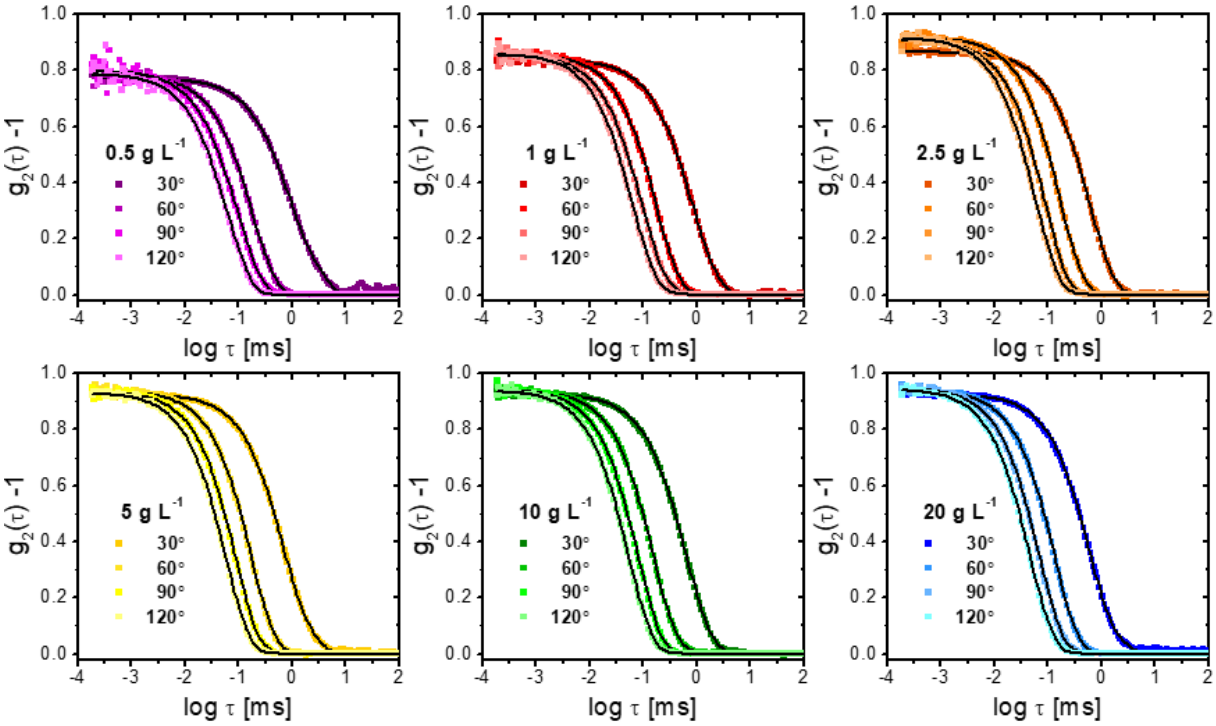

Figure 5.2 The representative normalized intensity autocorrelation data (symbols) along with the fitting lines (solid lines) of P*i*POx$_{239}$-*g*-P*n*PrOx$_{14}$ solutions from 0.5 to 20 g L^{-1} in ethanol. The solution concentration and the scattering angles are indicated in the legend.

The relation between τ_D and 2θ is further used to characterize the diffusional motion of the MBs, by plotting the mean relaxation rate $\Gamma = 1/\tau_D$ as a function of q^2. It is found that, a nice linear trend between Γ and q^2 is shown for all the samples (Figure 5.3), regardless of the varying solution concentration. The linear relation indicates that only translational motion of the MBs is observed in the q range, while no internal modes of motion is detected. The result, however, is unexpected, since the architecture of P*i*POx$_{239}$-*g*-P*n*PrOx$_{14}$ suggests an anisotropic shape due to the vastly different backbone and side chain length, which might lead to non-translational diffusion especially in dilute solution.

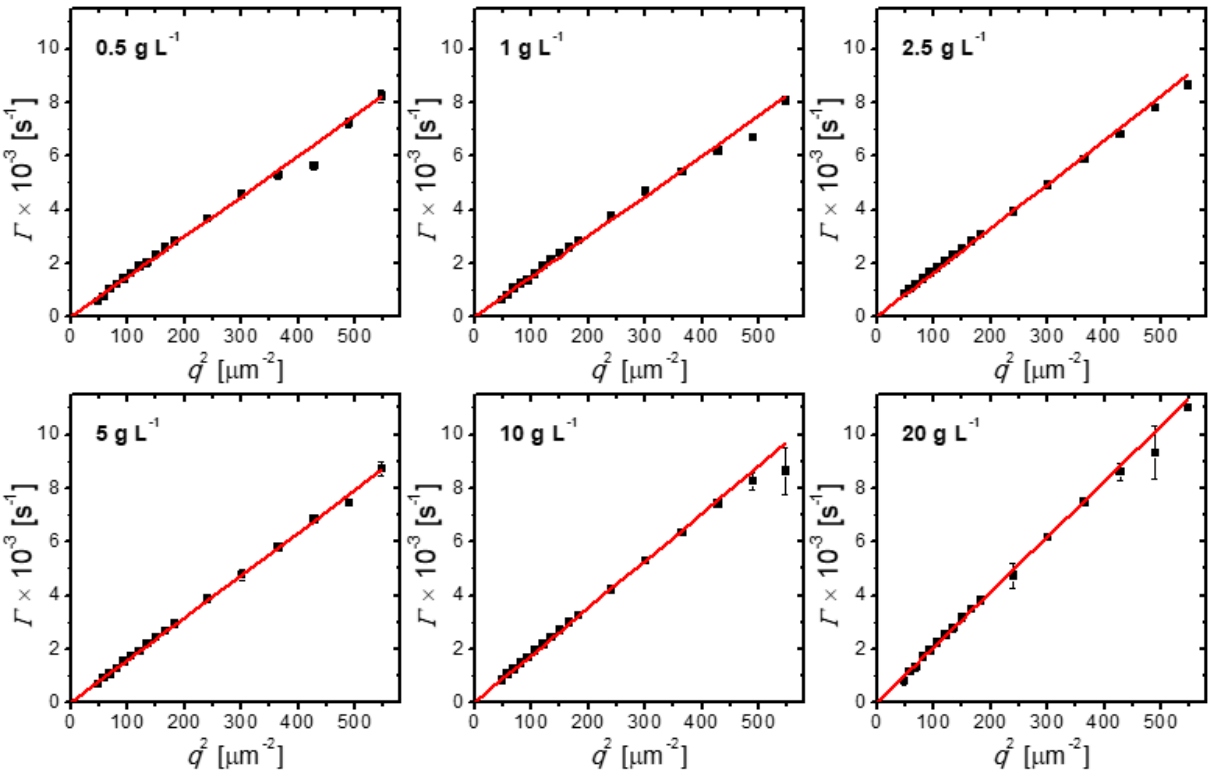

Figure 5.3 The mean relaxation rate Γ versus q^2 of P*i*POx$_{239}$-*g*-P*n*PrOx$_{14}$ solutions from 0.5 to 20 g L^{-1} in ethanol. The solution concentration is indicated on each figure. The red straight lines are the linear regressions, passing through the origin.

From the Γ vs. q^2 plots, the translational diffusion coefficient D of the MB (Figure 5.4) is given by the slope of the linear regression (red straight lines in Figure 5.3). It is important to note that, for particle-like samples, the hydrodynamic radius R_h at different concentrations can be directly derived from the corresponding D using the Stokes-Einstein equation (equation 4.7), whereas for polymer solutions or chain-like samples, this is not the case. For chain-like samples, the self-diffusion coefficient at infinitely dilute solution, D_0, should be used to calculate the hydrodynamic radius of infinite dilution $R_{h,0}$. In such systems, the relation of $D = D_0(1 + k_D \times c)$ applies, as introduced in equation 4.11, and a regression line to the experimental data of D vs. c (red straight line in Figure 5.4) provides D_0 by the y-intercept. It results in $D_0 = 15.1 \pm 0.3$ μm^2 s^{-1}, and thus $R_{h,0} = 12.2 \pm 0.3$ nm is obtained for the MB.

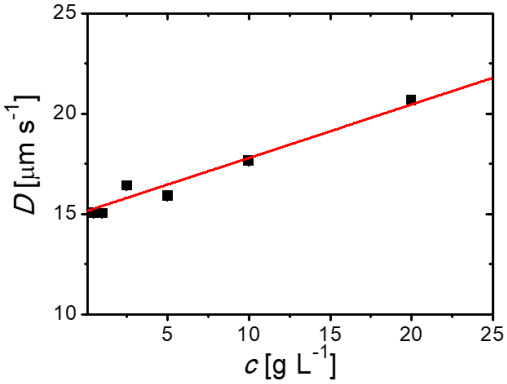

Figure 5.4 The relation between the translational diffusion coefficient D (symbols) and the concentration c for P*i*POx$_{239}$-*g*-P*n*PrOx$_{14}$ in ethanol from 1.25 to 20 g L^{-1}. The red straight line is a linear regression.

From the DLS data, pure translational motion is found for the MB in the concentration range of 0.5 – 20 g L^{-1}, with its hydrodynamic radius of infinite dilution being disclosed. However, it is still unclear whether the MBs feature an anisotropic shape in dilute solution or not. Moreover, their shape evolution upon variation of concentration remains unsolved. Therefore, a structural study is necessary to gain a better understanding of the system. This is realized by the small-angle scattering measurements described in the next section.

5.4 Structural changes upon enhanced mutual interaction

SAXS measurements were performed on P*i*POx$_{239}$-*g*-P*n*PrOx$_{14}$ solutions in a concentration range from 1.25 to 46 g L^{-1} at 20 °C. The concentration range is chosen to cover most of the concentrations in the DLS measurements, while higher concentrations are reached for a more complete observation on the scaling relation between the molecular size and the polymer concentration.

The SAXS data of the most dilute sample, i.e., 1.25 g L^{-1}, is shown in Figure 5.5a, which has the typical scattering features of worm-like particles. In the low q range (q < 0.08 nm^{-1}), where structure at large scales is reflected, the scattering intensity $I(q)$ is a plateau, and its absolute value determines the contour length L_c of the MB. At intermediate q (0.1 < q < 0.5 nm^{-1}), the relation of $I(q) \sim q^{-5/3}$ is observed, indicating a self-avoiding-walk of the segmental length [196]. For polymer chains dissolved in a good solvent, the SAXS data usually features $I(q) \sim q^{-5/3}$, and the segment length is characterized as the persistence length l_p, which can be

applied to the chain-like MB. Further at $0.7 < q < 1.5$ nm^{-1}, $I(q)$ shows a decay of $I(q) \sim q^{-4}$. This is a result from the finite cross section of the MB, formed by the densely-grafted side chains on the backbone. The decaying q position implies the length scale of the cross-sectional radius R_c. At $q > 1.5$ nm^{-1}, $I(q)$ is independent of q, which is considered as the background scattering.

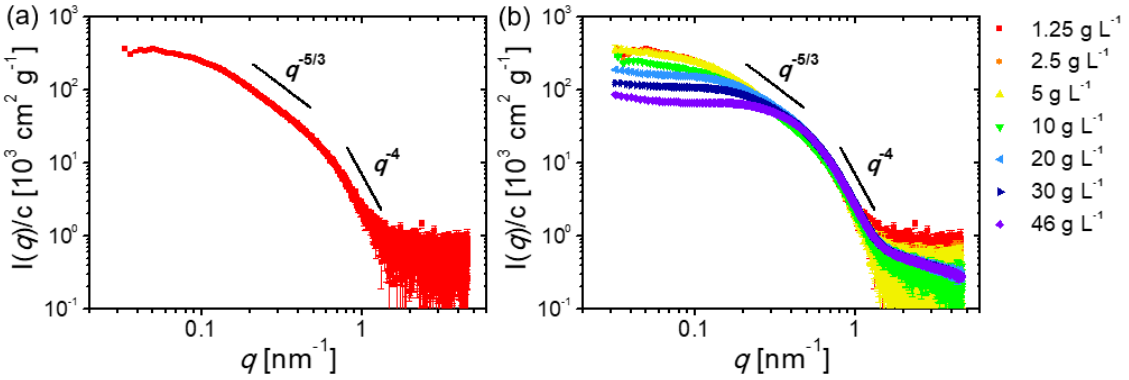

Figure 5.5 The concentration normalized SAXS data (symbols) of the P*i*POx$_{239}$-*g*-P*n*PrOx$_{14}$ solutions at 20 °C in ethanol. (a) 1.25 g L^{-1}. (b) 1.25 – 46 g L^{-1}. The concentrations of the corresponding symbol color/shape are indicated in the legend. In the intermediate q and the high q region, lines corresponding to $I(q) \sim q^{-5/3}$ and $I(q) \sim q^{-4}$ are drawn, respectively.

In Figure 5.5b, SAXS data of all samples are shown, normalized by concentration. From 1.25 g L^{-1} up to 5 g L^{-1}, the curve stays nearly unchanged. Above 5 g L^{-1}, the low q scattering intensity is successively suppressed with increasing concentration. Furthermore, the relation of $I(q) \sim q^{-5/3}$ at intermediate q gradually disappears (see Figure 5.6 for the vertically shifted data), implying a change in l_p. In the range of $0.7 < q < 1.5$ nm^{-1}, SAXS data overlap for all concentrations, indicating a constant R_c. At the highest q range, namely $q > 1.5$ nm^{-1}, $I(q)$ stays independent of q from 1.25 up to 5 g L^{-1} (Figure 5.6a), while a shallow decay of $I(q)$ is recognizable from 10 to 46 g L^{-1} (Figure 5.6b). This shallow decay is attributed to the concentration fluctuations at small length scales, which are presumably caused by the side chain scattering and are observable when the concentration is high enough. At the high q range, the data from 10 to 46 g L^{-1} overlap very well, suggesting that the scattering from the side chains hardly depend on concentration.

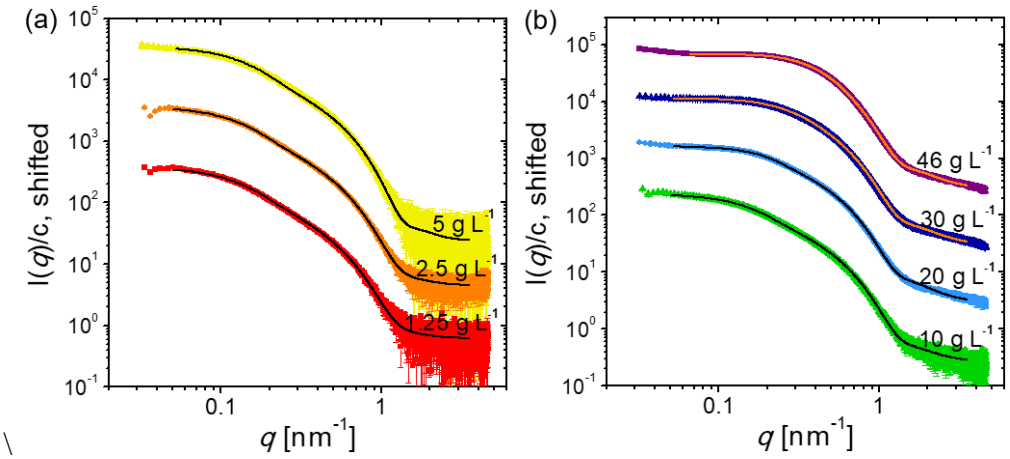

Figure 5.6 SAXS data (symbols) of the P*i*POx$_{239}$-*g*-P*n*PrOx$_{14}$ solutions at 20 °C in ethanol, shown together with the model fits (solid lines). (a) The dilute solutions (b) The semi-dilute solutions. The concentrations are indicated in the graphs. The data are vertically shifted by a factor of 10 with respect to each other for better visibility.

From the SAXS data, the pair distance distribution functions, $p(r)$, are derived (Figure 5.7a), giving hints to the overall geometry of the MBs at various concentrations. The $p(r)$ function of the most dilute sample, c = 1.25 g L^{-1}, is asymmetric. It shows two maxima at the pair distances r = 5 nm and r = 11 nm, and the curve decays steadily between r = 11 – 47 nm. Upon increasing concentration to 10 g L^{-1}, the $p(r)$ function stays overall asymmetric. The maximum at r = 5 nm is unchanged, while the one at r = 11 nm becomes shallower and nearly disappear. Meanwhile, the decaying distribution at r > 11 nm gradually shifts toward lower r-values by around 3-5 nm, meaning the r_{max} slightly shrinks. The asymmetric shape of $p(r)$ implies that the MB features an anisotropic geometry, and the two maxima are possibly related to the segmental length of the MB. For a precise analysis, the physical meaning of these two pronounced r should be disclosed after the structural parameters are resolved by model fitting the SAXS data.

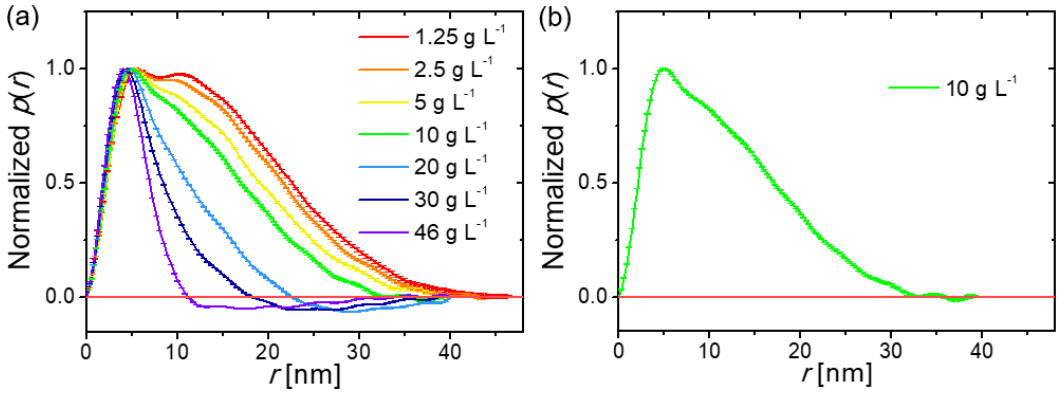

Figure 5.7 Normalized pair distance distribution functions, $p(r)$, of the P*i*POx$_{239}$-*g*-P*n*PrOx$_{14}$ solutions in ethanol. (a) 1.25 – 46 g L^{-1}. (b) 10 g L^{-1}. The horizontal red solid line indicates $p(r) = 0$.

At 10 g L^{-1}, the $p(r)$ plot shows negative values at r = 35 – 40 nm (Figure 5.7b), indicating the presence of the correlation scattering in the data. This means, the SAXS data not only contain the scattering of the MBs, i.e., the form factor, but also the structure factor. The influence from the interference scattering becomes more obvious for the data at higher concentrations, as the $p(r)$ plots obviously show negative values (Figure 5.7a). Thus, the plots above 10 g L^{-1} do not directly reflect the conformational information of individual MBs unless the form factor scattering can be isolated from the total scattering. This is intendedly achieved by model fitting the SAXS data, described in the following content.

For model fitting, the form factor, describing the scattering of the MB, is chosen to be the flexible cylinder form factor $P_{fc}(q)$. It gives the conformational parameters, including L_c, l_p and R_c of the chain-like MB. Above 10 g L^{-1}, $P_{fc}(q)$ is multiplied by the structure factor of the worm-like chain $S_{wlc}(q)$, which applies the L_c and l_p from $P_{fc}(q)$. Namely, $S_{wlc}(q)$ describes the interaction between semi-flexible chains featuring the exact conformational parameters from $P_{fc}(q)$. From $S_{wlc}(q)$, an interaction factor β, revealing the interaction strength, and the interaction length L_{int} are obtained. The scattering from the side chains, namely the intensity tail at q > 1.5 nm^{-1} (Figure 5.6b), is modeled by the Ornstein-Zernike structure factor, from which the correlation length ξ of the local density fluctuation in the solution is given. With the described model (equations 5.1 and 5.2), nice fits were obtained (Figure 5.6, solid lines).

By fitting the data, $P_{fc}(q)$ is isolated from the total scattering for each sample (Figure 5.8a). The $p(r)$ plots derived from these $P_{fc}(q)$ curves (Figure 5.8b) are supposed to contain only the conformational information of the MB. It is found that, from 1.25 to 20 g L^{-1}, the $p(r)$-functions

are asymmetric, and they shift to slightly smaller *r*-values with increasing concentration. Further, from 20 to 46 g L^{-1}, the *p*(*r*)-functions become steadily less asymmetric, while they substantially shift to smaller *r*. The asymmetric *p*(*r*)-functions suggest an anisotropic overall shape of the MBs at all concentrations, and the changes from 1.25 to 46 g L^{-1} indicate a gradual shape transition from an extended coil to a prolate ellipsoid.

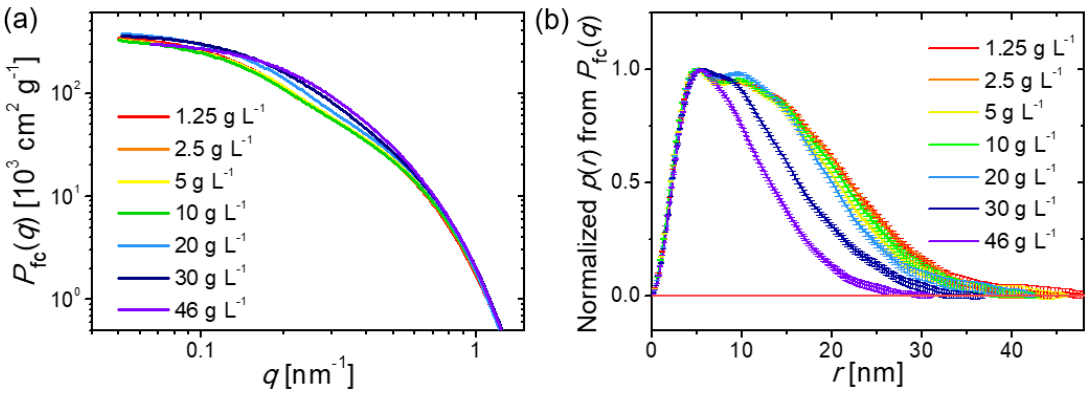

Figure 5.8 (a) Curves of the flexible cylinder form factor $P_{fc}(q)$ obtained by model fitting the SAXS data of P*i*POx$_{239}$-*g*-P*n*PrOx$_{14}$ solutions. (b) Normalized pair distance distribution functions, *p*(*r*), derived from $P_{fc}(q)$. The horizontal red solid line indicates *p*(*r*) = 0.

The analysis result at 1.25 g L^{-1} gives L_c of the MB to be 56.7 nm with an uncertainty of 1.5 nm. Meanwhile, an estimate of L_c can be obtained by multiplying the total degree of polymerization along the MB, i.e., $N_{bk} + 2N_{sc}$, with the monomer length, which is calculated based on the C-C and C-N chemical bonds and the bond angles [197]. Such estimation provides the contour length of the MB having a fully stretched conformation to be 66.75 nm. Thus, the experimentally obtained L_c is 84.9 % of the fully extended length, implying a rather stretched chain conformation of the backbone. Since L_c is supposed to be independent on the solution concentration, L_c = 56.7 nm is applied to all the samples.

The radius of gyration, R_g, of the MB (Figure 5.9) is obtained from the *p*(*r*)-functions of $P_{fc}(q)$ (with equation 4.35). From 1.25 up to 20 g L^{-1}, R_g stays unchanged at around 11.5 nm. This, together with the $R_{h,0}$ from DLS, results in the characteristic ratio $R_g/R_{h,0}$ = 0.94, providing hints to the structural compactness as well as the geometric symmetry of the MB. For solid spheres, $R_g/R_{h,0}$ = 0.775 is obtained. For elongated particles and rod-like particles, $R_g/R_{h,0}$ ranges from 1 to 2 or even above, depending on the aspect ratio between the longitudinal to the

perpendicular length. For polymers, the degree of branching will make an influence on $R_g/R_{h,0}$. For example, polymers as random coils usually show $R_g/R_{h,0}$ = 1.1 – 1.6 [198, 199], while $R_g/R_{h,0}$ of the highly grafted polymer is suppressed to values less than 1 [200]. For the P*i*POx$_{239}$-*g*-P*n*PrOx$_{14}$ MB, the $R_g/R_{h,0}$ value of 0.94 fits the value expected for a highly grafting polymer. This result reflects the significance of the side chains on the geometry of the MB. From 20 to 46 g L^{-1}, R_g decreases with increasing c, with the scaling relation of $R_g \sim c^{-0.8}$ (Figure 5.9). As reviewed in chapter 2.3, based on the theoretical prediction, the scaling exponent of -0.8 suggests the dominant role of the inter- and intra- side chain interactions between the MBs. Noticeably, neither the scaling regime of the backbone interaction nor the one of the persistence segments are observed here. This might be attributed to the molecular architecture, i.e., the side chains are grafted on the backbone with a high density and are long enough to influence the overall structure of the MB.

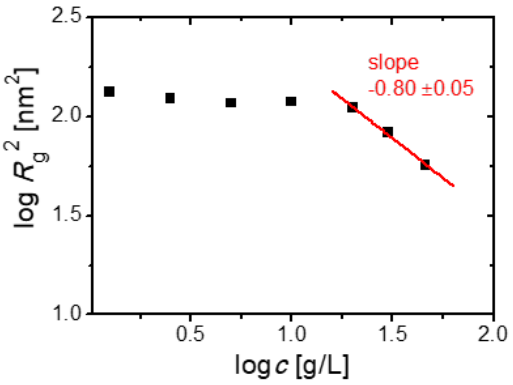

Figure 5.9 Radius of gyration R_g as a function of concentration c of P*i*POx$_{239}$-*g*-P*n*PrOx$_{14}$ solutions in ethanol from 1.25 to 46 g L^{-1}. The red straight line is a linear regression of the data points from 20 to 46 g L^{-1}.

The dependence of l_p on c is also resolved (Figure 5.10). Its value stays constant from 1.25 g L^{-1} up to 10 g L^{-1}, being around 10 nm. This is close to the maximum at $r \approx 11$ nm in the $p(r)$-functions (Figure 5.8b). Thus, based on the model fitting result, the maximum at $r \approx 11$ nm in the $p(r)$-functions can be attributed to the segmental persistence length along the MB. Comparing with the l_p value of the bare linear backbone, being around 1.5 nm [201-204], the l_p of the MB is significantly larger, implying an increase of the main chain rigidity due to the dense grafting of the side chains. Above 10 g L^{-1}, l_p steadily decreases with increasing c until it reaches 3 nm at 46 g L^{-1} (Figure 5.10). This means, the rigidity of the MB is severely weakened, which is supposedly a result of the enhanced mutual interaction between the MBs [40].

Interestingly, the concentration where l_p starts to decrease, i.e., 10 g L^{-1}, is slightly mismatched with the one observed in R_g (Figure 5.9), i.e., 20 g L^{-1}. It indicates that the rigidity decreases a bit prior to the decrease of the overall size upon increasing c. Still, based on the c-dependence of R_g as well as l_p, it is fair to state that the overlap concentration c^* of the solution could possibly fall in the range of 10 – 20 g L^{-1}.

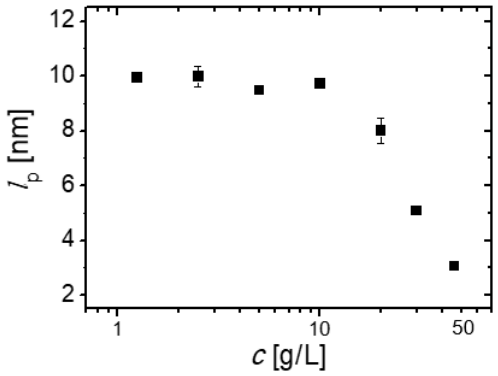

Figure 5.10 Persistence length l_p as a function of concentration c of P*i*POx$_{239}$-*g*-P*n*PrOx$_{14}$ solutions in ethanol from 1.25 to 46 g L^{-1}.

In the theoretical estimation on the chain size of rigid polymers, the predicted radius of gyration R_{g_theo} is expressed as a function of L_c and l_p by the equation [205]:

$$R_{g\_theo}{}^2 = \frac{L_c l_p}{3} - l_p{}^2 + \frac{2 l_p{}^3}{L_c} - 2(1 - e^{-\frac{L_c}{l_p}}) \frac{l_p{}^4}{L_c{}^2} \qquad (5.3)$$

In Figure 5.11, R_{g_theo} with defined L_c (56.7 nm) is plotted against l_p (values from Figure 5.10), which is shown together with the R_g values obtained from $p(r)$. It turns out that the R_g from $p(r)$ nearly coincide with the theoretical curve. Still, it should be noted that the conformational behavior of MBs might not be exactly the same as rigid linear polymers, since the effect from the large cross section of MBs is not considered in equation 5.3, This might be the reason for the slightly higher R_g than the theoretical values at the same l_p.

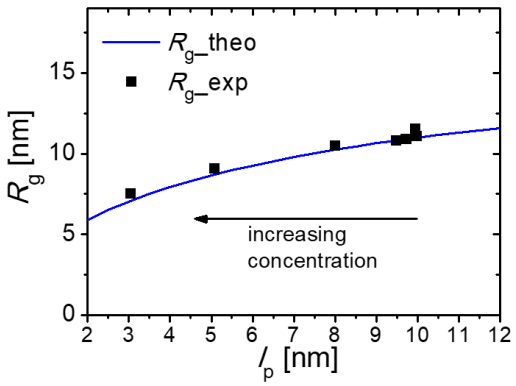

Figure 5.11 Theoretically predicted radius of gyration R_{g_theo} against persistence length l_p of rigid polymer chains (blue smooth curve) based on equation 5.3, in comparison with the experimental R_g value (black squares). The arrow points at the direction of increasing solution concentration.

In the measured concentration range, R_c fluctuates around 2.5 nm without obvious trend (Figure 5.12a). Cross-comparing with the maxima *r*-values in the *p*(*r*)-functions (Figure 5.8b), the cross-sectional diameter, i.e., 5 nm, is found to correspond very well to the maximum at $r \approx 5$ nm in the *p*(*r*)-functions for all concentrations. Thus, the cross section of the MB is supposed to be responsible for the maxima at $r \approx 5$ nm in the *p*(*r*)-functions. At similar length scales of the cross section, the correlation length ξ, from the Ornstein-Zernike structure factor, characterizes the local concentration fluctuation presumably from the side chains at the periphery of the MBs. This is found to be around 1 nm (Figure 5.12b), showing no clear dependence on *c*. In general, these two structural parameters at small length scales in the MB hardly change, implying a stable local structure upon variation of the solution concentration.

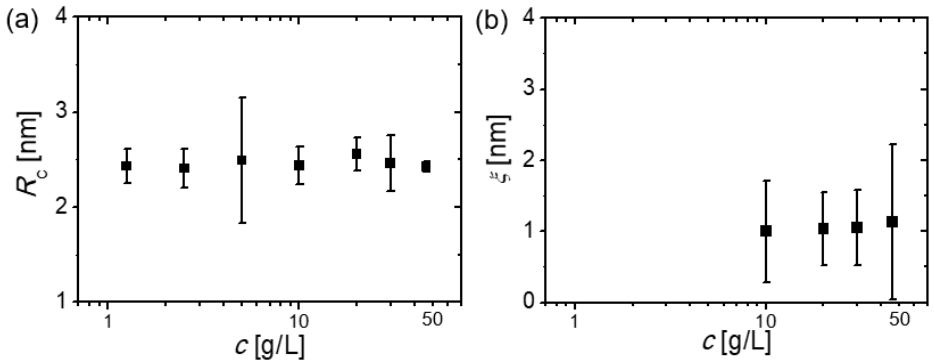

Figure 5.12 Structure parameters at small length scales of P*i*POx$_{239}$-*g*-P*n*PrOx$_{14}$ solutions in ethanol from 1.25 to 46 g L^{-1}. (a) Cross-sectional radius R_c and (b) correlation length ξ

as a function of concentration *c*.

Considering now the variation of the correlation between individual MBs in the solution, to draw a picture of the influence from the mutual interaction on the MB conformation. The average distance between MBs, $D_{avg,}$, is plotted (Figure 5.13, smooth curve). It is estimated by the solution concentration [g L^{-1}], where the number of MBs in a unit volume is calculated and converted to the space occupied by each MB. D_{avg} is compared with the size of the MBs, r_{max} (Figure 5.13, symbols), where r_{max} is taken as the largest *r*-value in the *p*(*r*)-functions (Figure 5.8b) at the corresponding concentration. Plotting D_{avg} and r_{max} together, an intersection at around 10 g L^{-1} is shown. This essentially means that the MBs are isolated from each other below 10 g L^{-1}, while they experience the mutual interference above 10 g L^{-1}, and such result furthermore confirms the deduction in the previous discussion that c^* = 10 – 20 g L^{-1}. Between 20 – 46 g L^{-1}, D_{avg} is larger than r_{max}, attributed to the coil-like shape or the anisotropic shape of the MBs.

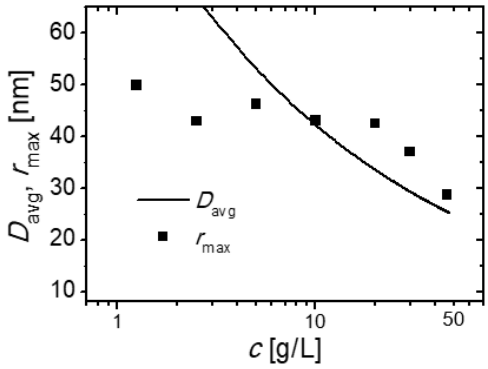

Figure 5.13 Comparison between the average distance between individual MBs, D_{avg} (smooth curve), and the largest dimension within a MB, r_{max} (symbols), as a function of concentration *c* of P*i*POx$_{239}$-*g*-P*n*PrOx$_{14}$ in ethanol from 1.25 to 46 g L^{-1}.

For SAXS data above 10 g L^{-1}, the structure factor is involved, indicating the presence of the interference between MBs in the solution. In the fitting model, the structure factor describing interaction between worm-like polymer chains, $S_{wlc}(q)$, is combined with $P_{fc}(q)$, where $S_{wlc}(q)$ contains the structural parameters from $P_{fc}(q)$, i.e., L_c and l_p. The returned parameters from $S_{wlc}(q)$ are L_{int}, which marks a characteristic length scale between the overall size and the cross section of the MB, and β, which is positively related to the interaction strength between the MBs. The resulting L_{int} shows a decrease upon increasing *c* (Figure 5.14a), and the

values fall into the reasonable length range between r_{max} (Figure 5.13, symbols) and R_c (Figure 5.12a). β increases with increasing c (Figure 5.14b, symbols), reflecting the enhanced interaction strength. Using the relation of $\beta = [1- S_{wlc}(0)]/S_{wlc}(0)$ in combination with equation 4.27, assuming $c^* = 10$ and 20 g L^{-1}, theoretical plots of β are obtained as a function of c (Figure 5.14b, blue curve and black curve, respectively). The experimental data falls nicely in the range within the two theoretical curves, which justifies the validity of $S_{wlc}(q)$ in the MB solution system.

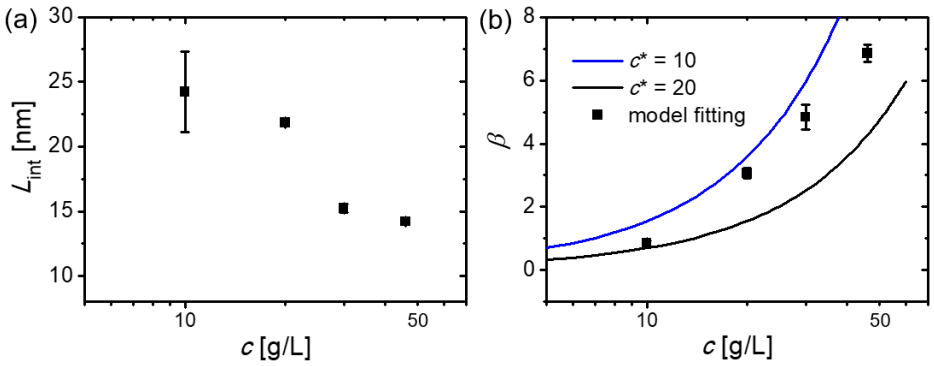

Figure 5.14 Structural parameters from the structure factor of worm-like chains $S_{wlc}(q)$, obtained by model fitting the SAXS data of the P*i*POx$_{239}$-*g*-P*n*PrOx$_{14}$ solution in ethanol from 1.25 to 46 g L^{-1}. (a) Characteristic interaction length L_{int}. (b) Interaction parameter β (symbols). The theoretical curves of β, assuming $c^* = 10$ g L^{-1} (blue curve) and $c^* = 20$ g L^{-1} (black curve).

Based on the structural analysis results from SAXS, the conformational change of P*i*POx$_{239}$-*g*-P*n*PrOx$_{14}$ in dependence on solution concentration in a good solvent can be drawn, as in Figure 5.15. It has a worm-like shape in dilute solution, and the structure is unchanged up to 10 g L^{-1}. At 20 g L^{-1}, while the overall size is similar to the one as in dilute solution, l_p gets shorter. As the concentration increases from 20 to 46 g L^{-1}, both the brush size and l_p decrease steadily upon increasing concentration, resulting in a reduced backbone rigidity of the MB. Despite of the significant changes of the overall size and l_p, the crosse section formed by the densely grafted side chains keeps its dimension all along during the variation of concentration.

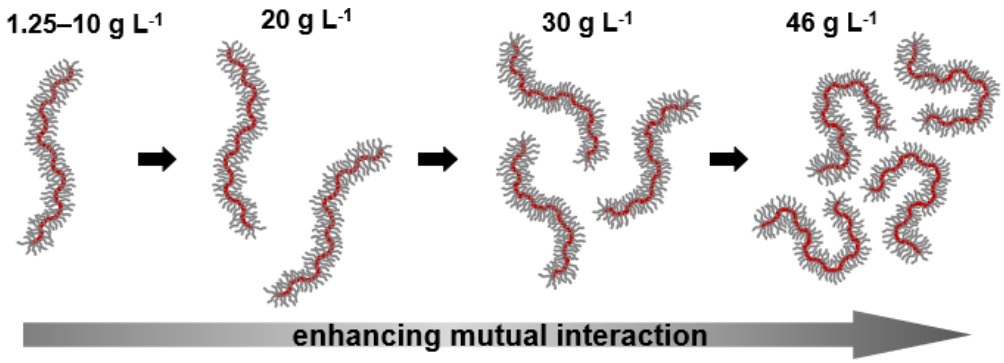

Figure 5.15 Schematic representation of the structural evolution upon increasing solution concentration of the chain-like MB, P*i*POx$_{239}$-*g*-P*n*PrOx$_{14}$, in a good solvent. The black arrows point at the direction of increasing concentration.

5.5 Conclusion

The diffusional behavior and the conformation of a chain-like MB, P*i*POx$_{239}$-*g*-P*n*PrOx$_{14}$, is resolved in dependence on the solution concentration in ethanol, which is a good solvent. The DLS data reveal that, the MBs perform the pure translational motion in the concentration range of 0.5 – 20 g L^{-1}, i.e., from dilute to semi-dilute condition. The hydrodynamic radius $R_{h,0}$ from DLS, together with R_g from SAXS, give the value of the characteristic ratio $R_g/R_{h,0}$ = 0.94, indicating the highly branched structure and the important role of the side chains on the MB geometry. Using SAXS, its conformation is found to resemble a worm-like chain with a large cross section in the dilute and unperturbed state. This conformation persists from 1.25 up to 10 g L^{-1}. Above 10 g L^{-1}, the MB conformation is influenced by the mutual interaction between the MBs, and a rigid-to-soft transition of the backbone rigidity is observed, which is driven by the interaction between the side chains. Namely, a direct transition from the non-interacting state to the side chain interaction state is found, while neither the backbone interaction nor the persistence length interaction state are observed. The result is tentatively attributed to the dominant role of the side chains in the architecture of the MB.

6. Structural investigation on MB with LCST homopolymer side chains

In this chapter, the thermoresponsive behavior of a MB with lower critical solution temperature (LCST) homopolymer side chains is investigated in terms of the structural changes. The main results in this chapter were previously published in J.-J. Kang et al., *Colloid Polym. Sci* **2021**, *299*, 193-203 [206].

6.1 Introduction

As discussed in chapter 2.4, when the thermoresponsive polymers are attached to the backbone of the MB as its side chains, their thermoresponsivity will be largely influenced by the dense-grafting architecture. Furthermore, the structural evolution of the MB upon variation of temperature is dependent on the architecture of the MBs, i.e., the length ratio between the backbone and the side chains. In the present work, a MB with the LCST side chains, poly(2-ethyl-2-oxazoline) (PEtOx), is studied in an aqueous solution. The MB has a unique length ratio between the backbone and the side chain lengths, and it supposedly features a shape between a prolate to a cylinder at the dissolved state, i.e., at low temperatures. Due to such length ratio, the MB is expected to show a non-typical structural change upon heating.

The LCST behavior of the MB is investigated at 30 g L^{-1} in D_2O. DLS as well as SANS measurements were performed on the MB solution during a temperature scan, and the data reveal the influence of the continuous dehydration of the LCST side chains on the structure of the MB.

6.2 Experimental details

Sample preparation. The sample for both DLS and SANS measurements is a P*i*POx_{100}-*g*-$PEtOx_{17}$ solution in D_2O at 30 g L^{-1}. During preparation, the dry polymer powder was dissolved in D_2O (99.95 %, Deutero GmbH, Kastellaun, Germany), which had been filtered previously using a syringe filter (pore size 0.8 μm, mixed cellulose ester membrane). The solution was

placed on a shaker for at least one week before the measurements to ensure equilibrium.

Dynamic light scattering (DLS). DLS data were collected during a temperature scan from 25 to 41 °C at a scattering angle of 90°. At each temperature, 20 measurements were carried out with a duration of 30 s each. The temperature scanning procedure was repeated twice, and the sample was left to equilibrate at 25 °C for 2.5 h between the two scans. For all temperatures, the thermal equilibration time was set to 10 min, before the data collection. The normalized intensity autocorrelation functions, $g_2(\tau,q)$, were analyzed using the REPES algorithm implemented in the Gendist software [140, 207, 208], where the normalized field autocorrelation function, $g_1(\tau,q)$, is assumed as equation 4.9.

Small-angle neutron scattering (SANS). SANS data were collected during a temperature scan from 25 to 50 °C. Before the measurement at each temperature, the thermal equilibration time was set to 3 min.

In the measured temperature range, the total scattering is contributed by the scattering of the aggregates, the MB, and the local density fluctuation and the background scattering. Thus, the SANS data were fitted by the model:

$$I(q) = I_{\mathrm{agg}}(q) + P_{\mathrm{cyl}}(q)S_{\mathrm{HS}}(q) + I_{\mathrm{fluct}}(q) + I_{\mathrm{bk}} \qquad (6.1)$$

where $I_{\mathrm{agg}}(q)$ is the scattering of the aggregates, $P_{\mathrm{cyl}}(q)$ is the cylinder form factor (equation 4.20), $S_{\mathrm{HS}}(q)$ is the Percus-Yevick hard-sphere structure factor (equations 4.24 and 4.25) and $I_{\mathrm{fluct}}(q)$ is the scattering from the local density fluctuation (equation 4.31). I_{bk} is the incoherent background.

$I_{\mathrm{agg}}(q)$ is the Porod term of the Guinier-Porod empirical model (equation 4.29 for $q > q_1$) , which characterizes the inner structure of the aggregates by the Porod exponent α.

The scattering of the individual MBs is modeled by $P_{\mathrm{cyl}}(q)$. Considering the backbone-to-side chain length ratio as well as the SAS data modeling results from previous studies [75, 94, 209], the shape of the P*i*POx$_{100}$-*g*-PEtOx$_{17}$ molecule was expected to be either ellipsoidal or cylindrical. While the trial fits using the ellipsoid form factor returns unphysical structural parameters, $P_{\mathrm{cyl}}(q)$ gives reasonable results. From $P_{\mathrm{cyl}}(q)$, the cross-sectional radius R and the length L of the cylinder are provided, and a Gaussian distribution is considered for both R and L. Thus, their polydispersity is characterized by the standard deviation of the Gaussian distribution. For example, the polydispersity for R is defined as $\sigma_R/R_{\mathrm{mean}}$, where σ_R is the

standard deviation of R and R_{mean} is the mean of the Gaussian distribution. The same applies for the polydispersity of L.

$S_{HS}(q)$ is multiplied with $P_{cyl}(q)$ to account for the correlation between the cylindrical MBs. It gives the hard-sphere radius R_{HS} and the hard-sphere volume fraction η, where the former is an approximation of half the distance between the MBs, and the latter being the volume fraction of the correlated MBs in the sample.

$I_{fluct}(q)$ presumably comes from the dissolved side chains at the periphery parts of the MB, resulting in an electron density gradient at small length scales. It has the form of the Ornstein-Zernike structure factor, with the exponent fixed to be 2. The correlation length ξ of the concentration fluctuation is obtained.

During model fitting, I_{bk} is set to be a free parameter to account for the decreasing overall scattering due to the precipitation of the MBs at high temperatures.

Figure 6.1 demonstrates how each term in equation 6.1 contributes to the total scattering $I(q)$ below and above the cloud point T_{cp} = 40.5 °C (Figure 3.3a), taking the data at 25 °C and 46 °C as examples, respectively.

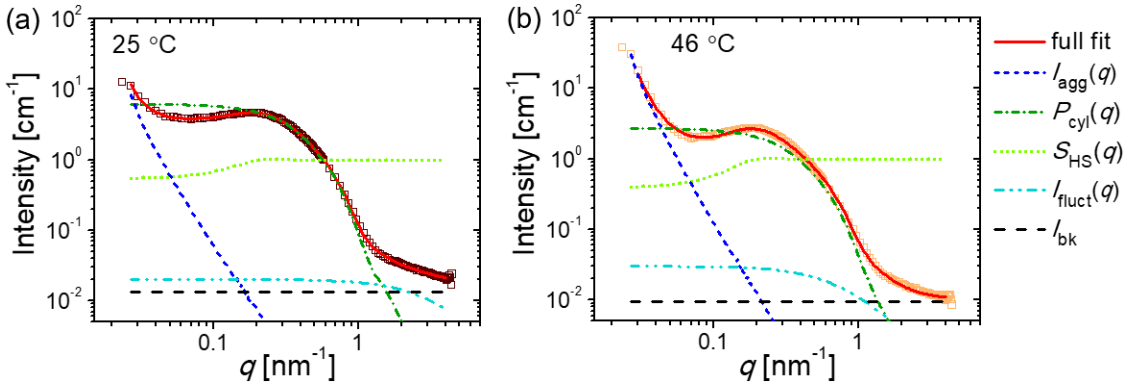

Figure 6.1 Demonstration of model fits to the SANS data of P*i*POx$_{100}$-*g*-PEtOx$_{17}$ solution in D_2O using equation 6.1 at (a) 25 °C and (b) 46 °C, which are below and above T_{cp}, respectively.

The software SasView 4.2.2 was used for model fitting [185], where the q-smearing effects were taken into consideration by using a Gaussian function with standard deviation Δq as a weight function.

6.3 Temperature-resolved diffusional behavior

In order to gain a first knowledge on the thermal responsivity of P*i*POx$_{100}$-*g*-PEtOx$_{17}$, heating scans of DLS measurements were carried out on its aqueous solution at 30 g L^{-1}, from 25 to 41 °C, i.e., from room temperature to just above T_{cp} = 40.5 °C (Figure 3.3). The heating scan was repeated twice, with 2.5 h of waiting time at 25 °C in-between, so that the reproducibility of the thermal behavior is observed.

During the first heating scan, at all measured temperatures, the normalized intensity autocorrelation curves show two decays (Figure 6.2a), a fast mode and a slow mode. This indicates that there are two kinds of diffusing particles having distinctively different sizes in the solution. Considering the hydrodynamic radii R_h distributions of the fast and slow modes (Figure 6.2b), which have maxima at around 8 nm and few micrometers, respectively, the former is attributed to the individual MBs and the latter to the aggregates of the MBs. From the areas under the fast and the slow peaks, it is seen that 80 – 90 % of the scattering intensity stem from the fast mode, and this stays true for all the measured temperatures. Namely, at temperatures below T_{cp}, individual MBs are the majority in the solution, while few of their aggregates coexist with them in the solution. Data collected during the second scan show similar features as in the first scan (Figure 6.2c,d).

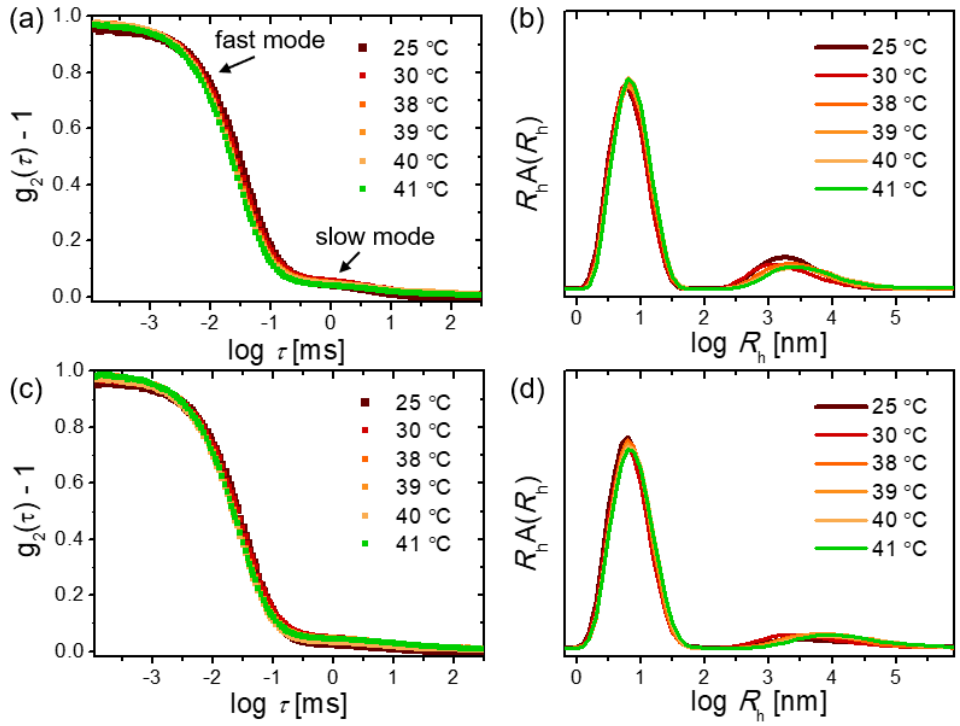

Figure 6.2 Temperature-resolved DLS data collected during two heating scans for P*i*POx$_{100}$-*g*-PEtOx$_{17}$ solution at 30 g L^{-1} in D_2O. (a,c) The normalized intensity autocorrelation. (b,d) Hydrodynamic radii, R_h, distribution. (c) and (d) are from the second scan.

R_h at each measured temperature is obtained as described in chapter 4.1. For the molecularly dissolved MBs, R_h increases from 7.8 ± 0.4 nm to 8.6 ± 0.4 nm (Figure 6.3a) during the first heating scan. During the second scan, R_h of the MBs increases from 8.4 ± 1.1 nm to 9.3 ± 1.0 nm. Comparing R_h values during the two scans, in the second scan R_h is generally about 0.5 nm higher than the one in the first scan, while the uncertainty in the second scan is about two to three times of the one in the first scan. These findings suggest that, the 2.5 h of equilibrium time at 25 °C between the two scans might not be long enough for the system to reverse to its stable state after it is heated up above T_{cp}. The trend of increasing particle size upon heating is actually an unusual observation for LCST MBs [94, 97, 98], since the dehydration of the LCST PEtOx side chains is supposed to result in a shrinkage. The increase of R_h might imply a change in the inner structure of the individually dissolved MBs upon heating towards T_{cp}.

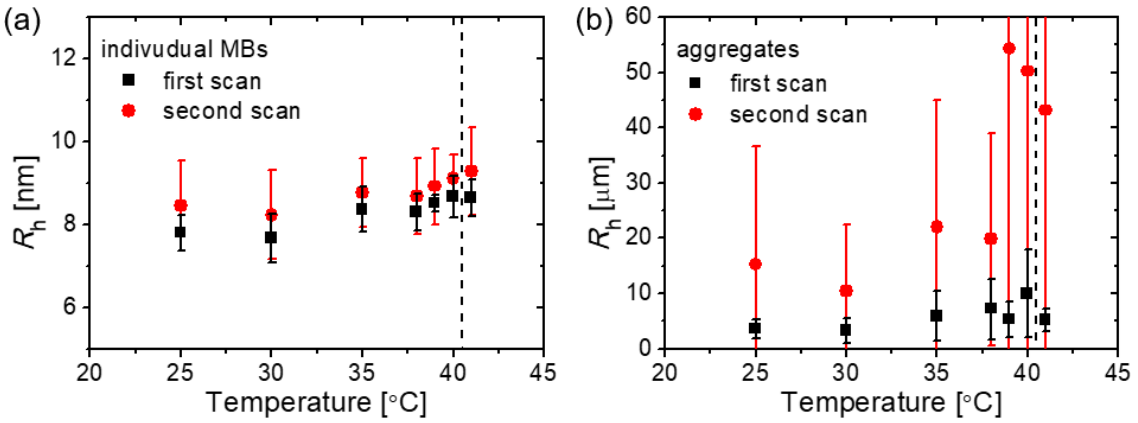

Figure 6.3 R_h as a function of temperature during the first (black squares) and the second (red spheres) heating scan. (a) R_h of individually dissolved MBs (b) R_h of the aggregates. The vertical dashed lines indicate T_{cp} of the solution.

R_h of the aggregates is found to range from several to tens of micrometers (Figure 6.3b) in the two scans, which exceeds the reliable detecting length scale of DLS. Thus, it is concluded that the aggregates have sizes on the micrometer scale, but their R_h cannot be determined precisely from the DLS data.

In summary, a coexistence of the molecularly dissolved MBs and the aggregates is found in the solution in D_2O at 30 g L^{-1}. During the heating scan from 25 to 41 °C, the R_h of the MBs shows a slight increase by 0.8 ± 0.4 nm, and a repeated measurement confirms the increase of R_h upon heating. It is now of interest to characterize the inner structure variation in the same temperature range, in order to explain the increase of R_h.

6.4 Temperature-resolved structural evolution

To disclose the inner structure of the P*i*POx$_{100}$-*g*-PEtOx$_{17}$ molecule and the aggregates, SANS measurements were performed on the identical solution as in the DLS measurements. Ths data during a heating scan from 25 °C up to 50 °C were collected, revealing structural changes from room temperature to far above T_{cp}.

The SANS data are shown in Figure 6.4 along with the model fits, which have several shared features. At q < 0.06 nm^{-1}, the scattering intensity shows a power law relation with q, namely $I(q) \sim q^{\alpha}$, which indicates the presence of large fractal objects. This is attributed to the scattering of the aggregates in the solution. The scattering from the aggregates is modeled by

the Porod term, where the power law exponent, α, reveals the structural compactness of the aggregates. Comparing data below and above T_{cp}, α is apparently larger at temperatures above T_{cp}, implying more compact aggregates at high temperatures.

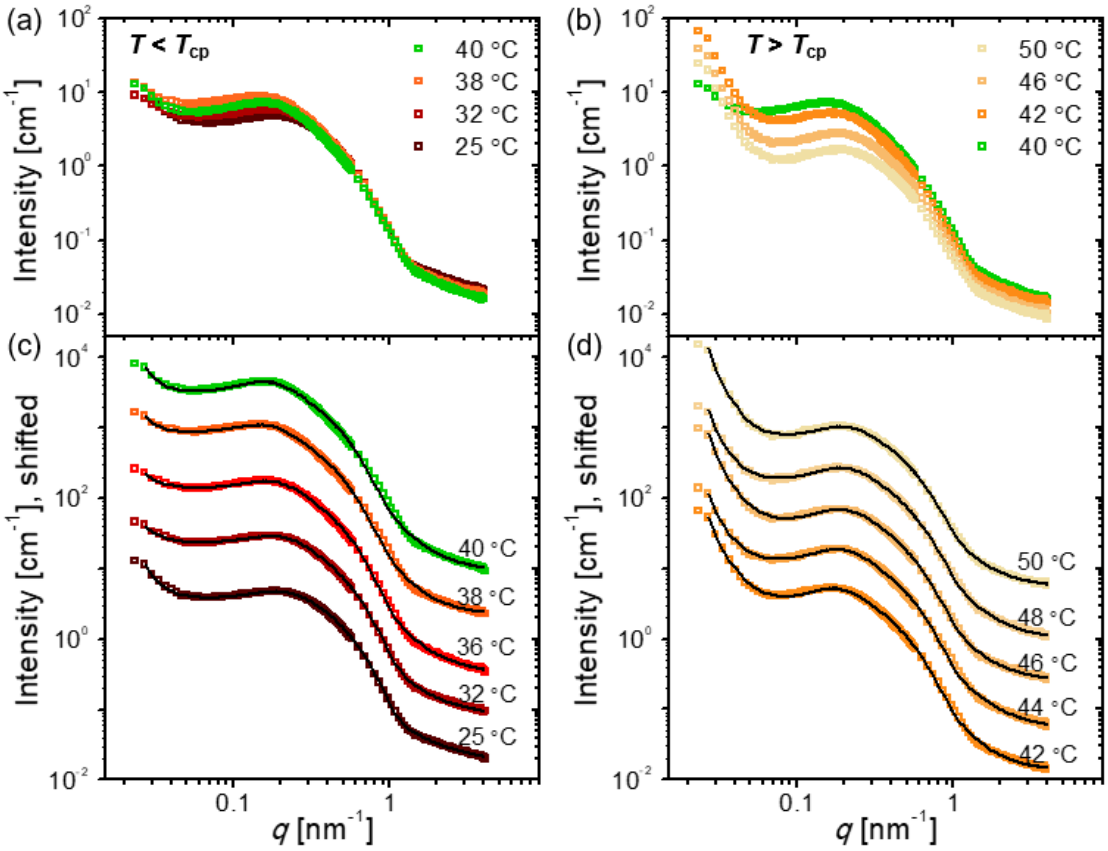

Figure 6.4 SANS data (symbols) of the P*i*POx$_{100}$-*g*-PEtOx$_{17}$ solution in D_2O at 30 g L^{-1} at the indicated temperatures. (a) and (b) are the data below and above T_{cp}, respectively, and only data from selected temperatures are shown, to avoid the unclarity due to overlapping data. Data at all temperatures are shown in (c) and (d) along with the model fits (solid lines), and the intensity is shifted by a factor of 5 with respect to each other.

In the mid-q region (0.06 – 1 nm^{-1}), $I(q)$ shows a broad peak at $q \approx 0.2$ nm^{-1} followed by a monotonic decay. As this q range fits to the approximate length scale of the MB, it is supposedly contributed by the individually dissolved MBs in the solution, and the broad peak is due to the spatial correlation between them. In the range of 0.06 – 0.3 nm^{-1}, $I(q)$ increases upon heating from 25 to 38 °C, and decreases again when heated up to 40 °C (Figure 6.4a). In the range of 0.6 – 1 nm^{-1}, on the other hand, SANS curves hardly change with increasing temperature from 25 to 40 °C. The MB is modeled to be a rigid cylinder having polydisperse cross-sectional

radius R and length L. The above-mentioned observations indicate that increasing temperature mainly influences the large length scale, i.e., the cylinder length L, while the small length scale, i.e., the cylinder radius R, is unaffected. The maximum at $q \approx 0.2$ nm^{-1} originates from the spatial correlation between the MBs, and it slightly shifts towards lower q upon heating to 40 °C, implying that the average distance between MBs becomes larger. The correlation is modeled by the Percus-Yevick hard-sphere structure factor $S_{HS}(q)$, giving the hard-sphere radius R_{HS}, and the hard-sphere volume fraction η. (Above 40 °C, due to the overall decrease of the scattering intensity, it is difficult to make comments on the changes of SANS data during heating from the SANS curves.)

In the high-q region (1 – 5 nm^{-1}), the intensity shows a shallow decay with q. This is attributed to the presence of concentration fluctuations at small length scales, which is presumably from the dissolved side chains. Upon variation of temperature, it stays rather unchanged. The Ornstein-Zernike structure factor is used to model this scattering contribution, giving the characteristic correlation length ξ of the local density fluctuation.

Despite of the wide detecting temperature range, crossing the phase transition temperature, SANS data contain all the three above-mentioned contributions. Therefore, the same fitting model (equation 6.1) is used for data at all temperatures, and nice fits were obtained (Figure 6.4c,d, solid lines).

Above 40 °C, i.e., right above $T_{cp,}$ clearly visible precipitates appear in the solution, resulting in a steadily decrease of the overall scattering intensity upon heating (Figure 6.4b). From 40 to 50 °C, the incoherent scattering background, I_{bk}, decreases from 0.0139 cm^{-1} to 0.0078 cm^{-1}, implying that about 44 % of the MBs precipitate. The precipitates again dissolve, after few weeks of storage at room temperature, even without shaking the solution.

In the following, the dependence of the structural parameters on temperature is discussed. Scattering from large-scale inhomogeneities or aggregates is observed in the entire temperature range. The inner structure of the aggregates is evaluated by the Porod exponent α. It is around 2.7 at 25 °C, and slightly decreases to 2.5 upon heating to 36 °C (Figure 6.5a). At 38 °C, α increases abruptly to 3.1 and then fluctuates around 3.0. Above T_{cp}, α steadily increases until it reaches 3.5 at 50 °C. Overall, α shows an increasing trend, meaning the aggregate becomes more compact upon heating. Judging by the α value, the aggregates have a loose inner structure at room temperature, and they transform into compact ones with rough surface at high temperatures. The structural evolution of the aggregates is schematically demonstrated in Figure 6.6. The scaling factor of the Porod term, I_D, shows a significant decrease above T_{cp}

(Figure 6.5b), which is presumably due to the precipitation.

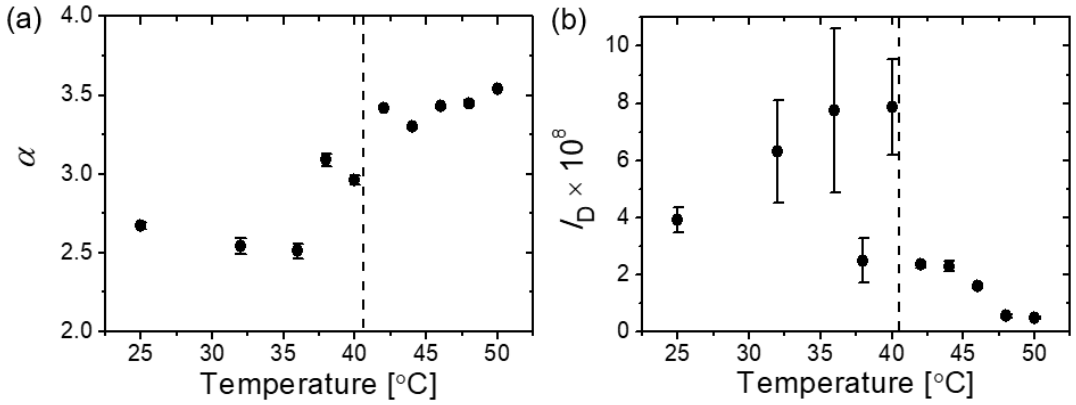

Figure 6.5 Structural parameters from the Porod term for the aggregate scattering $I_{agg}(q)$ from 25 to 50 °C, obtained by modeling the SANS data of P*i*POx$_{100}$-*g*-PEtOx$_{17}$ solution at 30 g L^{-1} in D_2O. (a) Porod exponent α. (b) Scaling factor I_D. The vertical dashed lines indicate T_{cp} of the solution.

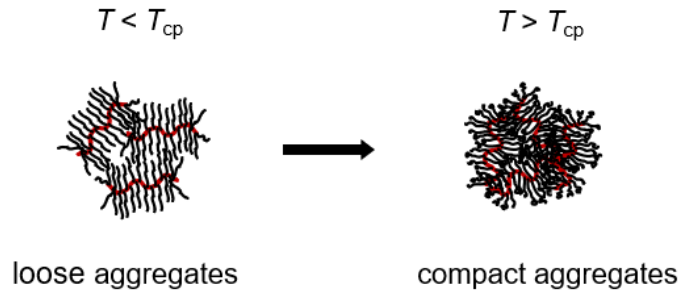

Figure 6.6 Schematic representation of the structural changes of the aggregates in the P*i*POx$_{100}$-*g*-PEtOx$_{17}$ aqueous solution at 30 g L^{-1}, from below to above T_{cp}. The arrow indicates the heating process.

The individually dissolved MBs are modeled by the cylinder form factor. At 25 °C, *R* is found to be 2.8 nm, and *L* is 12.5 nm (Figure 6.7a). The polydispersity of *R* and *L* are 0.25 and 0.14, respectively, and the high polydispersity values imply that the shape of the MBs is between a rigid cylinder and a prolate ellipsoid. While *R* stays nearly unchanged, *L* shows a clear dependence on temperature. From 25 to 38 °C, *L* increases to 21.0 nm, and then decreases above 38 °C until it becomes 12.4 nm at 50 °C. The increasing trend between 25 and 38 °C suggests that the backbone is straightened, which explains the increasing R_h found by DLS (Figure 6.3a). The backbone extension is thought to be related to the dehydration of the PEtOx$_{17}$

side chains, which shrink upon heating. The shrinkage of the side chains leads to an increasing density around the backbone, and thus the backbone is straightened to account for the spatial limitation. Above 38 °C, the decrease of *L* is supposed to be an overall collapse of the MBs due to the continuously increased hydrophobicity of $PEtOx_{17}$. It should be noted that, although the changes in *L* mainly originates in the LCST property of the $PEtOx_{17}$ side chains, *R* does not show variation with temperature accordingly. This is attributed to the high grafting density of the side chains, making the change in the lateral direction too small to be detected.

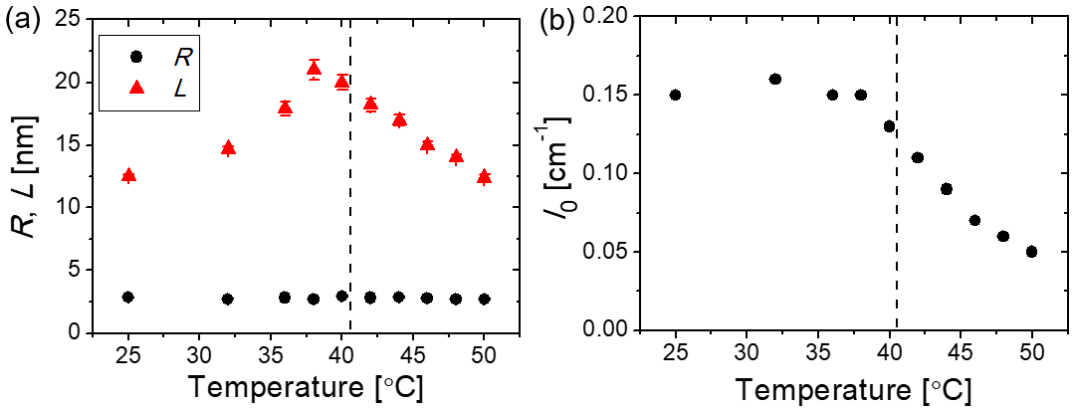

Figure 6.7 Structural parameters from the cylinder form factor $P_{cyl}(q)$ from 25 to 50 °C, obtained by modeling the SANS data of P*i*POx_{100}-*g*-$PEtOx_{17}$ solution at 30 g L^{-1} in D_2O. (a) The cylinder radius *R* (black circles) and the cylinder length *L* (red triangles). (b) Scaling factor I_0. The vertical dashed lines indicate T_{cp} of the solution.

The two-step variation in shape is presumably linked to the architectural parameters of the MB. As discussed in chapter 2.4, regarding the thermoresponsive behavior of MBs with LCST side chains, in case the backbone is much longer than the side chains, the increasing hydrophobicity upon heating leads to a cylindrical-to-globule shape transition due to the coiling of the backbone. On the other hand, in case of similar backbone and side chain length, coiling of the backbone is unlikely, thus the hydrophobic side chains lead to a shrinkage of the overall MB size. In the present case of P*i*POx_{100}-*g*-$PEtOx_{17}$, the backbone length is neither very long nor close to its side chain length. Therefore, the continuous dehydration of the PEtOx side chains firstly leads to a straightening of the MB due to the spatial limitation in the central part of the MB, before the overall collapse above T_{cp}.

The scaling factor of the cylinder form factor, I_0, stays unchanged between 25 to 38 °C, and continuously decreases above 38 °C (Figure 6.7b). The decreasing I_0 is related to the

decreasing number of individually dissolved MBs, which could be a result from the aggregation of these MBs, or due to the precipitation at high temperatures.

The spatial correlation between the MBs is modeled by the Percus-Yevick hard-sphere structure factor. R_{HS}, which can be seen as half the average distance between the MBs, is found to be 11.9 nm at 25 °C (Figure 6.8a, black circles, left scale), and increases with increasing temperature up to 40 °C. Further heating above 40 °C, R_{HS} decreases. The variation of R_{HS} is supposed to correspond to the variation of the size of MB in its longitudinal direction, i.e., L from the form factor (Figure 6.7a, red triangles). Considering the spatial correlation, one might ask if the cylindrical MBs are closely packed. This could be answered by comparing the value of $2 \times R_{HS}$ with L, to see if the MBs are aligned due to the limited space or even overlapping. The values of $(2R_{HS} - L)/L$ are plotted in Figure 6.8b against temperature, providing hints to the distance between neighboring MBs relative to their own size. It is found that, at all temperatures, $(2R_{HS} - L)/L$ is always above zero, i.e., the MBs are well separated from each other and their correlation is weak. It is 90 % at 25 °C, and decreases to 38 % at 38 °C, indicating the MBs become closer upon heating towards T_{cp}, probably due to the increasing hydrophobicity. Above 38 °C, $(2R_{HS} - L)/L$ continuously increases until it reaches 105 % at 50 °C, meaning the MBs become far apart from each other. This is presumably due to the precipitation of MBs, leading to a decreasing number of MBs in the solution. η is found to be small (Figure 6.8a, blue triangles, right scale), i.e., between 0.08 and 0.13, which is in line with the weak spatial correlation described above. It shows a slight increase by around 0.05 upon heating from 25 °C to T_{cp}, implying an enhancement of the correlation strength. Above T_{cp}, it decreases by around 0.02 due to the decreasing number of dissolved MBs.

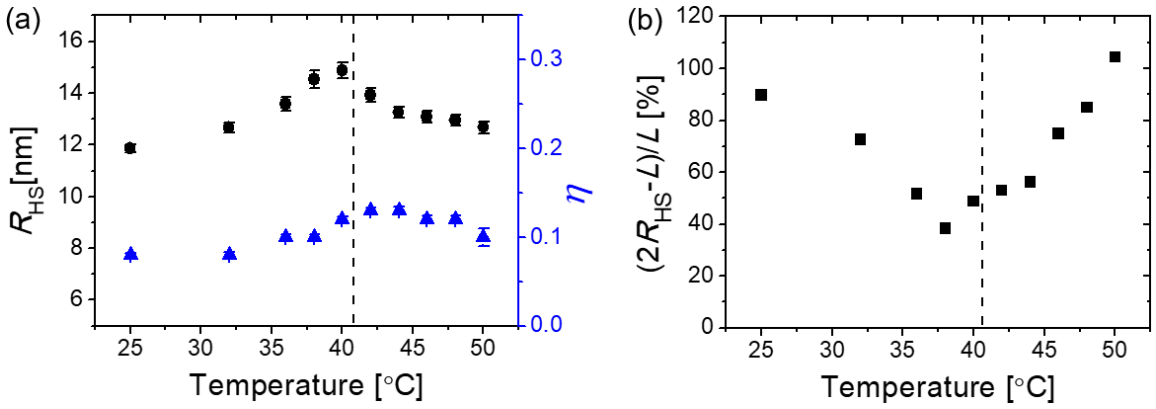

Figure 6.8 (a) Structural parameters from the Percus-Yevick hard-sphere structure factor $S_{HS}(q)$ from 25 to 50 °C, obtained by modeling the SANS data of P*i*POx$_{100}$-*g*-PEtOx$_{17}$

solution at 30 g L^{-1} in D_2O. The hard-sphere radius R_{HS} (black circles, left scale) and the hard-sphere volume fraction η (blue triangles, right scale). (b) Values of $(2R_{HS} - L)/L$, where L is the cylinder length from Figure 6.7a. The vertical dashed line indicates T_{cp} of the solution.

The scattering at small length scales from the side chains is modeled by the Ornstein-Zernike structure factor. ξ is 0.3 nm at 25 °C and sees an increase upon heating towards T_{cp} to reach 1.6 nm (Figure 6.9a), where a sharp upturn appears at 38 °C. The scaling factor I_{oz} also shows such sharp increase starting at 38 °C (Figure 6.9b). The increasing trend of both ξ and I_{oz} is the same behavior as the LCST linear polymers in aqueous solutions, meaning that the local chain conformation becomes more compact due to the increasing hydrophobicity. Compared to linear chains, the ξ values in MB solution are much smaller than the ones from linear polymer systems [210, 211]. This is attributed to the densely grafted structure, and thus the high chain density. Above T_{cp}, ξ shows a shallow increase along with large uncertainties, and I_{oz} scatters without clear trend. These might be due to both the effects from the collapsed side chains and the precipitation of the MBs, thus the scattered data points.

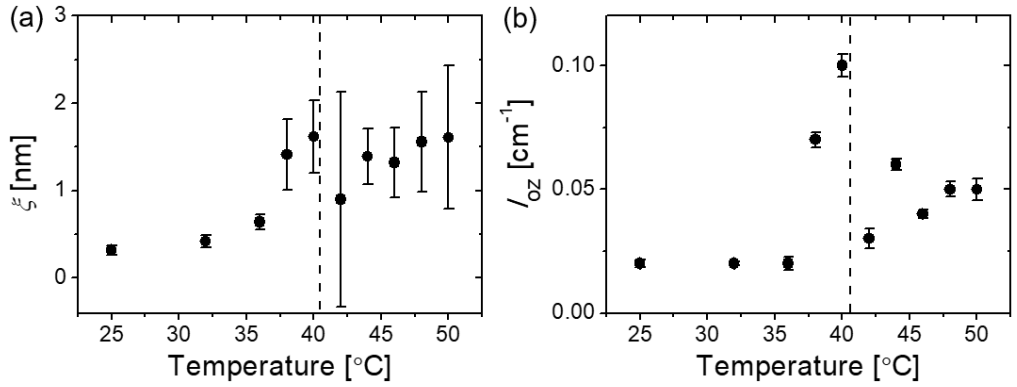

Figure 6.9 Structural parameters from the density fluctuation $I_{fluct}(q)$, using the modified Ornstein-Zernike structure factor, from 25 to 50 °C, obtained by modeling the SANS data of P*i*POx_{100}-*g*-$PEtOx_{17}$ solution at 30 g L^{-1} in D_2O. (a) Correlation length ξ. (b) Scaling factor I_{oz}. The vertical dashed lines indicate T_{cp} of the solution.

Based on the SANS analysis, a schematic representation can be drawn, regarding the structural evolution of the P*i*POx_{100}-*g*-$PEtOx_{17}$ molecules in an aqueous solution (Figure 6.10). Upon heating, the MBs firstly stretch and then overall collapse above T_{cp}, which is due to the dehydration of the side chains and the continuously increasing hydrophobicity.

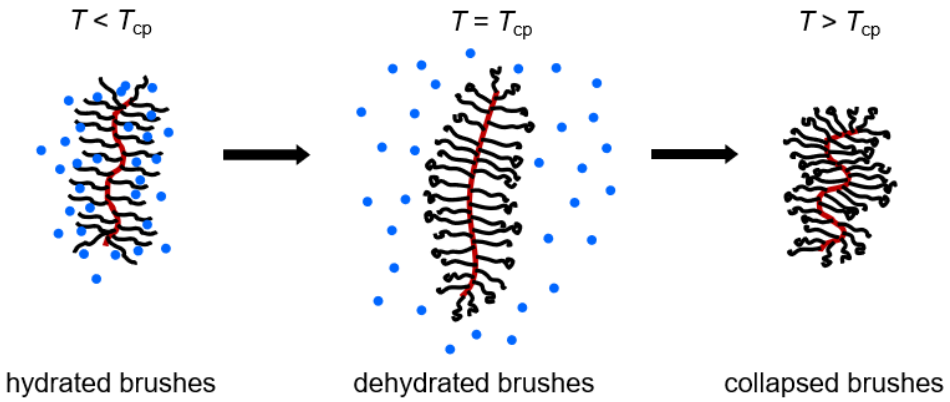

Figure 6.10 Schematic representation of the structural variation of the P*i*POx$_{100}$-*g*-PEtOx$_{17}$ molecules at 30 g L^{-1} in aqueous solutions, from below to above T_{cp}. The arrows indicate the heating process, and the blue circles are the water molecules.

6.5 Conclusion

The LCST behavior of the MB P*i*POx$_{100}$-*g*-PEtOx$_{17}$ at 30 g L^{-1} in D_2O is investigated, and the temperature-dependent inner structure is resolved, from room temperature up to 50 °C, i.e., 10 °C above its T_{cp} = 40.5 °C. The coexistence of the large aggregates and the individually dissolved MBs is found in the full temperature range. Namely, not all of the MBs become parts of the aggregates above T_{cp}. Due to the fact that the length ratio between the backbone and the side chain is neither very large nor very small, the MBs show an extension upon heating towards T_{cp} before it shrinks above T_{cp}, instead of the continuous shrinkage that is generally observed for MBs with LCST side chains.

7. Structural investigation on MBs with LCST copolymer side chains

As a following study of chapter 6, the thermoresponsive behavior of two MBs having LCST copolymer side chains is investigated in this chapter. The main results in this chapter were previously published in J.-J. Kang et al., *Macromolecules* **2020**, *53*, 4068-4081 [212].

7.1 Introduction

As discussed in chapter 2.4.1, when the MB has thermoresponsive copolymer side chains, different monomer sequence is expected to result in different thermoresponsive behavior. In the present work, two MBs having PPO-*co*-PEO side chains are studied, where both poly(propylene oxide) (PPO) and poly(ethylene oxide) (PEO) are LCST-type polymers. Their T_{cp} are, however, vastly different. It is only 8 °C for PPO, while it is above 100 °C for PEO. Thus, at ambient temperature, PPO is insoluble in water, while PEO is completely soluble. The two MBs differ in the side chain architecture, where one has PPO-*b*-PEO side chains (called P*b*E in the following content) and the other has P(PO-*ran*-EO) side chains (called P*r*E). *Cryo*-electron transmission (*cryo*-EM) and small-angle neutron scattering (SANS) were performed on their dilute aqueous solutions, to gain structural information about the isolated MBs. Further, DLS and SANS measurements were performed on their semi-dilute solutions during a temperature scan, so that the differences in the LCST behavior are characterized by resolving the inner structure evolution in a wide temperature range.

7.2 Experimental details

Sample preparation. The sample solutions for *cryo*-EM images are P*b*E and P*r*E solutions in deionized H_2O at 2.5 g L^{-1}. For DLS measurements, the samples are P*b*E and P*r*E solutions in D_2O at 20 g L^{-1}. For SANS measurements, the samples are solutions in D_2O at 5 g L^{-1} or 20 g L^{-1}. For preparing the solutions, the dry polymer powder was dissolved in the solvent, which had been filtered previously using a syringe filter (pore size 0.8 ㎜, mixed cellulose ester

membrane). The solutions were placed on a shaker for at least one week before the measurements to ensure equilibrium.

Dynamic light scattering (DLS). DLS data were collected during a heating scan between 25 and 60 °C for the P*b*E solution, and between 25 to 38 °C for the P*r*E solution. Above the respective highest temperature, the solutions become so turbid that the recording of scattering intensity is impossible. The scattering angle was fixed at 90°. At each temperature, 20 measurements were performed, and the duration for each was 30 s. 10 min of waiting time was set for thermal equilibrium before data collection at each temperature. The normalized intensity autocorrelation functions, $g_2(\tau,q)$, were analyzed using the REPES algorithm implemented in the Gendist software [140, 207, 208], where the normalized field autocorrelation function, $g_1(\tau,q)$, is assumed as equation 4.9.

Small-angle neutron scattering (SANS). SANS data were collected for dilute solutions of P*b*E and P*r*E at 5 g L^{-1}, at 25 °C. Also, data were collected during a heating scan for their semi-dilute solutions at 20 g L^{-1}, where the temperature range is 25 – 66 °C for P*b*E, and 25 – 46 °C for P*r*E. At each measured temperature, a thermal equilibration time of 3 min was set.

For data collected below and above the cloud point T_{cp} of the solution, the fitting model contains different contributions respectively. Below T_{cp}, the scattering mainly comes from the individually dissolved MBs, while above T_{cp}, it is the scattering of their aggregates. Besides, slightly different models are used for P*b*E and P*r*E to account for the different features in their SANS data, revealing the structural details in the two systems.

The fitting model for P*b*E solution at 5 g L^{-1} (25 °C) is:

$$I(q) = P_{cs}(q)S_{HS}(q) + I_{bk} \tag{7.1}$$

where $P_{cs}(q)$ is the core-shell ellipsoid form factor (equations 4.18 and 4.19) and $S_{HS}(q)$ is the Percus-Yevick hard-sphere structure factor (equations 4.24 and 4.25). I_{bk} is the incoherent background.

$P_{cs}(q)$ is chosen to model the P*b*E MB, because of its intrinsic core-shell structure as a result from the block copolymer side chains. More importantly, the high grafting density of the side chains supposedly leads to a distinct difference in the polymer-water composition between the central part and the outer part of the MB. It gives the polar radius R_p and the equatorial radius R_e in the core, as well as the polar thickness T_p and the equatorial thickness T_e in the shell.

The SLDs in the core (ρ_c) and shell (ρ_s) parts are also free variables during fitting, while the SLD of the solvent D_2O was fixed at 6.33×10^{-6} Å^{-2}, considering its mass density 1.1 g/cm^3. The fitting results of ρ_c and ρ_s are compared with the SLDs of pure PPO and PEO, 0.34×10^{-6} Å^{-2} and 0.64×10^{-6} Å^{-2} [213], respectively, thus providing an estimate of the D_2O content in the core and the shell parts of the ellipsoid. $S_{HS}(q)$ is used to describe the correlation between MBs. It gives the hard-sphere radius R_{HS}, which is half the average distance between the correlated MBs, and the hard-sphere volume fraction η, namely the volume fraction of the correlated MBs.

For P*b*E solution at 20 g L^{-1}, data between 25 and 58 °C, i.e., below T_{cp}, were also fitted by equation 7.1. Figure 7.1a shows the contribution by each term in equation 7.1 to the SANS data for P*b*E solution at 20 g L^{-1} below T_{cp}, demonstrated by the data at 25 °C.

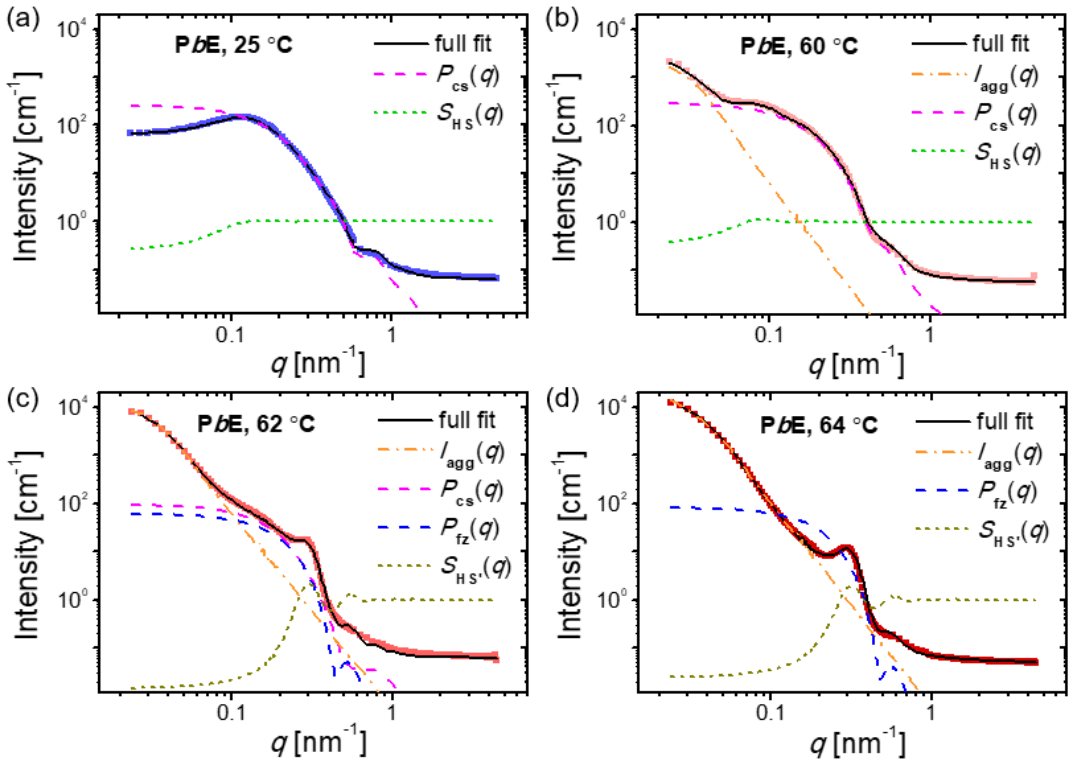

Figure 7.1 Demonstration of model fits to the SANS data of P*b*E at 20 g L^{-1} (symbols). (a) 25 °C, using equation 7.1. (b) 60 °C, using equation 7.2. (c) 62 °C, using equation 7.3. (d) 64 °C, using equation 7.4.

For SANS data of P*b*E solution (20 g L^{-1}) at T_{cp} = 60 °C, the fitting model include contribution from the scattering of the aggregates, which are composed of several MBs. Meanwhile, the scattering of the individually dissolved MBs is still present between 60 and 62 °C, coexisting with the large aggregates. Above 64 °C, all of the MBs become a part of the

aggregates, so no scattering of individual MBs is observed in SANS data. Thus, between 60 and 64 °C, the fitting model is modified to accordingly include the scattering contributions as described. At 60 °C, the model includes the scattering of the aggregates, $I_{agg}(q)$, and the the scattering of individual MBs as at lower temperatures. The fitting equation reads:

$$I(q) = I_{agg}(q) + P_{cs}(q)S_{HS}(q) + I_{bk} \tag{7.2}$$

At 62 °C, the MBs composing the aggregates are closely packed and this is modeled by the fuzzy sphere form factor $P_{fz}(q)$ (equation 4.17), which is combined with another hard-sphere structure factor $S_{HS'}(q)$. Considering the aggregates with the presence of the individual MBs, the fitting equation is:

$$I(q) = I_{agg}(q) + P_{fz}(q)S_{HS'}(q) + P_{cs}(q)S_{HS}(q) + I_{bk} \tag{7.3}$$

Above 64 °C, contribution from individual MBs no longer appear in SANS data, so the fitting equation is:

$$I(q) = I_{agg}(q) + P_{fz}(q)S_{HS'}(q) + I_{bk} \tag{7.4}$$

For I_{agg}(q), the empirical Guinier-Porod model (equation 4.29) is used. The Guinier term gives the radius of gyration of the aggregate, $R_{g,agg}$, and the shape factor, s. The Porod term gives the Porod exponent α, which characterizes the surface roughness of the aggregates. $P_{fz}(q)$ is essentially a sphere having a density gradient at the surface (see Figure 4.6), giving the fuzzy sphere radius R_{fz} and the fuzziness f. Figure 7.1b-d clearly show the contribution from each term in the fitting models at 60 °C, 62 °C and above 64 °C for P*b*E solution, where equation 7.2, equation 7.3 and equation 7.4 are used, respectively.

The fitting model for P*r*E solution at 5 g L^{-1} (25 °C) is:

$$I(q) = P_{cs}(q) + I_{fluct} + I_{bk} \tag{7.5}$$

$P_{cs}(q)$ is again used to model the MBs, considering a polymer-rich central part and a water-rich outer part. $I_{fluct}(q)$ is the scattering from the local concentration fluctuations (equation 4.31). It is presumably the scattering of the side chains. This is modeled by the modified Ornstein-Zernike equation, giving the correlation length ξ and the exponent m.

For P*r*E solution at 20 g L^{-1}, the fitting model between 25 and 36 °C, i.e., below T_{cp}, is:

$$I(q) = P_{cs}(q)S_{HS}(q) + I_{fluct} + I_{bk} \quad (7.6)$$

where $S_{HS}(q)$ describes the correlation between the MBs. Figure 7.2a shows the contribution by each term in equation 7.6 to the SANS data for P*r*E solution at 20 g L^{-1} below T_{cp}, demonstrated by the data at 25 °C.

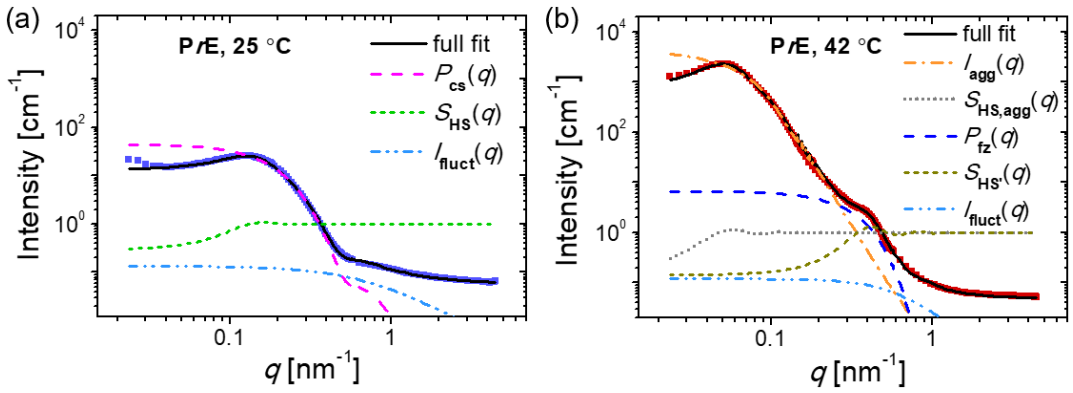

Figure 7.2 Demonstration of model fits to the SANS data of P*r*E at 20 g L^{-1} (symbols). (a) 25 °C, using equation 7.6. (b) 42 °C, using equation 7.7.

For SANS data of P*r*E solution (20 g L^{-1}) above T_{cp} = 38 °C, the fitting model is:

$$I(q) = I_{agg}(q)S_{HS,agg}(q) + P_{fz}(q)S_{HS'}(q) + I_{fluct}(q) + I_{bk} \quad (7.7)$$

The hard-sphere structure factor $S_{HS,agg}(q)$ is multiplied to the aggregate scattering $I_{agg}(q)$ to account for the spatial correlation between the aggregates. This gives the hard-sphere radius, $R_{HS,agg}$, and the hard-sphere volume fraction, η_{agg}. Figure 7.2b shows the contribution by each term in equation 7.7 to the SANS data for P*r*E solution above T_{cp}, demonstrated by the data at 42 °C.

The software SasView 4.2.2 was used for model fitting [185], where the q-smearing effects were taken into consideration by using a Gaussian function with standard deviation Dq as a weight function.

7.3 *Cryo*-EM images

The c*ryo*-EM images of P*b*E and P*r*E solutions at 2.5 g L^{-1} in H_2O were taken, where the samples were prepared at 25 °C. It reveals the overall shape and size of the two kinds of MBs

in real space under ambient temperature.

Images of P*b*E and P*r*E are shown in Figure 7.3a and Figure 7.3b, respectively, where the individual MBs are clearly recognized: the dark lines are the polymeric backbones, which is surrounded by the greyish region of side chains. In general, a shape of elongated ellipsoid is found for both kinds of MBs, while P*r*E appears to be more anisotropic than P*b*E. The different aspect ratio, i.e., the ratio between the dimensions along the longitudinal and the perpendicular direction, of the ellipsoidal MBs is explained by the degrees of polymerization of the backbone and the side chains (Table 7.1). For P*b*E, N_{sc} is almost triple of N_{bk}; whereas for P*r*E, N_{bk} and N_{sc} are comparable. Thus, a lower aspect ratio is observed for P*b*E, compared to P*r*E.

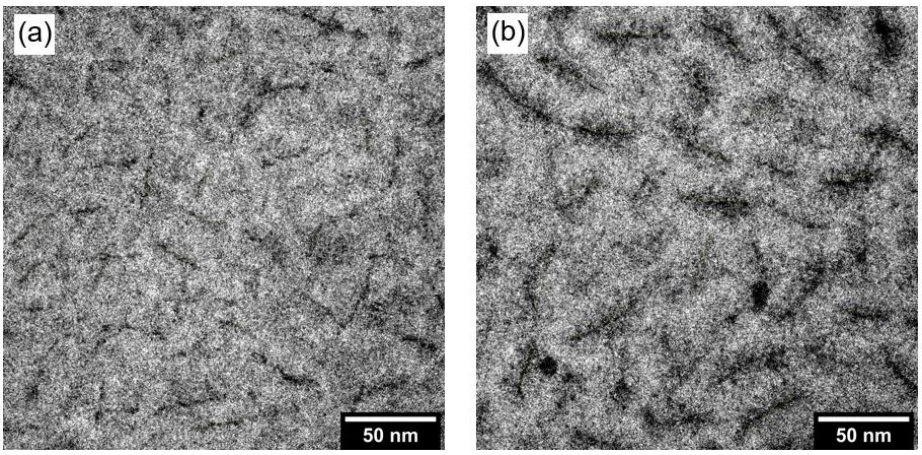

Figure 7.3 *Cryo*-EM images of (a) P*b*E and (b) P*r*E solutions at 2.5 g L^{-1} in H_2O.

Table 7.1 The degrees of polymerization and the estimated lengths for the backbone and the side chains of P*b*E and P*r*E molecules.

Sample	N_{bk}[(a)]	N_{sc}[(b)]	L_{bk}[(c)] **[nm]**	L_{sc}[(d)] **[nm]**
P*b*E	88	253	22.2	91.2
P*r*E	143	157	36.0	56.6

[(a)]Degree of polymerization of the backbone. [(b)]Degree of polymerization of the side chain. [(c)]Estimate of the fully stretched backbone length. [(d)]Estimate of the fully stretched side chain length.

N_{bk} and N_{sc} further allow an estimate of the backbone lengths and the side chain length by multiplying the degree of polymerization with the corresponding monomer length, considering the C-C bond and the C-O bond lengths as well as the bond angle [197]. The backbone length

with a stretched conformation, L_{bk}, is thus obtained (Table 7.1), which is 22.2 nm for P*b*E and 36.0 nm for P*r*E. These values are compared with the lengths of the backbones on the image, which are labeled by numbers in Figure 7.4, and the corresponding lengths are given in Table 7.2. For P*b*E, the length range is 15.6 – 20.1 nm, and for P*r*E it is 17.0 – 36.5 nm. Considering that the *cryo*-EM image is a 2D projection of the MBs embedded in the thin frozen film, where MBs are oriented in all directions in the 3D space, only the maximum values in Table 7.2 should be taken as the full length of the backbones. Thus, it is reasonable to compare L_{bk} values in Table 7.1 with the maximum values in Table 7.2, respectively for P*b*E and P*r*E, which provides the conformational information of the backbones. It turns out that the maximum values for both samples are found to be close to the corresponding L_{bk}, implying a stretched chain conformation of the backbones.

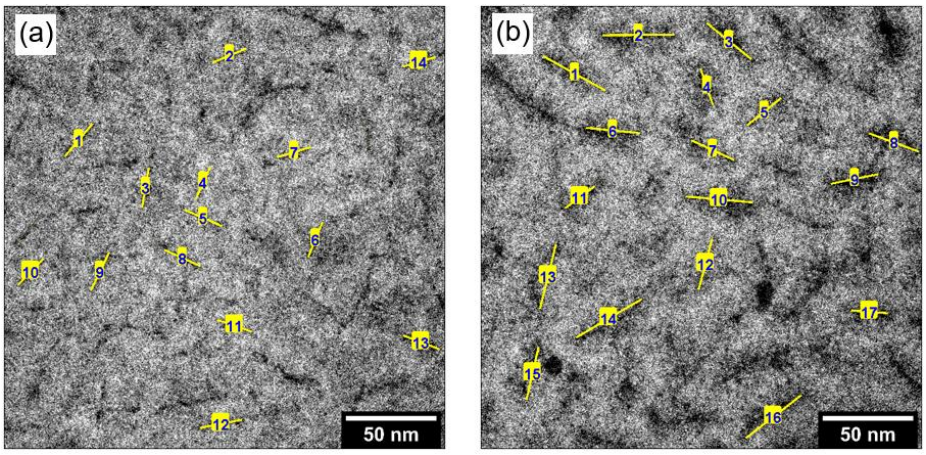

Figure 7.4 The identical c*ryo*-EM images in Figure 7.1 of (a) P*b*E and (b) P*r*E, where selective dark lines in the image are marked by the yellowish lines along with a labeled number for each. The corresponding length for the yellowish lines in real space are given in Table 7.2

Table 7.2 Length of the labeled yellowish lines in Figure 7.4.

Figure 7.4a (P*b*E)		**Figure 7.4b (P*r*E)**	
Labeled #	**Length [nm]**	**Labeled #**	**Length [nm]**
1	20.1	1	34.2
2	17.3	2	34.3
3	19.0	3	27.4
4	16.4	4	17.8

5	19.1	5	20.4
6	17.5	6	25.9
7	16.6	7	22.1
8	18.5	8	25.0
9	19.8	9	22.7
10	16.9	10	32.2
11	16.8	11	17.0
12	20.1	12	24.7
13	18.0	13	31.8
14	15.6	14	36.5
		15	25.5
		16	33.3
		17	17.2

In summary, from the *cryo*-EM images of P*b*E and P*r*E dilute aqueous solutions, it is found that both of the MBs feature an overall shape of prolate ellipsoid, and the backbone has a rather straight conformation. Among the two MBs, P*b*E shows a smaller aspect ratio due to the fact that its side chain length is much longer than the backbone length.

7.4 Structure in dilute and semi-dilute solution

To investigate the inner structure of P*b*E and P*r*E at ambient temperature, SANS measurements were performed on their solutions at 5 g L^{-1} and 20 g L^{-1} in D_2O at 25 °C. The data are shown in Figure 7.5a and Figure 7.5b for P*b*E and P*r*E, respectively.

For P*b*E, the curves at the two concentrations feature a monotonic decay and an additional fringe at $q \approx 0.7$ nm^{-1}. For P*r*E, the two curves feature a monotonic decay and a scattering tail at $q > 0.1$ nm^{-1}. For both kinds of the MBs, at 5 g L^{-1}, the decay of the scattering intensity appears at lower q (0.1 – 0.5 nm^{-1}), compared to the one at 20 g L^{-1} (0.2 – 0.9 nm^{-1}), implying a lager particle size at 5 g L^{-1}. Also, the data at 20 g L^{-1} additionally show a broad maximum at $q \approx 0.15$ nm^{-1}, which is the correlation peak between the MBs. On the other hand, the data at 5 g L^{-1} do not have such broad peak, indicating that the inter-particle correlation is either not present or very weak.

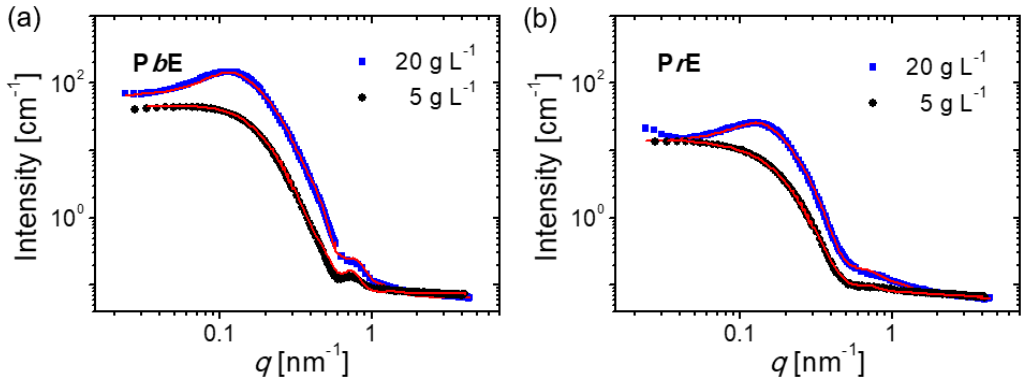

Figure 7.5 SANS data of (a) P*b*E and (b) P*r*E solutions at 5 (black circles) and 20 g L^{-1} (blue squares) in D_2O, shown together with the corresponding model fits (solid lines).

The scattering of the MBs is modeled by the core-shell ellipsoid form factor $P_{cs}(q)$. It gives the core radius in the polar (R_p) and the equatorial (R_e) directions, the shell thickness in the polar (T_p) and the equatorial (T_e) directions, and the SLDs in the core (ρ_c) and the shell (ρ_s) region. At 5 g L^{-1}, the presence of the inter-particle correlation is found only for P*b*E, and not for P*r*E. At 20 g L^{-1}, both kinds of the MBs feature inter-particle correlation, which is described by the hard-sphere structure factor $S_{HS}(q)$. Additionally, for P*r*E, the scattering contribution from the chain scattering is included in the fitting model. This is described by the modified Ornstein-Zernike equation, giving the correlation length ξ of the local density fluctuations and the exponent m. With the described model, nice fits were obtained (Figure 7.5, solid lines).

The resulting structural parameters from $P_{cs}(q)$ for P*b*E solution at 5 g L^{-1} and 20 g L^{-1} are shown in Figure 7.6, for a comparison between the dilute and the semi-dilute solutions. At 5 g L^{-1}, The radii in the core part are R_p = 6.4 nm and R_e = 8.6 nm, and the shell thicknesses, i.e., T_p and T_e, are both 8.7 nm (Figure 7.6a, black closed circles), which together give a nearly spherical shape. (Here, one might be confused by the SANS results when recalling the ellipsoidal shape observed under *cryo*-EM (Figure 7.1a). It is supposed that, it is the backbone region, with a high electron density, that is observed in *cryo*-EM, while SANS reflects the structure of the whole MB.) At 20 g L^{-1}, R_p = 7.4 nm and R_e = 8.2 nm (Figure 7.6a, blue hollow circles), which are similar to the values at 5 g L^{-1}. Thus, the dimensions of the core part hardly change with varying concentration. Meanwhile, T_p (16.8 nm) is much larger than T_e (4.3 nm), meaning the shell is much thicker in the polar direction than in the equatorial direction. Namely, upon increasing concentration, the shell thickness grows in the polar direction, while it shrinks in the equatorial direction. Thus, the dimensions of the shell part show a significant dependence

on the solution concentration. The value of ρ_c yields 3 vol% of D_2O content in the core, and the ρ_s value yields 85 vol% of D_2O in the shell (Figure 7.6b), which are insensitive to the concentration variation.

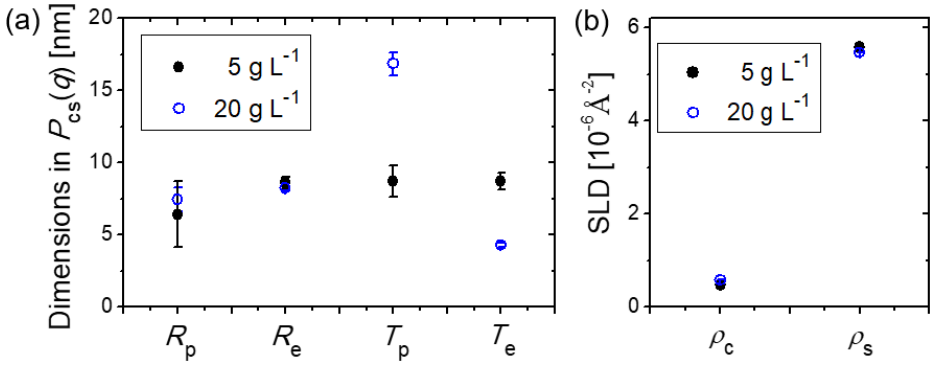

Figure 7.6 Structural parameters from the core-shell ellipsoid form factor $P_{cs}(q)$ at 25 °C, obtained by modeling the SANS data of P*b*E solution at 5 (black closed circles) and 20 g L^{-1} (blue hollow circles) in D_2O. (a) Polar radius R_p, equatorial radius R_e, polar thickness T_p and equatorial thickness T_e. (b) SLDs in the core ρ_c and the shell ρ_s.

The core part of P*b*E is composed of the hydrophobic, collapsed PPO blocks, which probably form a robust core. Therefore, the structure of the core part is not very sensitive to the varying concentration. On the other hand, the shell is composed of the water-swollen PEO blocks, which are mobile chains and able to adapt to the spatial limitation due to the concentration change. As the value of $T_p \approx T_e$ at 5 g L^{-1} is just between the value of T_p and T_e at 20 g L^{-1}, it is supposed that the spatial limitation at high concentration results in a distortion of the shell part. At high concentration, a mutual alignment of the MBs along the polar axis possibly happens, leading to a larger dimension in the polar direction than the equatorial direction. Similar observation has been reported for amphiphilic block copolymers, which form elongated micelles for the sake of reducing the interaction energy in equatorial direction [214, 215]. Thus, with increasing concentration, P*b*E keeps the size and shape of its PPO-rich core, while the water-swollen PEO blocks in the shell rearrange differently in the polar and the equatorial direction due to the mutual interaction between the MBs, as schematically shown in Figure 7.7.

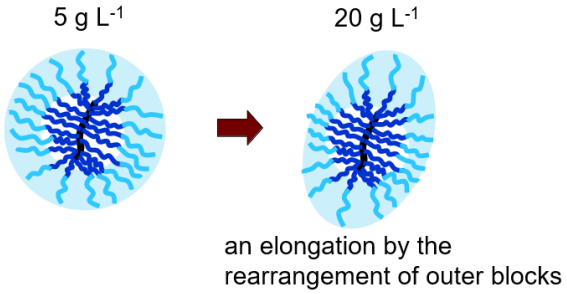

Figure 7.7 Schematic representation of the structural evolution of P*b*E from dilute to semi-dilute solutions. The brown arrow indicates an increase of the concentration. The black, dark blue and light blue lines mark the backbone, the PPO and the PEO, respectively. The bluish shading indicates the water-rich region.

For P*r*E, the structural parameters from $P_{cs}(q)$ at 5 and 20 g L^{-1} are shown together in Figure 7.8 for comparison. At 5 g L^{-1}, R_p = 12.0 nm and R_e = 7.5 nm, and T_p = 7.4 nm and T_e = 8.4 nm (Figure 7.8a, black closed circles), yielding an elongated ellipsoidal shape. This result matches the observation in the *cryo*-EM image of P*r*E (Figure 7.1b). At 20 g L^{-1}, R_p grows to 14.1 nm, while R_e stays at similar value to be 7.8 nm (Figure 7.8a, blue hollow circles). Thus, the core part becomes slightly larger with increasing concentration, implying a larger polymer-rich region in the MB. Regarding the shell thickness, T_p and T_e, are 5.8 nm and 6.0 nm at 20 g L^{-1}, respectively. Therefore, with increasing concentration, the shell thickness shrinks by 2-3 nm evenly at all directions. At 5 g L^{-1}, ρ_c (2.1×10^{-6} $Å^{-2}$) indicates 28 vol% of D_2O in the core, and ρ_s (5.9×10^{-6} $Å^{-2}$) indicates 93 vol% of D_2O in the shell (Figure 7.8b). These are compared with the D_2O content at 20 g L^{-1}, which are 9 vol% and 91 vol% in the core and the shell, respectively. Thus, it is found that the D_2O content in P*r*E generally decreases from low to high concentration, especially in its core part.

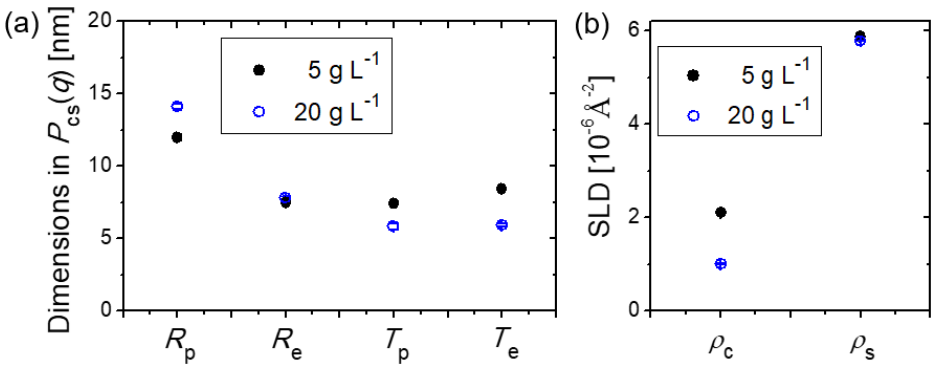

Figure 7.8 Structural parameters from the core-shell ellipsoid form factor $P_{cs}(q)$ at 25 °C, obtained by modeling the SANS data of P*r*E solution at 5 (black closed circles) and 20 g L^{-1} (blue hollow circles) in D_2O. (a) Polar radius R_p, equatorial radius R_e, polar thickness T_p and equatorial thickness T_e. (b) SLDs in the core ρ_c and the shell ρ_s.

As the PO and EO monomers are randomly distributed in the side chains of P*r*E, it is supposed that the side chains are flexible, being able to adapt to the spatial change. Upon an increase of the concentration, the polymer-rich core part slightly expands, while the water-rich shell part shrinks, which together suggest a decreasing water content in the MB. Moreover, the random distribution of the hydrophobic PO segment allows more water content especially in the core region at low concentration, and the amount of D_2O in the MB sees a decrease at a higher concentration. Thus, from low to high concentration, the random copolymer side chains rearrange to adapt to the decreasing space, shrinking evenly in all directions with a loss in the D_2O content, as schematically shown Figure 7.9.

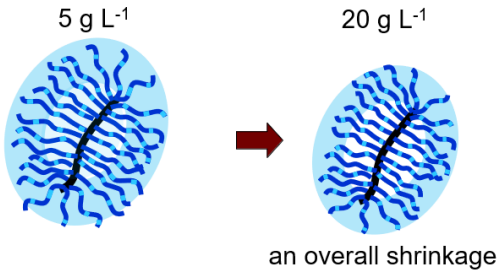

Figure 7.9 Schematic representation of the structural evolution of P*r*E from dilute to semi-dilute concentration. The brown arrow indicates an increase of the concentration. The black, dark blue and light blue lines mark the backbone, the PO and the EO monomers, respectively. The bluish shading indicates the water-rich region.

In terms of the correlation between the MBs, the P*b*E molecules seem to have stronger inter-correlation in the solution than the P*r*E molecules, since the structure factor is found only necessary for fitting the SANS data of the P*b*E solution at 5 g L^{-1}. At such low concentration, the presence of the inter-particle correlation between P*b*E is attributed to the relatively long side chains compared to the backbone length. As the fully stretched side chain length is about four times longer than the length of the backbone (Table 7.1), it is much likely for P*b*E to correlate with each other in space. On the contrary, for P*r*E, the side chain length is similar to the backbone length. As a result, the P*r*E molecules are not correlated in the solution at 5 g L^{-1}. The difference in the correlation strength further explains the structural change of P*b*E from 5 to 20 g L^{-1}, where the shell part shows unbalanced thickness in the polar and the equatorial direction at higher concentration, while such distortion in the shell part is not observed for P*r*E. The correlation between the MBs at 20 g L^{-1} is discussed in detail in chapter 7.6.

7.5 Temperature-resolved diffusional behavior

The LCST behavior below T_{cp} is investigated by DLS measurements on the solutions of P*b*E and P*r*E at 20 g L^{-1} in D_2O. Data were collected for both solutions during a heating scan starting from 25 °C. As the DLS measurement is prohibited above 60 °C for P*b*E and 38 °C for P*r*E, due to the high turbidity of the solution, these temperatures are considered the cloud points T_{cp} of the corresponding solution.

Shown in Figure 7.10a,b are the normalized intensity autocorrelation curves along with the fitting lines for both samples, where the bluish curves are data below T_{cp} and the reddish ones are data at T_{cp}. For P*b*E, the curves below T_{cp} shows single decay and gradually shifts toward lower delay time τ upon heating. At T_{cp} = 60 °C, the decay becomes broader and suddenly jumps to higher τ. For P*r*E, the curves do not change significantly below T_{cp}, while a slight shift at its T_{cp} = 38 °C to higher τ is observed. Figure 7.10c,d show the corresponding hydrodynamic radii R_h distribution. For P*b*E below T_{cp}, R_h distribution shows one peak attributed to the individually dissolved MBs, while at T_{cp}, there are two peaks, one has similar size as those below T_{cp}, and the other is larger by 1-2 orders of magnitude. Considering the increased hydrophobicity at high temperatures, the large one is supposedly contributed by the aggregates of the MBs. Namely, at T_{cp} of P*b*E solution, individual MBs are still present in the solution, with the appearance of the aggregates. For P*r*E solution, on the other hand, R_h

distribution always shows a single peak, which shifts to lager value at T_{cp}. Here, the diffusing particles below T_{cp} are considered to be individual MBs, while at T_{cp} they are aggregates. Namely, the coexistence of individual MBs and aggregates is not observed in P*r*E solution.

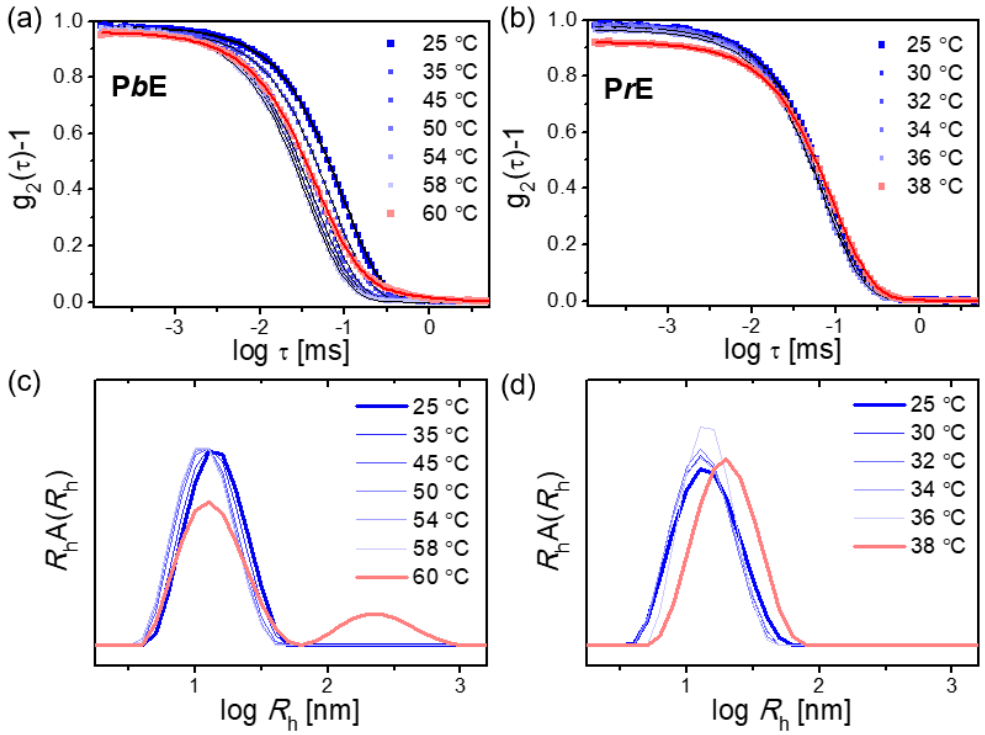

Figure 7.10 Temperature-resolved DLS data of P*b*E and P*r*E solutions at 20 g L^{-1} in D_2O. The representative normalized intensity autocorrelation data (symbols) along with the fitting lines (solid lines) of (a) P*b*E and (b) P*r*E. Hydrodynamic radii, R_h, distribution of (c) P*b*E and (d) P*r*E. Temperatures are as indicated.

R_h is plotted as a function of temperature in Figure 7.11, where its thermal dependence is clearly demonstrated. For P*b*E, R_h is around 16 nm at 25 °C, and it shows a continuous shrinkage as heating up to 58 °C, where it decreases to around 13 nm. At 60 °C, i.e., its T_{cp}, R_h of the MB is around 15 nm while R_h of the aggregates is about 450 nm. The decreasing MB size upon heating is presumably due to the dehydration and thus the collapse of the LCST side chains. For P*r*E, R_h is around 16 nm at 25 °C, which shows a shrinkage by around 1.5 nm in the beginning stage of heating, i.e., between 25 – 32 °C. Above 32 °C, R_h slightly increases by around 1 nm upon heating until aggregates form at 38 °C, which feature $R_h \approx 23$ nm. The initial shrinkage of P*r*E is attributed to the dehydration of the LCST side chains like the case in P*b*E solution. However, despite of the small variation, the reason for the subsequent increase of R_h

is not so clear. It could possibly be a result from the change in the MB shape, which needs to be clarified by a further investigation on the inner structure.

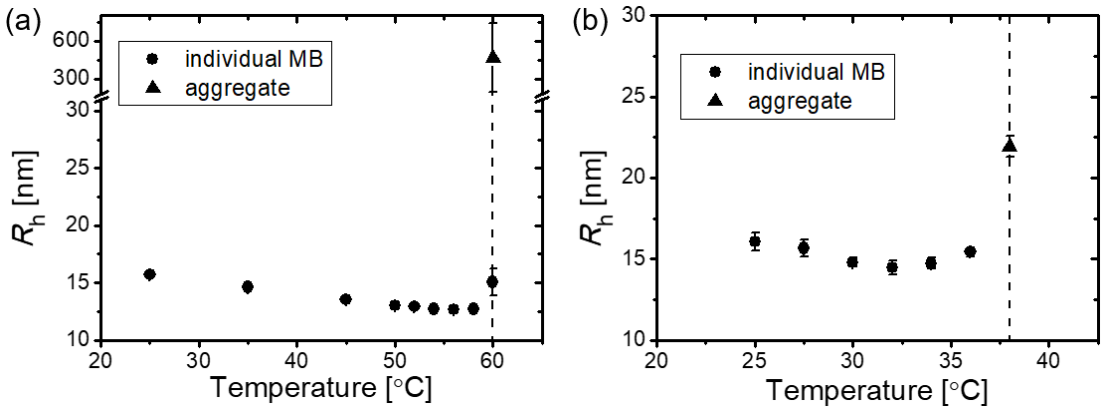

Figure 7.11 Temperature dependence of hydrodynamic radius R_h of individual MB (spheres) and aggregates (triangles) in (a) P*b*E solution and (b) P*r*E solution. The vertical dashed lines indicate T_{cp} of the solution.

From the DLS measurements, significantly different T_{cp} are found for P*b*E (60 °C) and P*r*E (38 °C) solutions in D_2O at 20 g L^{-1}, despite of the same PO weight fraction in the MBs. The high T_{cp} of P*b*E solution is attributed to the block copolymer side chain architecture, where the hydrophobic PPO inner block (T_{cp} = 8 °C) is well protected from the aqueous environment by the hydrophilic PEO outer block (T_{cp} > 100 °C). On the contrary, in P*r*E molecule, the PO and EO monomers are randomly distributed, thus the aggregation happens at a lower temperature.

The monomer sequence also seems to result in different phase transitions at the corresponding T_{cp}. It reflects on the presence of the individually dissolved MB at T_{cp}, which is the case for P*b*E solution but not for P*r*E solution. Supposedly, the high T_{cp} of the PEO block in P*b*E facilitates the solubility in water at high temperatures. Thus, for P*b*E solution at 60 °C, the overall hydrophobicity leads to the aggregation of a portion of the MBs, while the rest of the MBs are still molecularly dissolved in the solution. Such phenomenon is again observed in the small-angle scattering measurements, and is discussed in details in chapter 7.6.1.

7.6 Temperature-resolved structural evolution

SANS measurements were performed on the same P*b*E and P*r*E solutions as for the DLS measurements, namely solutions in D_2O at 20 g L^{-1}. Data were collected for both samples during a heating scan. For P*b*E (T_{cp} = 60 °C), the temperature range was 25 – 66 °C, and for P*r*E (T_{cp} = 38 °C), it was 25 – 46 °C.

Figure 7.12 shows the SANS data below T_{cp} for both sample solutions, along with the model fits. The data of P*b*E below T_{cp}, i.e., from 25 to 58 °C, show a broad maximum at $q \approx 0.1$ nm^{-1} and an additional fringe at 0.7 nm^{-1} (Figure 7.12a,c). During heating from 25 °C, the scattering curves show little dependence on temperature until 58 °C, where there is a rather clear shift of the maximum position towards low q and the peak becomes shallower. For P*r*E, the data between 25 – 32 °C feature a broad maximum at $q \approx 0.15$ nm^{-1}, a decay shoulder between 0.2 – 0.6 nm^{-1} and a scattering tail at $q > 0.1$ nm^{-1}, showing weak temperature-dependence (Figure 7.12b,d). Further heating above 32 °C, the intensity successively increases, and the maximum position shifts gradually towards lower q while the peak becomes more pronounced. For the two kinds of MBs, the different features of the SANS data imply different inner structure and the structural dependence on temperature. This is supposedly due to the different dehydration process of the copolymer side chains with random or block monomer sequence.

The scattering below T_{cp} is contributed by the individually dissolved MBs, and the broad maximum is coming from their spatial ordering. Therefore, the data is modeled by the core-shell ellipsoid form factor $P_{cs}(q)$ for the MB, which is combined with the hard-sphere structure factor $S_{HS}(q)$ for the correlation between them. Additionally for P*r*E solution, a modified Ornstein-Zernike equation is included in the model for the scattering at $q > 0.1$ nm^{-1}, coming from the density fluctuation at small length scales in the solution.

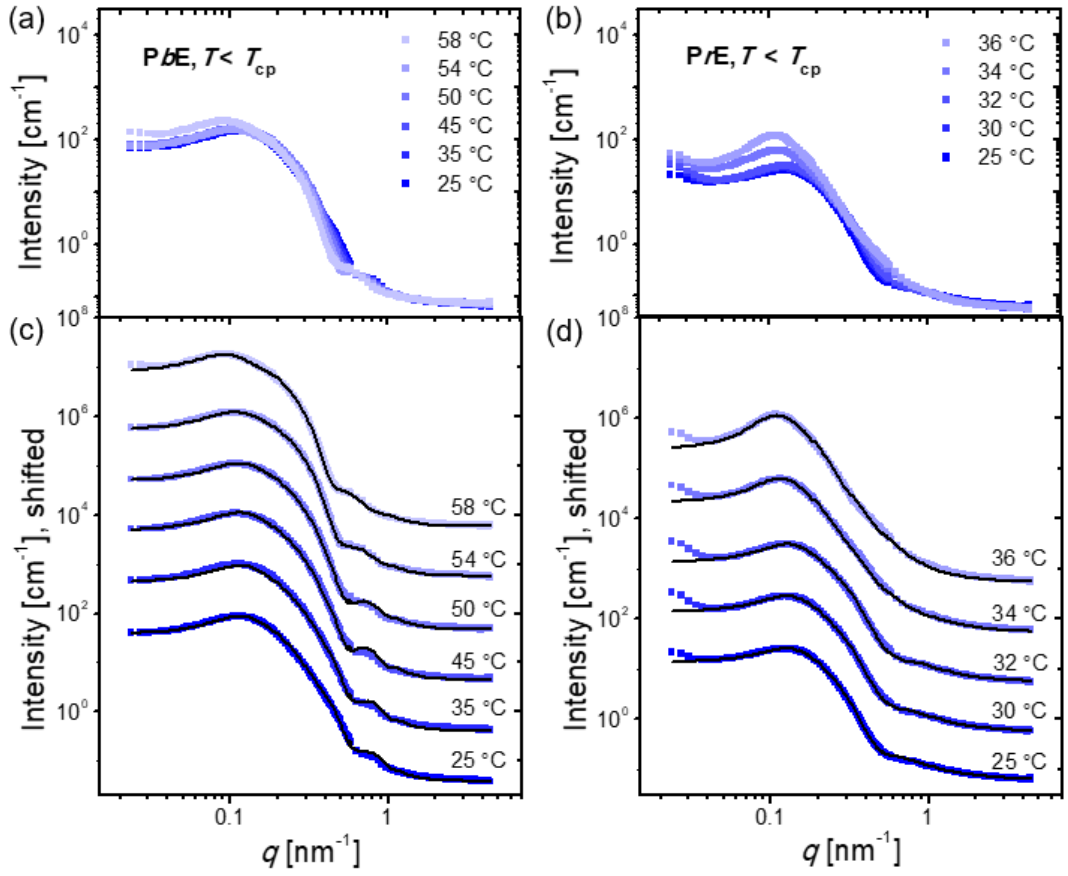

Figure 7.12 SANS data (symbols) below T_{cp} of (a,c) P*b*E and (b,d) P*r*E solutions at 20 g L^{-1} in D_2O. In (c) and (d), the data are shown together with the model fits (solid lines), which are vertically shifted by a factor of 10 with respect to each other for better visibility. The temperatures are indicated in the graphs.

The SANS data above T_{cp} with the model fits are shown in Figure 7.13. Compared to the data below T_{cp}, a significant increase in the low q scattering intensity is observed for both samples, which is attributed to the presence of aggregates in the solution. The data of P*b*E solution show a series of changes between 60 – 64 °C (Figure 7.13a,c): at T_{cp} = 60 °C, it features the low q scattering and the decay shoulder between 0.2 – 0.6 nm^{-1}, namely the scattering of the aggregates and the individual MBs, respectively; at 62 °C, the low q scattering is enhanced, and the decay shoulder is weakened, while an additional peak emerges at 0.3 nm^{-1}, which is supposedly due to the correlation between the aggregating MBs; further at 64 °C, the decay shoulder completely disappears, leaving the strong low q scattering and the sharp peak at 0.3 nm^{-1}. At 66 °C, the data slow down the evolution with temperature, and is very similar to the curve at 64 °C. As for P*r*E solution (Figure 7.13b,d), at T_{cp} = 38 °C, the low q scattering is

shown together with a maximum at 0.08 nm^{-1}, and a correlation peak appears at 0.6 nm^{-1}. As the maximum at low q (0.08 nm^{-1}) is attributed to the spatial correlation between the aggregates, the peak (0.6 nm^{-1}) is supposed to come from the correlation between the closely packed MBs composing the aggregates. Further heating to 40 °C, the low q intensity grows by 10 times, and all the above-mentioned features shift to lower q: the maximum shifts to 0.05 nm^{-1}, and the correlation peak shifts to 0.4 nm^{-1}. At higher temperatures, i.e., 42 – 46 °C, the data only show small change with temperature, and the major features are the same as at 40 °C. For the two samples, above the corresponding T_{cp}, the different characteristics in SANS data as well as its dependence on temperature point to the differences in the aggregation behavior at high temperatures.

For the SANS modeling, scattering of the aggregates are described by the Guinier-Porod empirical model, revealing their size and shape as well as the surface roughness. This term is used as it is for P*b*E, while it is combined with a hard-sphere structure $S_{HS,agg}(q)$ for P*r*E, due to the spatial correlation of the P*r*E aggregates. As for the closely packed MBs composing the aggregates, the fuzzy sphere form factor $P_{fz}(q)$ is used, and the hard-sphere structure factor $S_{HS'}(q)$ is combined with $P_{fz}(q)$ to account for their correlation. The fitting model for P*r*E additionally includes the modified Ornstein-Zernike term.

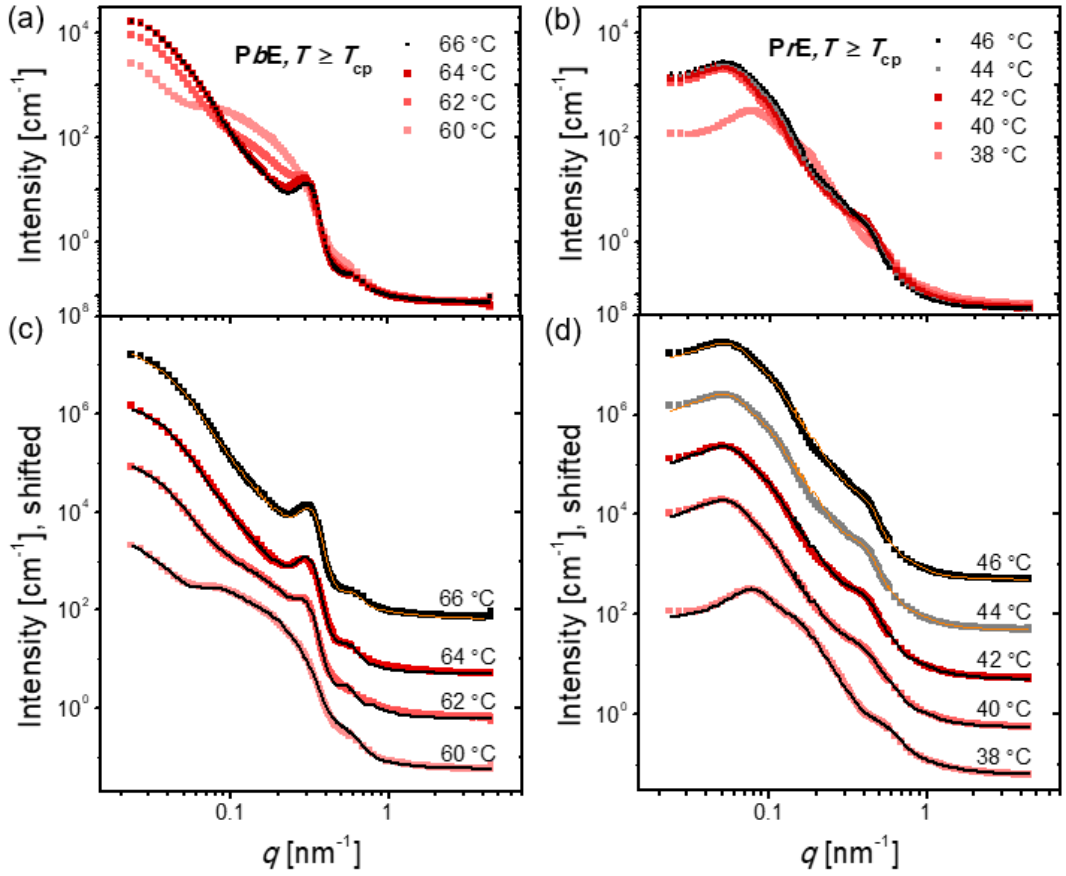

Figure 7.13 SANS data (symbols) above T_{cp} of (a,c) P*b*E and (b,d) P*r*E solutions at 20 g L^{-1} in D_2O. In (c) and (d), the data are shown together with the model fits (solid lines), which are vertically shifted by a factor of 10 with respect to each other for better visibility. The temperatures are indicated in the graphs.

For both samples, the temperatures, where the aggregates show up are consistent with the temperatures found in the DLS measurements. Moreover, the coexistence of individual MBs and aggregates in P*b*E solution at 60 °C is again observed by SANS measurements. From the model fitting results, the structural changes of the MBs as well as the aggregates are revealed. These are discussed in detail in the following two sections for P*b*E and P*r*E, respectively.

7.6.1 MB with block copolymer side chains

Dehydration process below T_{cp}. For P*b*E solution at 20 g L^{-1} in D_2O, the scattering of the individually dissolved MBs is found between 25 – 62 °C in the SANS data (Figure 7.12a,c and Figure 7.13a,c), which is modeled by the core-shell ellipsoid form factor $P_{cs}(q)$. The structural

parameters from $P_{cs}(q)$ are plotted against temperature in Figure 7.14, including the core polar radius R_p, the core equatorial radius R_e, the core SLD ρ_c, the shell polar thickness T_p, the core equatorial radius T_e and the shell SLD ρ_s.

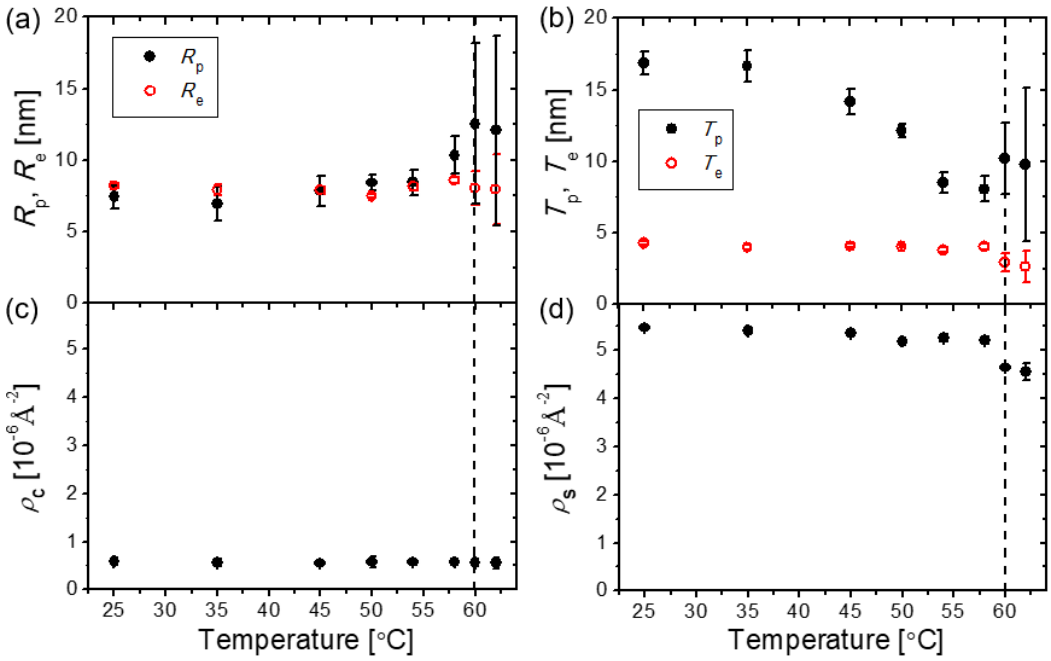

Figure 7.14 Structural parameters from the core-shell ellipsoid form factor $P_{cs}(q)$ from 25 to 62 °C, obtained by modeling the SANS data of P*b*E solution at 20 g L^{-1} in D_2O. (a) Dimensions in the core part: polar radius R_p (closed black circles) and equatorial radius R_e (open red circles). (b) Dimensions in the shell part: polar thickness T_p (closed black circles) and equatorial thickness T_e (open red circles). (c) SLD in the core, ρ_c. (d) SLD in the shell, ρ_s. The vertical dashed lines indicate T_{cp} of the solution.

It is shown that, despite of the small inequality, R_p and R_e are around 7.5 nm between 25 and 54 °C (Figure 7.14a), meaning a spherical core region of the MBs. At 58 °C, R_p becomes obviously larger than R_e, and the inequality is even more significant at T_{cp} = 60 °C, where R_p = 12.5 nm and R_e = 8.1 nm. Thus, the core region keeps the spherical shape upon heating up to T_{cp}, where it transforms to an elongated shape. ρ_c is found to be 0.6 × 10^{-6} Å^{-2} in the full temperature range (Figure 7.14c), which is close to the SLD of the inner PPO block (0.34 × 10^{-6} Å^{-2}). An estimate of the D_2O content can be made by the SLD of PPO and D_2O (6.33 × 10^{-6} Å^{-2}), which are supposed to be the main components in the core part of P*b*E. This gives a D_2O content of 3 vol%, unchanged with temperature. The stable size in the core, in combination with the low D_2O content, is explained by the low T_{cp} (8 °C) of PPO, making it essentially water-

insoluble in the detected temperature range, thus staying hydrophobic and collapsed all along. The elongated shape at 60 and 62 °C, however, is related to the continuous dehydration of the outer PEO block in the shell part, influencing the overall shape of the MB. It is discussed together with the parameters from the shell in the following paragraph.

At 25 °C, T_p (16.8 nm) is significantly larger than T_e (4.3 nm) (Figure 7.14b), resulting in an overall elongated shape of the MB. With increasing temperature, T_p shows a decreasing trend down to 8.1 nm at 58 °C and then slightly increases to 10.2 nm at 60 °C, while T_e stays unchanged between 25 – 58 °C and decreases to 3.0 nm at 60 °C. The shrinking T_p is presumably due to the dehydration and thus a contraction of the PEO blocks, while the unchanged T_e is due to the spatial restriction in the equatorial direction. The dehydration of the PEO blocks is characterized by the variation of ρ_s (Figure 7.14d), where D_2O content decreases from 84.9 vol% at 25 °C to 80.1 vol% at 58 °C, estimated by the SLD of PEO (0.64×10^{-6} Å^{-2}) and D_2O. Namely, P*b*E features a water-rich shell at room temperature, and it undergoes a very weak dehydration upon heating to 58 °C. At T_{cp}, the D_2O content in the shell further drops to 70.3 vol%, implying a larger amount of water repelled out of the MB. Meanwhile, from 58 to 60 °C, the aspect ratio of the ellipsoidal MB slightly increases, since the total length in the polar direction ($R_p + T_p$) increases while that in the equatorial direction ($R_e + T_e$) decreases. Such shape change indicates that, the further dehydration at 60 °C possibly leads to a rearrangement of the PEO blocks during the continuous collapse.

The spatial correlation between the MBs is modeled by the hard-sphere structure factor $S_{HS}(q)$. R_{HS}, considered as half the average distance between the MBs, is 22 nm at 25 °C. It stays constant between 25 – 50 °C and starts increasing at 54 °C until it reaches 32 nm at 54 °C (Figure 7.15a), indicating the MBs become further away from each other as the temperature approaches T_{cp}. η is regarded as the volume fraction of the correlated MBs in the sample, so it further indicates the correlation strength. It stays at 0.17 between 25 – 45 °C, and then starts to decrease in small steps upon further heating, until it becomes 0.11 at 60 °C (Figure 7.15b). Thus, the correlation strength gets weaker as temperature approaches T_{cp}. For the dependence on temperature of both R_{HS} and η, especially above 50 °C, an explanation could be that the total number of the correlated MBs is decreasing. Namely, a certain amount of the MBs become randomly distributed in the solution, resulting in a longer distance as well as a weaker correlation between the MBs.

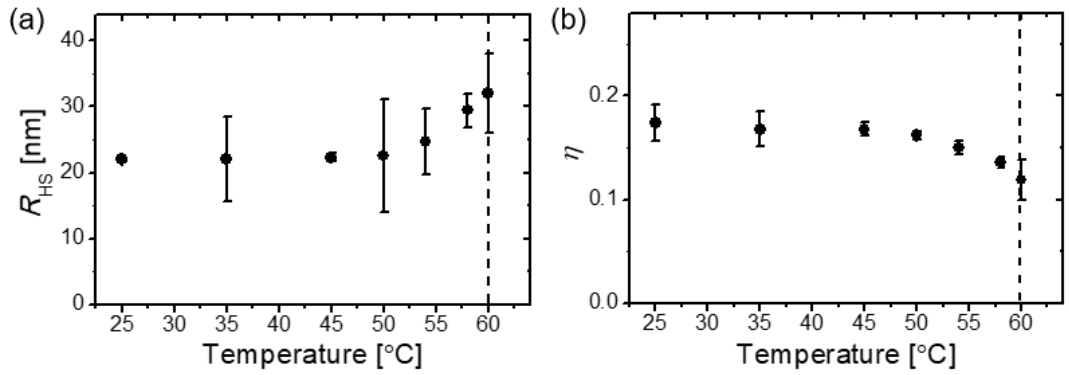

Figure 7.15 Structural parameters from the hard-sphere structure factor $S_{HS}(q)$ from 25 to 62 °C, obtained by modeling the SANS data of P*b*E solution at 20 g L^{-1} in D_2O. (a) Hard-sphere radius R_{HS}. (b) Hard-sphere volume fraction η. The vertical dashed lines indicate T_{cp} of the solution.

The SANS model fitting results of P*b*E solution between 25 – 60 °C reveal that the inner structure of P*b*E is rather stable upon heating from room temperature up to 45 °C. Above 45 °C, P*b*E shows firstly a shrinkage between 45 – 58 °C, and then a slight extension at 60 °C. As the inner PPO blocks are water-insoluble and thus stays collapsed in the core region all along, the temperature dependence of the MB structure above 45 °C is driven by the dehydration of the outer PEO blocks, with a moderate decrease in the D_2O content.

Upon heating the P*b*E solution, aggregates appear at 60 °C due to the increasing hydrophobicity, evidenced by the high scattering intensity at low q of the SANS data (Figure 7.13a,c). Meanwhile, some of the MBs are still present as individual ones in the solution during 60 – 62 °C. At 62 °C, these individually dissolved MBs feature similar inner structure as at 60 °C (Figure 7.14), while there is no correlation between them ($S_{HS}(q) = 1$). Further at 64 °C and 66 °C, no contribution from the individual MBs is observed, and the scattering comes completely from the aggregates.

Aggregation above T_{cp}. The scattering of the aggregates between 60 – 66 °C is described using the empirical Guinier-Porod model, which gives the size and the approximate shape of the aggregates. From the Guinier term, the gyration of gyration of the aggregates, $R_{g,agg}$, and the shape factor s are obtained. $R_{g,agg}$ is 73 nm when the aggregates show up in the solution at 60 °C, and gradually decreases to 58 nm at 66 °C (Figure 7.16a). The shrinkage is possibly due to the continuous dehydration and thus a contraction of the PEO blocks in this temperature range . Meanwhile, s stays around zero (Figure 7.16b), implying the spherical overall shape of the

aggregates all along. From the Porod term, the Porod exponent α is found to be around 4 and hardly changes with temperature (Figure 7.16c), which hints at smooth surfaces of the aggregates.

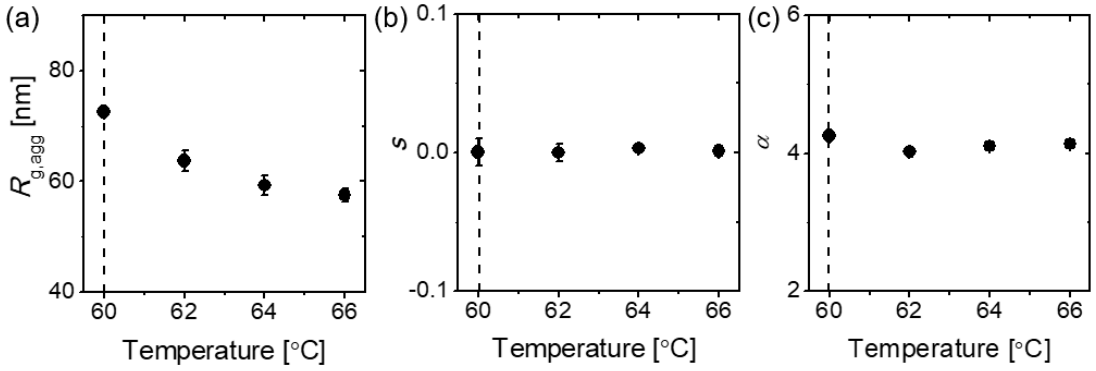

Figure 7.16 Structural parameters from the Guinier-Porod model for the aggregate scattering $I_{agg}(q)$ from 60 to 66 °C, obtained by modeling the SANS data of P*b*E solution at 20 g L^{-1} in D_2O. (a) Radius of gyration of the aggregates, $R_{g,agg}$. (b) Shape factor, *s*. (c) Porod exponent α. The vertical dashed lines indicate T_{cp} of the solution.

At 62 °C, a peak emerges at q = 0.3 nm^{-1} in the SANS data and this is enhanced with increasing temperature up to 66 °C (Figure 7.13a,c), which is attributed to the correlation between the closely packed MBs in the aggregates. These constituent MBs are modeled by the fuzzy sphere form factor $P_{fz}(q)$, and the fuzzy sphere radius R_{fz} and the fuzziness *f* are resolved. $P_{fz}(q)$ is combined with the hard-sphere structure factor $S_{HS'}(q)$, giving the hard-sphere radius $R_{HS'}$ as well as the hard-sphere volume fraction η' of the MBs composing the aggregates. From $P_{fz}(q)$, R_{fz} is found to be around 10 nm, which faintly decreases upon heating, and *f* being 3 nm, independent on temperature (Figure 7.17a). In $P_{fz}(q)$, the SLD smoothly varies in the radial direction until it reaches the SLD value of the solvent at radius R_{fz} + 2*f* (see Figure 4.6), which is thus considered the overall radius of the MBs composing the aggregates. The values of R_{fz} + 2*f* are calculated to be around 16 nm (Figure 7.17a, open circles), and compared with the values of $R_{HS'}$, which are around 11 nm (Figure 7.17b, closed black circles, left scale). As R_{fz} + 2*f* is always lager than $R_{HS'}$, it is indicated that the MBs partially overlap at the periphery. This is further interpreted as the interpretation of the side chains. Based on this finding, the spatial correlation between MBs in the aggregates can be drawn schematically in Figure 7.17c. Moreover, the high η' value of about 0.5 (Figure 7.17b, open blue circles, right scale) indicates high correlation strength between these MBs. Considering the partial interpenetration as well

as the high correlation strength, the MBs are strongly connected with each other to form the P*b*E aggregates.

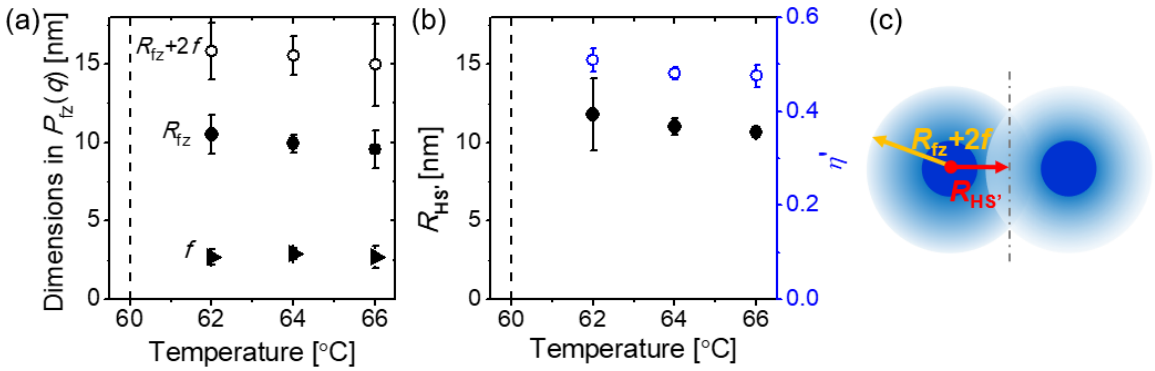

Figure 7.17 Structural parameters from the fuzzy sphere form factor $P_{fz}(q)$ and the hard-sphere structure factor $S_{HS'}(q)$ from 60 to 66 °C, obtained by modeling the SANS data of P*b*E solution at 20 g L^{-1} in D_2O. (a) Dimensions in $P_{fz}(q)$: fuzzy sphere radius R_{fz} (closed circles), fuzziness f (closed triangles) and $R_{fz} + 2f$ (open circles). (b) Parameters from $S_{HS'}(q)$: hard-sphere radius $R_{HS'}$ (closed black circles, left scale) and volume fraction η' (open blue circles, right scale). The vertical dashed lines indicate T_{cp} of the solution. (c) Schematic representation of the correlation between the MBs composing the aggregates, comparing $R_{fz} + 2f$ with $R_{HS'}$. The vertical dash-dotted line indicates the center between two fuzzy spheres.

To summarize the structural evolution of P*b*E in aqueous solutions in dependence on temperature, the results from SANS analysis are shown schematically in Figure 7.18. Upon heating from room temperature to just below T_{cp}, the MBs show a shrinkage in size due to the dehydration of the PEO block, accompanied by a moderate decrease of the water content. At T_{cp}, some individually dissolved MBs present together with large aggregates, which are composed of loosely structured MBs, in the solution. Further above T_{cp}, individual MBs disappear, and aggregates are formed by closely packed MBs. The aggregates feature a spherical shape and smooth surfaces, and the constituent MBs strongly connect with each other in the aggregates.

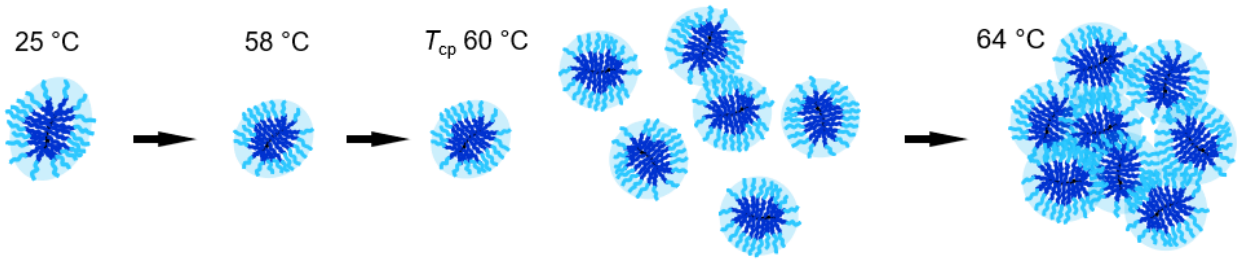

Figure 7.18 Schematic representation of the structural evolution of P*b*E in aqueous solutions, from room temperature to T_{cp} and further above. The black arrows indicate the heating process. The black, dark blue and light blue lines mark the backbone, the PPO and the PEO blocks, respectively. The bluish shading indicates the water-rich region.

7.6.2 MB with random copolymer side chains

Dehydration process below T_{cp}. For P*r*E solution at 20 g L^{-1} in D_2O, individually dissolved, corelated MBs are found between 25 – 34 °C in the SANS data (Figure 7.12b,d), modeled by the core-shell ellipsoid form factor $P_{cs}(q)$. In Figure 7.14, the structural parameters from $P_{cs}(q)$ are plotted with temperature, including the core polar radius R_p, the core equatorial radius R_e, the core SLD ρ_c, the shell polar thickness T_p, the core equatorial radius T_e and the shell SLD ρ_s.

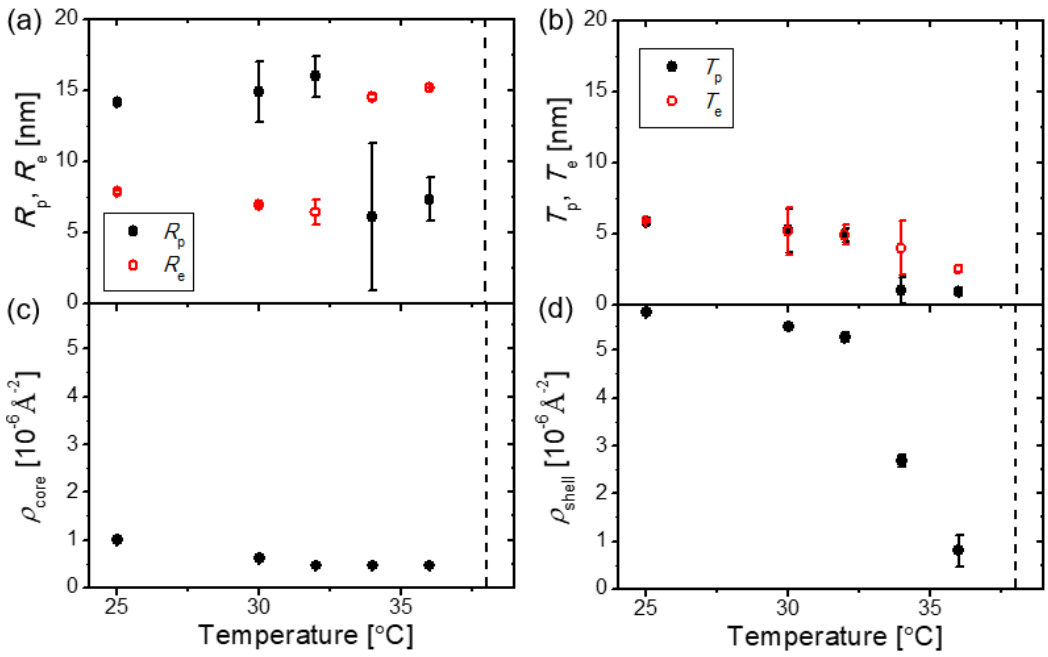

Figure 7.19 Structural parameters from the core-shell ellipsoid form factor $P_{cs}(q)$ from 25 to 36 °C, obtained by modeling the SANS data of P*r*E solution at 20 g L^{-1} in D_2O. (a) Dimensions in the core part: polar radius R_p (closed black circles) and equatorial radius R_e (open red circles). (b) Dimensions in the shell part: polar thickness T_p (closed black circles) and equatorial thickness T_e (open red circles). (c) SLD in the core, ρ_c. (d) SLD in the shell, ρ_s. The vertical dashed lines indicate T_{cp} of the solution.

At 25 °C, R_p and R_e are 14 and 8 nm, respectively (Figure 7.19a), while T_p and T_e show similar values to be 6 nm (Figure 7.19b). Between 25 – 32 °C, R_p slightly increases by 2 nm and R_e shows a small decrease by 2 nm, while T_p and T_e both decrease by about 1 nm. Estimated by ρ_c, ρ_s and the volume-weighted average SLD of PPO and PEO (0.43×10^{-6} Å^{-2}), the D_2O content in the core decreases from 9 vol% (25 °C) to only 0.5 vol% (32 °C) (Figure 7.19c), while the D_2O content in the shell also shows a decreasing trend from 90.7 vol% to 81.9 vol% (Figure 7.19d). Thus, between 25 – 32 °C, the temperature dependence of the parameters implies a slight extension of the MB upon heating, accompanied by a moderate dehydration. Further heating from 32 to 34 °C, R_p suddenly drops to 6 nm, while R_e jumps to 15 nm, and then both grow faintly at 36 °C. Meanwhile, T_p decreases down to only 1 nm and T_e to 2.5 nm. Between 32 – 36 °C, the core D_2O content stays almost water-free, namely 0.5 vol%, and the D_2O content in the shell show a drastic drops, where it reaches 6.3 vol% at 36 °C. Thus, during 32 – 36 °C, the MBs significantly dehydrate. The gradual collapse of the P(PO-*ran*-EO) side chains upon heating is supposed to be responsible for the mild shape change between 25 – 32

°C and the following severe transformation at 34 °C, where the polymeric backbone firstly straightens and then coils up due to the strong dehydration.

Regarding the correlation between P*r*E, R_{HS} is 20 nm at 25 °C, which firstly shows a vague increase upon heating, followed by a steady rise to 26 nm at 36 °C (Figure 7.20a), meaning the MBs become further away from each other upon heating towards T_{cp}. This might be attributed to the change in size and shape of the MBs, described in the previous paragraph, especially the noticeable structural changes during 32 – 36 °C. Meanwhile, η shows firstly a shallow and then significant increase from 0.16 (25 °C) to 0.27 (36 °C) (Figure 7.20b), implying the interaction between MBs is strengthened by heating. Considering the large loss of the D_2O content with increasing temperature, the hydrophobicity of the MBs is supposed to increase fiercely, leading to the enhanced interaction.

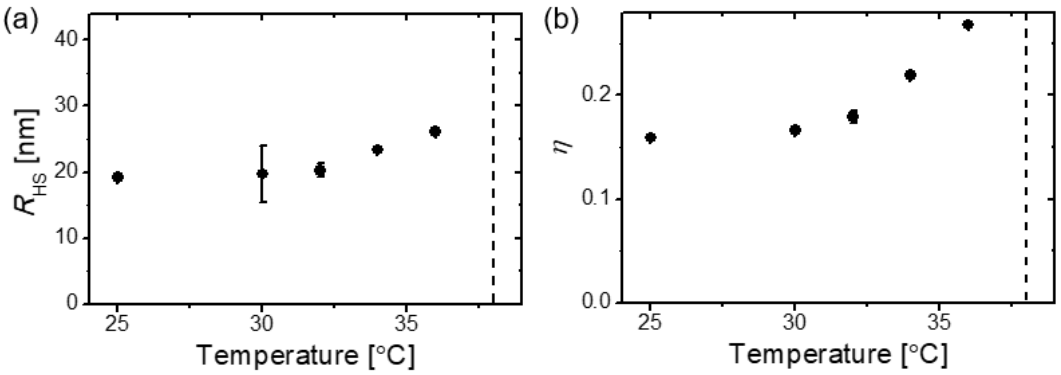

Figure 7.20 Structural parameters from the hard-sphere structure factor $S_{HS}(q)$ from 25 to 36 °C, obtained by modeling the SANS data of P*r*E solution at 20 g L^{-1} in D_2O. (a) Hard-sphere radius R_{HS}. (b) Hard-sphere volume fraction η. The vertical dashed lines indicate T_{cp} of the solution.

The structural changes of P*r*E in the aqueous solution between 25 – 36 °C is resolved by SANS. From 25 to 32 °C, a mild dehydration and thus a slight straightening of the MBs is observed. This is followed by a subsequent drastic loss in water content during 32 – 36 °C, and the sever collapse of the LCST side chains results in a significant deformation of the MB from a rod-like to a disk-like shape. It is supposed that, the continuous dehydration of the P(PO-*r*-EO) side chains is responsible for the above described structural variations upon heating, until aggregates set in at T_{cp} = 38 °C.

Aggregation above T_{cp}. At 38 °C, the MBs gather closely to form aggregates, leaving no

individually present ones, which is different from the case in P*b*E solution at its T_{cp}. The Guinier-Porod model is used to account for the scattering from the aggregates $I_{agg}(q)$, and a hard-sphere structure factor, $S_{HS,agg}(q)$, is multiplied with $I_{agg}(q)$ to describe the correlation between the aggregates. $R_{g,agg}$, is only 14 nm at 38 °C (Figure 7.21a), then grows to 26 nm at 40 °C, which decreases vaguely upon further heating. It is indicated that the MBs possibly rearrange to form into larger aggregates from 38 to 40 °C, while the increasing hydrophobicity leads to the subsequent slight shrinkage. $R_{HS,agg}$, which hints at the inter-aggregate distance, shows an increase accordingly with the growing size at 40 °C (Figure 7.21b, closed black circles, left scale) and stays constant above 40 °C. Meanwhile, η_{agg} stays nearly unchanged all along (Figure 7.21b, open blue circles, right scale). Thus, the variation of both $R_{HS,agg}$ and η_{agg} supports the hypothesis about a rearrangement of the aggregates between 38 and 40 °C. The shape factor *s* stays at zero (Figure 7.21c), suggesting a spherical overall shape. The Porod exponent α has values above 4 and close to 5 (Figure 7.21d), meaning there is a local concentration gradient at the aggregate surface.

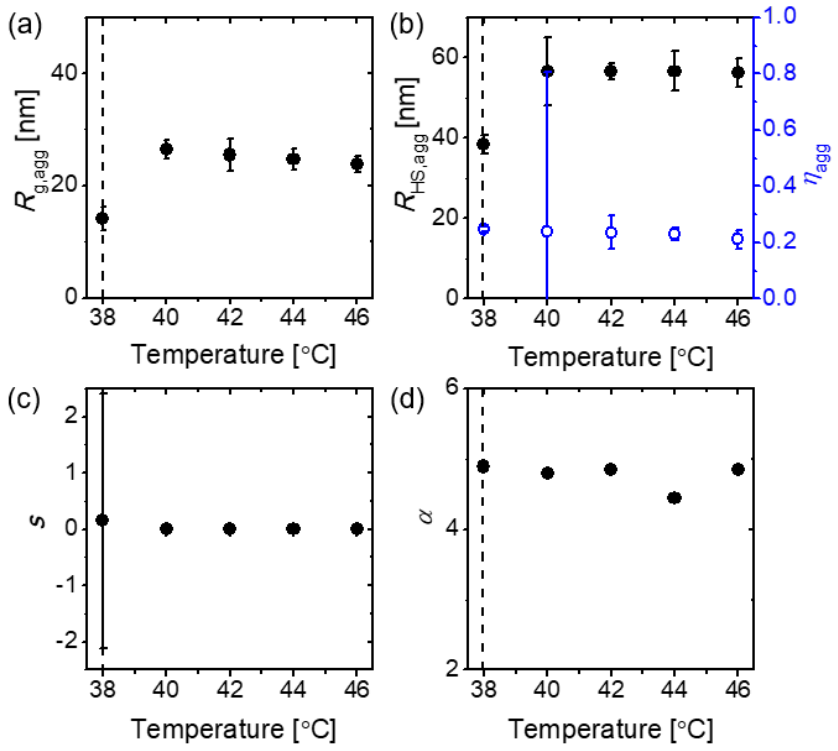

Figure 7.21 Structural parameters from the Guinier-Porod model for the aggregate scattering $I_{agg}(q)$, combined with the hard-sphere structure factor $S_{HS,agg}(q)$, from 38 to 46 °C, obtained by modeling the SANS data of P*r*E solution at 20 g L^{-1} in D_2O. (a) Radius of gyration of the aggregates, $R_{g,agg}$. (b) Parameters from $S_{HS,agg}(q)$: hard-sphere radius $R_{HS,agg}$

(closed black circles, left scale) and volume fraction η_{agg} (open blue circles, right scale). (c) Shape factor, *s*. (d) Porod exponent α. The vertical dashed lines indicate T_{cp} of the solution.

The MBs composing the aggregates is modeled in the same way as the ones in P*b*E solution. At 38 °C, they feature R_{fz} of 4 nm and *f* of 0.6 nm (Figure 7.22a). Thus the overall size, i.e., R_{fz} + 2*f* (Figure 7.22a, open circles), is very close to $R_{HS'}$ (Figure 7.22b, closed black circles, left scale). Based on these values, the spatial correlation between the MBs in the aggregates is drawn in Figure 7.22c, where the MBs do not interpenetrate with their neighboring ones. At 40 °C, both R_{fz} + 2*f* and $R_{HS'}$ increase by about 2 nm, keeping the correlation between the MBs. Above 42 °C, R_{fz} + 2*f* steadily increases, while $R_{HS'}$ stays unchanged, implying a closer packing between the MBs at temperatures much above T_{cp}. As for η', it shows a sudden drop from 0.32 at 38 °C to 0.19 at 40 °C (Figure 7.22b, open blue circles, right scale). This is explained by the rearrangement of the aggregates mentioned in the previous paragraph, which results in a loss of the inter-correlation between the MBs. Above 40 °C, η' continuously increases until it reaches similar values before the rearrangement, i.e., $\eta' \approx 0.3$, at 46 °C. Thus, between 40 – 46 °C, the interaction between the MBs is gradually enhanced, and it finally reaches the interaction strength as it is at 38 °C.

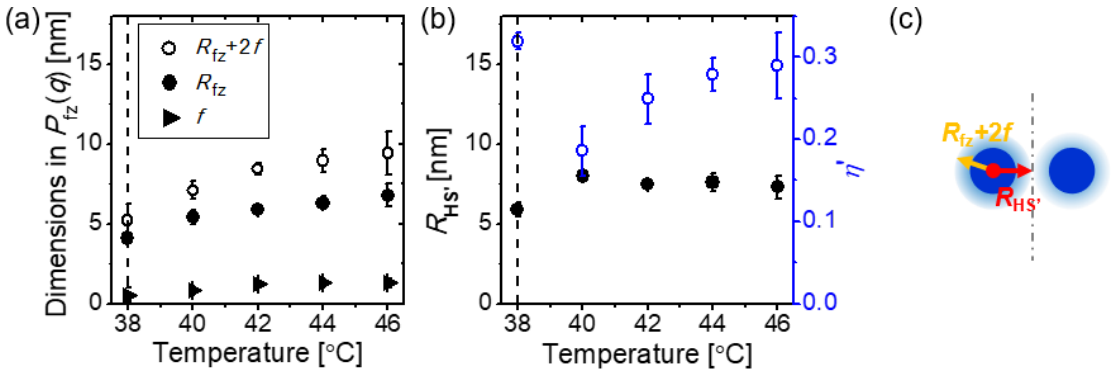

Figure 7.22 Structural parameters from the fuzzy sphere form factor $P_{fz}(q)$ and the hard-sphere structure factor $S_{HS'}(q)$ from 38 to 46 °C, obtained by modeling the SANS data of P*r*E solution at 20 g L^{-1} in D_2O. (a) Dimensions in $P_{fz}(q)$: fuzzy sphere radius R_{fz} (closed circles), fuzziness *f* (closed triangles) and R_{fz} + 2*f* (open circles). (b) Parameters from $S_{HS'}(q)$: hard-sphere radius $R_{HS'}$ (closed black circles, left scale) and volume fraction η' (open blue circles, right scale). The vertical dashed lines indicate T_{cp} of the solution. (c) Schematic representation of the correlation between the MBs composing the aggregates, comparing R_{fz} + 2*f* with $R_{HS'}$. The vertical dash-dotted line indicates the center between

two fuzzy spheres.

A comparison between PbE and PrE aggregation. Comparing the aggregates of P*r*E with the ones of P*b*E in aqueous solutions, it is found that, the P*b*E aggregate size is significantly larger than the size of P*r*E aggregates, revealed by their $R_{g,agg}$ (Figure 7.16a and Figure 7.21a). Moreover, in P*b*E solution, MBs composing the aggregates are strongly connected with each other, while the MBs in P*r*E solution merely agglomerate together without close connection, reflected by the relative values between $R_{fz} + 2f$ and R_{HS}, (Figure 7.17a,b and Figure 7.22a,b).

The different aggregation behavior is supposedly related to the dehydration level, which influences the side chain mobility [216-218], before the formation of aggregates at the corresponding T_{cp}. Evaluated by comparing the length scale of the ellipsoid from $P_{cs}(q)$ below T_{cp}, and the length scale of the sphere from $P_{fz}(q)$ above T_{cp}, P*b*E features similar size below and above T_{cp}. It could be thus deduced that P*b*E own high D_2O content above T_{cp}, just like below T_{cp}. The side chains, or more precisely the PEO blocks, in the dehydrated state have high mobility, and it is thus easier for the MBs to grow into large aggregates by interacting and connecting with the neighboring MBs with the mobile side chains. On the other hand, the size of P*r*E becomes much smaller from below to above T_{cp}. This points to an extremely low D_2O content in P*r*E above T_{cp}, as they are already severely dehydrated below T_{cp}. The low D_2O content results in a low chain mobility, hampering the growth of the aggregates. Therefore, the P*r*E aggregates seem like small clusters, where the MBs are loosely connected.

Besides the dehydration level, the molecular architecture also affects the side chain mobility. As listed in Table 7.1, P*b*E has a larger length ratio between the backbone and the side chains, compared to P*r*E. With such structure, the side chains on P*b*E experience less spatial constraint, compared to those on P*r*E, especially at the periphery part of the MB. This is also considered to be the reason why P*b*E grows into larger aggregates, since less spatial limitation brings higher chain mobility.

Local concentration fluctuations. In the full temperature range, from below to above T_{cp}, the scattering due to the concentration fluctuation, $I_{fluct}(q)$, is included in the fitting model for P*r*E solution, where the modified Ornstein-Zernike structure factor is used. The characteristic correlation length ξ of the local concentration fluctuation has a value around 1.5 nm all along, showing no particular trend (Figure 7.23a). The exponent m is 1.8 at 25 °C, and gradually increases to 2.8 at 36 °C (Figure 7.23b), meaning the solvent quality becomes poorer upon

heating towards T_{cp}. Above T_{cp}, m stays around 2.8, insensible to the temperature variation. $I_{fluct}(q)$ is only found necessary for the P*r*E system, while not for P*b*E, indicating a higher degree of local inhomogeneity in P*r*E solution, which might be due to the randomly distributed hydrophobic PO segments.

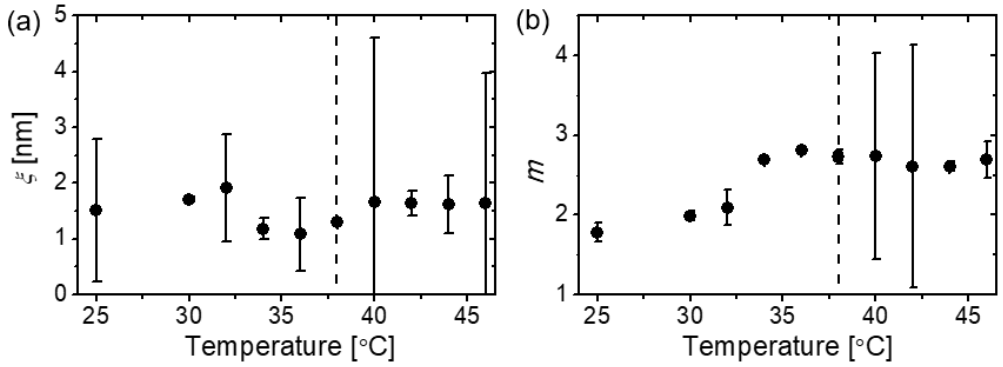

Figure 7.23 Structural parameters from the intensity fluctuation $I_{fluct}(q)$, using the modified Ornstein-Zernike structure factor, from 25 to 46 °C, obtained by modeling the SANS data of P*r*E solution at 20 g L^{-1} in D_2O. (a) Correlation length ξ. (b) Exponent m. The vertical dashed lines indicate T_{cp} of the solution.

Based on the SANS data analysis results, the structural evolution of P*r*E in aqueous solutions is constructed schematically in dependence on temperature, as shown in Figure 7.24. From room temperature to just below T_{cp}, the MBs undergo severe dehydration, where the collapse of the LCST side chains leads to a drastic deformation from a rod-like to a disk-like shape. At T_{cp}, the strongly dehydrated MBs agglomerate in small numbers to form spherical aggregates with a SLD gradient at their surface, creating a certain spatial order between the aggregates. Two degrees above T_{cp}, the MBs rearrange into slightly larger aggregates than before, showing still spatial order. Within the P*r*E aggregates, the MBs are only weakly connected to each other.

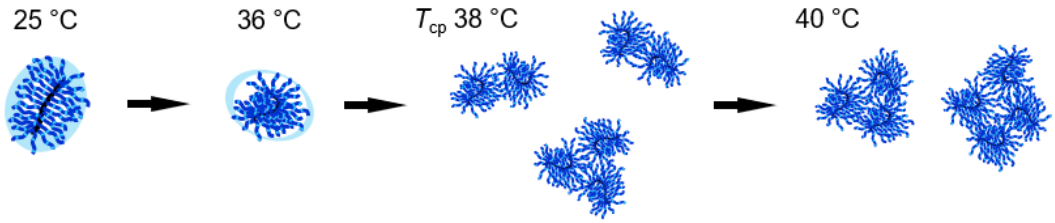

Figure 7.24 Schematic representation of the structural evolution of P*r*E in aqueous solutions, from room temperature to T_{cp} and further above. The black arrows indicate the heating process. The black, dark blue and light blue lines mark the backbone, the PO and the EO monomers, respectively. The bluish shading indicates the water-rich region.

7.7 Conclusion

The inner structure of two MBs having either PPO-*b*-PEO side chains or P(PO-*ran*-EO) side chains, called P*b*E and P*r*E, respectively, are investigated. The *cryo*-EM images are taken at low concentration, revealing the stretched conformation of the backbones for both kinds of the MBs. Using SANS, their inner structure at room temperature is studied in dilute and semi-dilute solutions. It is found that, both of the MBs feature a core-shell ellipsoid structure, with a polymer-rich core region and a water-rich shell region. Upon increasing concentration, the side chains of the MBs either rearrange or shrink to adapt to the limited space. For P*b*E, only the water-swollen PEO outer blocks are responsible for the adjustments; whereas for P*r*E, it is the full length of the P(PO-*ran*-EO) side chains that make the adjustments.

Next, the LCST behavior of P*b*E and P*r*E is investigated by their semi-dilute solutions. DLS data collected during a temperature scan show that T_{cp} of P*b*E solution (T_{cp} = 60 °C) is much higher than the one of P*r*E solution (T_{cp} = 38 °C). This is attributed to the side chain architecture of P*b*E, making the hydrophobic PO segments well-protected by the hydrophilic EO segments. The temperature-dependent structure is further resolved by SANS, giving hints to the dehydration process and the aggregation behavior. Upon heating toward the corresponding T_{cp}, the different side chain architecture, and thus the different distribution of the hydrophobic PO segments, leads to a weak dehydration of P*b*E, while a strong dehydration of P*r*E. Above T_{cp}, P*b*E are closely connected by their hydrated, mobile side chains, thereby forming large aggregates. On the contrary, due to the low water content and thus the lack of side chain mobility, P*r*E are loosely connected into small aggregates.

8. Summary and outlook

In the present thesis, molecular brushes (MBs) are studied in solution, focusing on their concentration-conformation dependence and their thermoresponsive behavior. Using small-angle X-ray/neutron scattering (SAXS/SANS), with complementary information from dynamic light scattering (DLS) and *cryo*-electron microscopy (*cryo*-EM), the structures of the MBs are resolved in detail, giving the structural evolution related to the variation of solution concentration or temperature.

Regarding the concentration effect on the MB conformation, in chapter 5, a chain-like MB (with long backbone and short side chains), P*i*POx$_{239}$-*g*-P*n*PrOx$_{14}$, is investigated in a good solvent. DLS and SAXS data were collected for the MB solutions from dilute to semi-dilute condition. The DLS data suggest that, the MBs perform purely translational diffusion in a wide concentration range (0.5 – 20 g L^{-1}), despite of their anisotropic overall shape. The SAXS data are model-fitted in the way that the mutual interaction between the MBs is related to the conformation of individual MBs, so that their interaction as well as the confirmation in semi-dilute regime can be precisely described, giving the structural parameters. In dilute solution, the MBs feature the structure of rigid linear polymers, having a large persistence length l_p and a large cross-section R_c. Upon increasing concentration, l_p decreases, meaning the backbones of the MBs soften as a result of the enhanced mutual interaction. In the semi-dilute regime, the radius of gyration R_g of the MB shows a scaling dependence on the solution concentration with an exponent of -0.8 ($R_g \sim c^{-0.8}$), which deviates from the theoretical prediction for solutions from linear polymers ($R_g \sim c^{-0.125}$). The result implies that the interaction between the MBs is significantly dominated by the side chain interactions, and this is missing for the linear polymers. Thus, our results show how far the conformation of chain-like MBs deviates from the conformation of linear polymers in dilute and semi-dilute solutions, and in which way the complex architecture affects the scaling exponent between the size and concentration in the semi-dilute regime. As a potential step of further studies on this project, a systematic investigation on how each architectural parameter (molar mass of the backbone/side chains, grafting density) affects the scaling relation between R_g and c can be delivered. From the obtained information, a comparison between the experimental results and the theoretical predictions [37, 38, 54] on the structural parameters (R_g, l_p and R_c) of MBs could provide a more complete picture.

As for the thermoresponsive behavior, MBs having LCST side chains are investigated in aqueous solution using SANS. In chapter 6, a MB with homopolymer side chains, P*i*POx$_{100}$-*g*-PEtOx$_{17}$, is investigated. While T_{cp} of the PEtOx$_{17}$ homopolymer is higher than 100 °C, the MB solution shows T_{cp} ~ 40.5 °C, which is attributed to the compact structure of the MB and the hydrophobic end groups on the side chains. At room temperature, the MBs are soluble, and found to feature a cylindrical shape. Upon heating towards T_{cp}, the MBs extend along the longitudinal direction, while above T_{cp}, they shrink again. It is supposed, that the dehydration of the LCST side chains leads to a gradual increase of the polymer density in the central part of the MB, resulting in an extension of the backbone, before the occurrence of an overall collapse above T_{cp}. Such two-step structural change has not been reported by previous studies on MBs with LCST side chains, where the MBs either have a chain-like shape or an ellipsoidal shape. Thus, our analysis results are attributed to the specific length ratio between the backbone and the side chains of the MB, P*i*POx$_{100}$-*g*-PEtOx$_{17}$, enabling an elongation of its shape at the beginning of the heating process.

For MBs with copolymer side chains, T_{cp} is furthermore dependent on the architecture of the side chains. To investigate this case, in chapter 7, the behavior of two MBs with copolymer side chains are compared, where the side chains are composed of poly(propylene oxide) (PPO, $T_{cp} \approx 8$ °C) and poly(ethylene oxide) (PEO, $T_{cp} > 100$ °C). In one of the MBs, called P*b*E, the two LCST polymers on the side chains are in block sequence; whereas in the other MB, called P*r*E, they are in random sequence. Although the PPO weight fraction in the two MBs is the same, i.e., 59 %, the T_{cp} of P*b*E (T_{cp} = 60 °C) is found to be significantly higher than the one of P*r*E (T_{cp} = 38 °C). The higher T_{cp} of P*b*E is supposed to be a result from the fact that the hydrophobic PPO blocks are attached to the backbone and are thus well-protected from the aqueous environment by the hydrophilic PEO blocks, which are at the periphery part of the MB. At room temperature, both kinds of the MBs feature a core-shell ellipsoidal structure, with a polymer-rich core and a water-rich shell. Upon heating, however, they show very different structural evolution, as a result from the different dehydration processes. During heating, for P*b*E, the PPO blocks stay hydrophobic, while the PEO blocks undergo a weak dehydration. Therefore, only a slight shrinkage of P*b*E is observed upon heating towards T_{cp}. Since a small amount of water is repelled out of P*b*E, a high water content is remained. This allows a high mobility of the side chains, which further facilitates the growth of large aggregates above T_{cp}. For P*r*E, the PO and EO monomers are randomly distributed, thus the MB shows an intermediate LCST property of the two components. Upon heating, the side chains severely

dehydrate, so water is mostly repelled out of the MBs, resulting in an overall collapse of the MBs at T_{cp}. Due to this drastic dehydration, the side chains of P*r*E feature low mobility and thus merely gather into small clusters above T_{cp}, lacking inter-connection between individual MBs. Our research suggests that the phase transition processes can be induced by choosing the appropriate side chain architecture, providing opportunities for a controllable thermoresponsive behavior. It is of interest to further investigate whether such a phenomenon is generally applicable to MBs with different LCST side chains. Thus, a possible extension of the work on this topic would be the examination on the phenomenon when the copolymer side chains are composed of other kinds of LCST polymers.

To summarize, MBs are polymers of complex architectures, and their physical properties in solutions are investigated in terms of the structural information. It is found that, from dilute to semi-dilute solutions, the chain-like MB shows a softening of its rigid main chain due to the significant side chain interaction. For the MBs with thermoresponsive segments, they feature rich structural behavior around the transition temperatures, which depends on the molecular architecture. These observations are revealed by the scattering methods, providing insight into structures on a wide range of length scales, and the *cryo*-electron microscopy give their real-space images which supports the findings.

Bibliography

[1] Bressler, I.; Kohlbrecher, J.; Thunemann, A. F. Sasfit: A Tool for Small-Angle Scattering Data Analysis Using a Library of Analytical Expressions. *J. Appl. Crystallogr.* **2015**, *48*, 1587-1598.

[2] Sheiko, S. S.; Sumerlin, B. S.; Matyjaszewski, K. Cylindrical Molecular Brushes: Synthesis, Characterization, and Properties. *Prog. Polym. Sci.* **2008**, *33*, 759-785.

[3] Yuan, J.; Müller, A. H. E.; Matyjaszewski, K.; Sheiko, S. S., 6.06 - Molecular Brushes. In *Polymer Science: A Comprehensive Reference*, Matyjaszewski, K., Möller, M., Eds. Elsevier: Amsterdam, 2012; pp 199-264.

[4] Verduzco, R.; Li, X.; Pesek, S. L.; Stein, G. E. Structure, Function, Self-Assembly, and Applications of Bottlebrush Copolymers. *Chem. Soc. Rev.* **2015**, *44*, 2405-2420.

[5] Tu, S.; Choudhury, C. K.; Luzinov, I.; Kuksenok, O. Recent Advances Towards Applications of Molecular Bottlebrushes and Their Conjugates. *Curr. Opin. Solid State Mater. Sci.* **2019**, *23*, 50-61.

[6] Li, Z.; Tang, M.; Liang, S.; Zhang, M.; Biesold, G. V.; He, Y.; Hao, S.; Choi, W.; Liu, Y.; Peng, J.; Lin, Z. Bottlebrush Polymers: From Controlled Synthesis, Self-Assembly, Properties to Applications. *Prog. Polym. Sci.* **2021**, 101387.

[7] Radzinski, S. C.; Foster, J. C.; Matson, J. B. Synthesis of Bottlebrush Polymers Via Transfer-to and Grafting-through Approaches Using a RAFT Chain Transfer Agent with a ROMP-Active Z-Group. *Polym. Chem.* **2015**, *6*, 5643-5652.

[8] Radzinski, S. C.; Foster, J. C.; Chapleski, R. C.; Troya, D.; Matson, J. B. Bottlebrush Polymer Synthesis by Ring-Opening Metathesis Polymerization: The Significance of the Anchor Group. *J. Am. Chem. Soc.* **2016**, *138*, 6998-7004.

[9] Yang, B.; Abel, B. A.; McCormick, C. L.; Storey, R. F. Synthesis of Polyisobutylene Bottlebrush Polymers Via Ring-Opening Metathesis Polymerization. *Macromolecules* **2017**, *50*, 7458-7467.

[10] Choinopoulos, I. Grubbs' and Schrock's Catalysts, Ring Opening Metathesis Polymerization and Molecular Brushes—Synthesis, Characterization, Properties and Applications. *Polymers* **2019**, *11*, 298-328.

[11] Johnson, J. A.; Lu, Y. Y.; Burts, A. O.; Xia, Y.; Durrell, A. C.; Tirrell, D. A.; Grubbs, R. H. Drug-Loaded, Bivalent-Bottle-Brush Polymers by Graft-through ROMP. *Macromolecules* **2010**, *43*, 10326-10335.

[12] Miki, K.; Kimura, A.; Oride, K.; Kuramochi, Y.; Matsuoka, H.; Harada, H.; Hiraoka, M.; Ohe, K. High-Contrast Fluorescence Imaging of Tumors in Vivo Using

Nanoparticles of Amphiphilic Brush-Like Copolymers Produced by ROMP. *Angew. Chem. Int. Ed.* **2011**, *50*, 6567-6570.

[13] Miyake, G. M.; Weitekamp, R. A.; Piunova, V. A.; Grubbs, R. H. Synthesis of Isocyanate-Based Brush Block Copolymers and Their Rapid Self-Assembly to Infrared-Reflecting Photonic Crystals. *J. Am. Chem. Soc.* **2012**, *134*, 14249-14254.

[14] Banquy, X.; Burdyńska, J.; Lee, D. W.; Matyjaszewski, K.; Israelachvili, J. Bioinspired Bottle-Brush Polymer Exhibits Low Friction and Amontons-Like Behavior. *J. Am. Chem. Soc.* **2014**, *136*, 6199-6202.

[15] Liberman-Martin, A. L.; Chu, C. K.; Grubbs, R. H. Application of Bottlebrush Block Copolymers as Photonic Crystals. *Macromol. Rapid Commun.* **2017**, *38*, 1700058.

[16] Mohammad, V.-V.; William, F. M. D., Jr.; Alexandr, P. Z.; Qiaoxi, L.; Benjamin, J. M.; Krzysztof, M.; Daniel, P. A.; Andrey, V. D.; Sergei, S. S.; Richard, J. S. In *Bottlebrush Elastomers: A Promising Molecular Engineering Route to Tunable, Prestrain-Free Dielectric Elastomers (Conference Presentation)*, Proc.SPIE, 2017.

[17] Vatankhah-Varnoosfaderani, M.; Daniel, W. F. M.; Zhushma, A. P.; Li, Q.; Morgan, B. J.; Matyjaszewski, K.; Armstrong, D. P.; Spontak, R. J.; Dobrynin, A. V.; Sheiko, S. S. Bottlebrush Elastomers: A New Platform for Freestanding Electroactuation. *Adv. Mater.* **2017**, *29*, 1604209.

[18] Abbasi, M.; Faust, L.; Wilhelm, M. Comb and Bottlebrush Polymers with Superior Rheological and Mechanical Properties. *Adv. Mater.* **2019**, *31*, e1806484.

[19] Xia, Y.; Adibnia, V.; Huang, R.; Murschel, F.; Faivre, J.; Xie, G.; Olszewski, M.; De Crescenzo, G.; Qi, W.; He, Z.; Su, R.; Matyjaszewski, K.; Banquy, X. Biomimetic Bottlebrush Polymer Coatings for Fabrication of Ultralow Fouling Surfaces. *Angew. Chem. Int. Ed.* **2019**, *58*, 1308-1314.

[20] Reynolds, V. G.; Mukherjee, S.; Xie, R.; Levi, A. E.; Atassi, A.; Uchiyama, T.; Wang, H.; Chabinyc, M. L.; Bates, C. M. Super-Soft Solvent-Free Bottlebrush Elastomers for Touch Sensing. *Mater. Horiz.* **2020**, *7*, 181-187.

[21] Kim, K. H.; Kim, M.; Moon, J.; Huh, J.; Bang, J. Bottlebrush Copolymer as Surface Neutralizer for Vertical Alignment of Block Copolymer Nanodomains in Thin Films. *ACS Macro Lett.* **2021**, 346-353.

[22] Ohnsorg, M. L.; Prendergast, P. C.; Robinson, L. L.; Bockman, M. R.; Bates, F. S.; Reineke, T. M. Bottlebrush Polymer Excipients Enhance Drug Solubility: Influence of End-Group Hydrophilicity and Thermoresponsiveness. *ACS Macro Lett.* **2021**, 375-381.

[23] Vohidov, F.; Milling, L. E.; Chen, Q.; Zhang, W.; Bhagchandani, S.; Nguyen, Hung V. T.; Irvine, D. J.; Johnson, J. A. ABC Triblock Bottlebrush Copolymer-Based Injectable Hydrogels: Design, Synthesis, and Application to Expanding the Therapeutic Index of Cancer Immunochemotherapy. *Chem. Sci.* **2020**, *11*, 5974-5986.

[24] Nese, A.; Lebedeva, N. V.; Sherwood, G.; Averick, S.; Li, Y.; Gao, H.; Peteanu, L.;

Sheiko, S. S.; Matyjaszewski, K. pH-Responsive Fluorescent Molecular Bottlebrushes Prepared by Atom Transfer Radical Polymerization. *Macromolecules* **2011**, *44*, 5905-5910.

[25] Yao, K.; Chen, Y.; Zhang, J.; Bunyard, C.; Tang, C. Cationic Salt-Responsive Bottle-Brush Polymers. *Macromol. Rapid Commun.* **2013**, *34*, 645-651.

[26] Kutnyánszky, E.; Hempenius, M. A.; Vancso, G. J. Polymer Bottlebrushes with a Redox Responsive Backbone Feel the Heat: Synthesis and Characterization of Dual Responsive Poly(Ferrocenylsilane)s with PNIPAM Side Chains. *Polym. Chem.* **2014**, *5*, 771-783.

[27] Lahasky, S. H.; Lu, L.; Huberty, W. A.; Cao, J.; Guo, L.; Garno, J. C.; Zhang, D. Synthesis and Characterization of Thermo-Responsive Polypeptoid Bottlebrushes. *Polym. Chem.* **2014**, *5*, 1418-1426.

[28] Bates, C. M.; Chang, A. B.; Momčilović, N.; Jones, S. C.; Grubbs, R. H. ABA Triblock Brush Polymers: Synthesis, Self-Assembly, Conductivity, and Rheological Properties. *Macromolecules* **2015**, *48*, 4967-4973.

[29] Paturej, J.; Sheiko, S. S.; Panyukov, S.; Rubinstein, M. Molecular Structure of Bottlebrush Polymers in Melts. *Sci. Adv.* **2016**, *2*, e1601478.

[30] Lin, T.-P.; Chang, A. B.; Luo, S.-X.; Chen, H.-Y.; Lee, B.; Grubbs, R. H. Effects of Grafting Density on Block Polymer Self-Assembly: From Linear to Bottlebrush. *ACS Nano* **2017**, *11*, 11632-11641.

[31] Sarapas, J. M.; Martin, T. B.; Chremos, A.; Douglas, J. F.; Beers, K. L. Bottlebrush Polymers in the Melt and Polyelectrolytes in Solution Share Common Structural Features. *Proc. Natl. Acad. Sci. U.S.A.* **2020**, *117*, 5168.

[32] Sunday, D. F.; Chremos, A.; Martin, T. B.; Chang, A. B.; Burns, A. B.; Grubbs, R. H. Concentration Dependence of the Size and Symmetry of a Bottlebrush Polymer in a Good Solvent. *Macromolecules* **2020**, *53*, 7132-7140.

[33] Bichler, K. J.; Jakobi, B.; Schneider, G. J. Dynamical Comparison of Different Polymer Architectures—Bottlebrush vs Linear Polymer. *Macromolecules* **2021**, *54*, 1829-1837.

[34] Starvaggi, H.; Tian, Y.; Liang, H.; Dobrynin, A. V. Bottlebrushes and Combs with Bimodal Distribution of the Side Chains: Diagram of States and Scattering Function. *Macromolecules* **2021**, *54*, 1818-1828.

[35] Sivokhin, A. P.; Orekhov, D. V.; Kazantsev, O. A.; Gubanova, O. V.; Kamorin, D. M.; Zarubina, I. S.; Bolshakova, E. A.; Zaitsev, S. D. Amphiphilic Thermoresponsive Copolymer Bottlebrushes: Synthesis, Characterization, and Study of Their Self-Assembly into Flower-Like Micelles. *Polym. J.* **2021**, *53*, 655-665.

[36] Kim, E. J.; Shin, J. J.; Do, T.; Lee, G. S.; Park, J.; Thapar, V.; Choi, J.; Bang, J.; Yi, G.-R.; Hur, S.-M.; Kim, J. G.; Kim, B. J. Molecular Weight Dependent Morphological Transitions of Bottlebrush Block Copolymer Particles: Experiments and Simulations.

ACS Nano **2021**, *15*, 5513-5522.

[37] Borisov, O. V.; Birshtein, T. M.; Zhulina, Y. B. The Temperature-Concentration Diagram of State for Solutions of Comb-Like Macromolecules. *Polym. Sci. (USSR)* **1987**, *29*, 1552-1559.

[38] Paturej, J.; Kreer, T. Hierarchical Excluded Volume Screening in Solutions of Bottlebrush Polymers. *Soft Matter* **2017**, *13*, 8534-8541.

[39] Bolisetty, S.; Airaud, C.; Xu, Y.; Müller, A. H. E.; Harnau, L.; Rosenfeldt, S.; Lindner, P.; Ballauff, M. Softening of the Stiffness of Bottle-Brush Polymers by Mutual Interaction. *Phys. Rev. E* **2007**, *75*, 040803.

[40] Bolisetty, S.; Rosenfeldt, S.; Rochette, C. N.; Harnau, L.; Lindner, P.; Xu, Y.; Müller, A. H. E.; Ballauff, M. Interaction of Cylindrical Polymer Brushes in Dilute and Semi-Dilute Solution. *Colloid Polym. Sci.* **2009**, *287*, 129-138.

[41] Yamamoto, S.-i.; Pietrasik, J.; Matyjaszewski, K. ATRP Synthesis of Thermally Responsive Molecular Brushes from Oligo(Ethylene Oxide) Methacrylates. *Macromolecules* **2007**, *40*, 9348-9353.

[42] Zhang, N.; Luxenhofer, R.; Jordan, R. Thermoresponsive Poly(2-Oxazoline) Molecular Brushes by Living Ionic Polymerization: Modulation of the Cloud Point by Random and Block Copolymer Pendant Chains. *Macromol. Chem. Phys.* **2012**, *213*, 1963-1969.

[43] Flory, P. J., *Principles of Polymer Chemistry*. Cornell University Press: Ithaca, 1953.

[44] De Gennes, P.-G., *Scaling Concepts in Polymer Physics*. Cornell university press: Ithaca, 1979.

[45] Rubinstein, M.; Colby, R. H., Polymer Solutions. In *Polymer Physics*, Oxford University Press: 2003; pp 171-196.

[46] Rubinstein, M.; Colby, R. H., Thermodynamics of Mixing. In *Polymer Physics*, Oxford University Press: 2003; pp 137-170.

[47] Aseyev, V.; Tenhu, H.; Winnik, F. M., Non-Ionic Thermoresponsive Polymers in Water. In *Self Organized Nanostructures of Amphiphilic Block Copolymers Ii. Advances in Polymer Science*, Müller, A., Borisov, O., Eds. Springer: Berlin, Heidelberg, 2010; Vol. 242, pp 29-89.

[48] Wu, C.; Wang, X. Globule-to-Coil Transition of a Single Homopolymer Chain in Solution. *Phys. Rev. Lett.* **1998**, *80*, 4092-4094.

[49] Tavagnacco, L.; Zaccarelli, E.; Chiessi, E. On the Molecular Origin of the Cooperative Coil-to-Globule Transition of Poly(*N*-Isopropylacrylamide) in Water. *Phys. Chem. Chem. Phys.* **2018**, *20*, 9997-10010.

[50] Zhang, Q.; Weber, C.; Schubert, U. S.; Hoogenboom, R. Thermoresponsive Polymers with Lower Critical Solution Temperature: From Fundamental Aspects and Measuring Techniques to Recommended Turbidimetry Conditions. *Mater. Horiz.* **2017**, *4*, 109-116.

[51] Denesyuk, N. A. Conformational Properties of Bottle-Brush Polymers. *Phys. Rev. E*

2003, *67*, 051803.

[52] Hsu, H. P.; Binder, K.; Paul, W. How to Define Variation of Physical Properties Normal to an Undulating One-Dimensional Object. *Phys. Rev. Lett.* **2009**, *103*, 198301.

[53] Panyukov, S. V.; Sheiko, S. S.; Rubinstein, M. Amplification of Tension in Branched Macromolecules. *Phys. Rev. Lett.* **2009**, *102*, 148301.

[54] Birshtein, T. M.; Borisov, O. V.; Zhulina, Y. B.; Khokhlov, A. R.; Yurasova, T. A. Conformations of Comb-Like Macromolecules. *Polym. Sci. (USSR)* **1987**, *29*, 1293-1300.

[55] Elli, S.; Ganazzoli, F.; Timoshenko, E. G.; Kuznetsov, Y. A.; Connolly, R. Size and Persistence Length of Molecular Bottle-Brushes by Monte Carlo Simulations. *J. Chem. Phys.* **2004**, *120*, 6257-6267.

[56] Feuz, L.; Leermakers, F. A. M.; Textor, M.; Borisov, O. Bending Rigidity and Induced Persistence Length of Molecular Bottle Brushes: A Self-Consistent-Field Theory. *Macromolecules* **2005**, *38*, 8891-8901.

[57] Yethiraj, A. A Monte Carlo Simulation Study of Branched Polymers. *J. Chem. Phys.* **2006**, *125*, 204901.

[58] Hsu, H.-P.; Paul, W.; Binder, K. Structure of Bottle-Brush Polymers in Solution: A Monte Carlo Test of Models for the Scattering Function. *J. Chem. Phys.* **2008**, *129*, 204904.

[59] Zhang, Z.; Carrillo, J.-M. Y.; Ahn, S.-k.; Wu, B.; Hong, K.; Smith, G. S.; Do, C. Atomistic Structure of Bottlebrush Polymers: Simulations and Neutron Scattering Studies. *Macromolecules* **2014**, *47*, 5808-5814.

[60] Angelescu, D. G.; Linse, P. Monte Carlo Simulations of Multigraft Homopolymers in Good Solvent. *Macromolecules* **2014**, *47*, 415-426.

[61] Chatterjee, D.; Vilgis, T. A. Scaling Laws of Bottle-Brush Polymers in Dilute Solutions. *Macromol. Theory Simul.* **2016**, *25*, 518-523.

[62] Dutta, S.; Wade, M. A.; Walsh, D. J.; Guironnet, D.; Rogers, S. A.; Sing, C. E. Dilute Solution Structure of Bottlebrush Polymers. *Soft Matter* **2019**, *15*, 2928-2941.

[63] Dutta, S.; Pan, T.; Sing, C. E. Bridging Simulation Length Scales of Bottlebrush Polymers Using a Wormlike Cylinder Model. *Macromolecules* **2019**, *52*, 4858-4874.

[64] Hsu, H.-P.; Paul, W.; Rathgeber, S.; Binder, K. Characteristic Length Scales and Radial Monomer Density Profiles of Molecular Bottle-Brushes: Simulation and Experiment. *Macromolecules* **2010**, *43*, 1592-1601.

[65] Rathgeber, S.; Pakula, T.; Wilk, A.; Matyjaszewski, K.; Lee, H.-i.; Beers, K. L. Bottle-Brush Macromolecules in Solution: Comparison between Results Obtained from Scattering Experiments and Computer Simulations. *Polymer* **2006**, *47*, 7318-7327.

[66] Zhang, B.; Gröhn, F.; Pedersen, J. S.; Fischer, K.; Schmidt, M. Conformation of Cylindrical Brushes in Solution: Effect of Side Chain Length. *Macromolecules* **2006**,

39, 8440-8450.

[67] Rathgeber, S.; Pakula, T.; Wilk, A.; Matyjaszewski, K.; Beers, K. L. On the Shape of Bottle-Brush Macromolecules: Systematic Variation of Architectural Parameters. *J. Chem. Phys.* **2005**, *122*, 124904.

[68] Hsu, H.-P.; Paul, W.; Binder, K. Understanding the Multiple Length Scales Describing the Structure of Bottle-Brush Polymers by Monte Carlo Simulation Methods. *Macromol. Theory Simul.* **2011**, *20*, 510-525.

[69] Maleki, H.; Theodorakis, P. E. Structure of Bottle-Brush Brushes under Good Solvent Conditions: A Molecular Dynamics Study. *J. Phys.: Condens. Matter* **2011**, *23*, 505104.

[70] Theodorakis, P. E.; Hsu, H.-P.; Paul, W.; Binder, K. Computer Simulation of Bottle-Brush Polymers with Flexible Backbone: Good Solvent Versus Theta Solvent Conditions. *J. Chem. Phys.* **2011**, *135*, 164903.

[71] Fredrickson, G. H. Surfactant-Induced Lyotropic Behavior of Flexible Polymer Solutions. *Macromolecules* **1993**, *26*, 2825-2831.

[72] Wintermantel, M.; Gerle, M.; Fischer, K.; Schmidt, M.; Wataoka, I.; Urakawa, H.; Kajiwara, K.; Tsukahara, Y. Molecular Bottlebrushes. *Macromolecules* **1996**, *29*, 978-983.

[73] Fytas, G.; Nothofer, H. G.; Scherf, U.; Vlassopoulos, D.; Meier, G. Structure and Dynamics of Nondilute Polyfluorene Solutions. *Macromolecules* **2002**, *35*, 481-488.

[74] Cheng, G.; Melnichenko, Y. B.; Wignall, G. D.; Hua, F.; Hong, K.; Mays, J. W. Small Angle Neutron Scattering Study of Conformation of Oligo(Ethylene Glycol)-Grafted Polystyrene in Dilute Solutions: Effect of the Backbone Length. *Macromolecules* **2008**, *41*, 9831-9836.

[75] Pesek, S. L.; Li, X.; Hammouda, B.; Hong, K.; Verduzco, R. Small-Angle Neutron Scattering Analysis of Bottlebrush Polymers Prepared Via Grafting-through Polymerization. *Macromolecules* **2013**, *46*, 6998-7005.

[76] Pesek, S. L.; Xiang, Q.; Hammouda, B.; Verduzco, R. Small-Angle Neutron Scattering Analysis of Bottlebrush Backbone and Side Chain Flexibility. *J. Polym. Sci., Part B: Polym. Phys.* **2017**, *55*, 104-111.

[77] Sunday, D. F.; Martin, T. B.; Chang, A. B.; Burns, A. B.; Grubbs, R. H. Addressing the Challenges of Modeling the Scattering from Bottlebrush Polymers in Solution. *J. Polym. Sci.* **2020**, *58*, 988-996.

[78] Harnau, L.; Reineker, P. Integral Equation Theory for Polyelectrolyte Solutions Containing Counterions and Coions. *J. Chem. Phys.* **1999**, *112*, 437-441.

[79] Harnau, L.; Costa, D.; Hansen, J. P. A Solvable Interaction Site Model for Lamellar Colloids. *EPL* **2001**, *53*, 729-734.

[80] Harnau, L. Influence of Intermolecular Interaction on the Dynamics of Good Solvent–Polymer Solutions. *J. Chem. Phys.* **2001**, *115*, 1943-1945.

[81] Harnau, L.; Hansen, J.-P. Colloid Aggregation Induced by Oppositely Charged Polyions. *J. Chem. Phys.* **2002**, *116*, 9051-9057.

[82] Rosenfeldt, S.; Dingenouts, N.; Ballauff, M.; Lindner, P.; Likos, C. N.; Werner, N.; Vögtle, F. Determination of the Structure Factor of Polymeric Systems in Solution by Small-Angle Scattering: A Sans-Study of a Dendrimer of Fourth Generation. *Macromol. Chem. Phys.* **2002**, *203*, 1995-2004.

[83] Li, L.; Harnau, L.; Rosenfeldt, S.; Ballauff, M. Effective Interaction of Charged Platelets in Aqueous Solution: Investigations of Colloid Laponite Suspensions by Static Light Scattering and Small-Angle X-Ray Scattering. *Phys. Rev. E* **2005**, *72*, 051504.

[84] Rosenfeldt, S.; Karpuk, E.; Lehmann, M.; Meier, H.; Lindner, P.; Harnau, L.; Ballauff, M. The Solution Structure of Stilbenoid Dendrimers: A Small-Angle Scattering Study. *Chemphyschem* **2006**, *7*, 2097-2104.

[85] Harnau, L.; Rosenfeldt, S.; Ballauff, M. Structure Factor and Thermodynamics of Rigid Dendrimers in Solution. *J. Chem. Phys.* **2007**, *127*, 014901.

[86] Sunday, D. F.; Martin, T. B.; Chang, A. B.; Burns, A. B.; Grubbs, R. H. Addressing the Challenges of Modeling the Scattering from Bottlebrush Polymers in Solution. *Journal of Polymer Science* **2020**, *58*, 988-996.

[87] Zhou, Y.; Tang, H.; Wu, P. Intra-Molecular Interactions Dominating the Dehydration of a Poly(2-Isopropyl-2-Oxazoline)-Based Densely Grafted Polymer Comb in Aqueous Solution and Hysteretic Liquid–Liquid Phase Separation. *Physical Chemistry Chemical Physics* **2017**, *19*, 6626-6635.

[88] Lin, P.; Clash, C.; Pearce, E. M.; Kwei, T. K.; Aponte, M. A. Solubility and Miscibility of Poly(Ethyl Oxazoline). *J. Polym. Sci., Part B: Polym. Phys.* **1988**, *26*, 603-619.

[89] Chen, F. P.; Ames, A. E.; Taylor, L. D. Aqueous Solutions of Poly(Ethyloxazoline) and Its Lower Consolute Phase Transition. *Macromolecules* **1990**, *23*, 4688-4695.

[90] Christova, D.; Velichkova, R.; Loos, W.; Goethals, E. J.; Prez, F. D. New Thermo-Responsive Polymer Materials Based on Poly(2-Ethyl-2-Oxazoline) Segments. *Polymer* **2003**, *44*, 2255-2261.

[91] Saraiva, A.; Persson, O.; Fredenslund, A. An Experimental Investigation of Cloud-Point Curves for the Poly(Ethylene Glycol)/Water System at Varying Molecular Weight Distributions. *Fluid Ph. Equilibria* **1993**, *91*, 291-311.

[92] Bekiranov, S.; Bruinsma, R.; Pincus, P. Solution Behavior of Polyethylene Oxide in Water as a Function of Temperature and Pressure. *Phys. Rev. E* **1997**, *55*, 577-585.

[93] Malcolm, G. N.; Rowlinson, J. S. The Thermodynamic Properties of Aqueous Solutions of Polyethylene Glycol, Polypropylene Glycol and Dioxane. *Trans. Faraday Society* **1957**, *53*, 921-931.

[94] Weber, C.; Rogers, S.; Vollrath, A.; Hoeppener, S.; Rudolph, T.; Fritz, N.; Hoogenboom, R.; Schubert, U. S. Aqueous Solution Behavior of Comb-Shaped Poly(2-Ethyl-2-

Oxazoline). *J. Polym. Sci., Part A: Polym. Chem.* **2013**, *51*, 139-148.

[95] Pamies, R.; Zhu, K.; Kjøniksen, A.-L.; Nyström, B. Thermal Response of Low Molecular Weight Poly-(*N*-Isopropylacrylamide) Polymers in Aqueous Solution. *Polym. Bull.* **2009**, *62*, 487-502.

[96] Halperin, A.; Kröger, M.; Winnik, F. M. Poly(*N*-Isopropylacrylamide) Phase Diagrams: Fifty Years of Research. *Angew. Chem. Int. Ed.* **2015**, *54*, 15342-15367.

[97] Li, C.; Gunari, N.; Fischer, K.; Janshoff, A.; Schmidt, M. New Perspectives for the Design of Molecular Actuators: Thermally Induced Collapse of Single Macromolecules from Cylindrical Brushes to Spheres. *Angew Chem Int Ed Engl* **2004**, *43*, 1101-1104.

[98] Li, X.; ShamsiJazeyi, H.; Pesek, S. L.; Agrawal, A.; Hammouda, B.; Verduzco, R. Thermoresponsive Pnipaam Bottlebrush Polymers with Tailored Side-Chain Length and End-Group Structure. *Soft Matter* **2014**, *10*, 2008-2015.

[99] Gromadzki, D.; Filippov, S.; Netopilík, M.; Makuška, R.; Jigounov, A.; Pleštil, J.; Horský, J.; Štěpánek, P. Combination of "Living" Nitroxide-Mediated and Photoiniferter-Induced "Grafting from" Free-Radical Polymerizations: From Branched Copolymers to Unimolecular Micelles and Microgels. *Eur. Polym. J.* **2009**, *45*, 1748-1758.

[100] Dalsin, S. J.; Hillmyer, M. A.; Bates, F. S. Molecular Weight Dependence of Zero-Shear Viscosity in Atactic Polypropylene Bottlebrush Polymers. *ACS Macro Lett.* **2014**, *3*, 423-427.

[101] Bejagam, K. K.; Singh, S. K.; Ahn, R.; Deshmukh, S. A. Unraveling the Conformations of Backbone and Side Chains in Thermosensitive Bottlebrush Polymers. *Macromolecules* **2019**, *52*, 9398-9408.

[102] Steinhauer, W.; Hoogenboom, R.; Keul, H.; Moeller, M. Block and Gradient Copolymers of 2-Hydroxyethyl Acrylate and 2-Methoxyethyl Acrylate Via RAFT: Polymerization Kinetics, Thermoresponsive Properties, and Micellization. *Macromolecules* **2013**, *46*, 1447-1460.

[103] Jaksch, S.; Schulz, A.; Kyriakos, K.; Zhang, J.; Grillo, I.; Pipich, V.; Jordan, R.; Papadakis, C. M. The Collapse and Aggregation of Thermoresponsive Poly(2-Oxazoline) Gradient Copolymers: A Time-Resolved Sans Study. *Colloid. Polym. Sci.* **2014**, *292*, 2413-2425.

[104] Filippov, S. K.; Verbraeken, B.; Konarev, P. V.; Svergun, D. I.; Angelov, B.; Vishnevetskaya, N. S.; Papadakis, C. M.; Rogers, S.; Radulescu, A.; Courtin, T.; Martins, J. C.; Starovoytova, L.; Hruby, M.; Stepanek, P.; Kravchenko, V. S.; Potemkin, I. I.; Hoogenboom, R. Block and Gradient Copoly(2-Oxazoline) Micelles: Strikingly Different on the Inside. *J. Phys. Chem. Lett.* **2017**, *8*, 3800-3804.

[105] Oleszko-Torbus, N.; Utrata-Wesołek, A.; Wałach, W.; Dworak, A. Solution Behavior of Thermoresponsive Random and Gradient Copolymers of 2-*N*-Propyl-2-Oxazoline. *Eur.*

Polym. J. **2017**, *88*, 613-622.

[106] Bozorg, M.; Hankiewicz, B.; Abetz, V. Solubility Behaviour of Random and Gradient Copolymers of Di- and Oligo(Ethylene Oxide) Methacrylate in Water: Effect of Various Additives. *Soft Matter* **2020**, *16*, 1066-1081.

[107] Wilfert, S.; Iturmendi, A.; Henke, H.; Brüggemann, O.; Teasdale, I. Thermoresponsive Polyphosphazene-Based Molecular Brushes by Living Cationic Polymerization. *Macromol. Symp.* **2014**, *337*, 116-123.

[108] Schulz, B.; Chudoba, R.; Heyda, J.; Dzubiella, J. Tuning the Critical Solution Temperature of Polymers by Copolymerization. *J. Chem. Phys.* **2015**, *143*, 243119.

[109] Liu, M.; Leroux, J.-C.; Gauthier, M. A. Conformation–Function Relationships for the Comb-Shaped Polymer Poegma. *Prog. Polym. Sci.* **2015**, *48*, 111-121.

[110] Pietrasik, J.; Sumerlin, B. S.; Lee, R. Y.; Matyjaszewski, K. Solution Behavior of Temperature-Responsive Molecular Brushes Prepared by ATRP. *Macromol. Chem. Phys.* **2007**, *208*, 30-36.

[111] Zhang, N.; Huber, S.; Schulz, A.; Luxenhofer, R.; Jordan, R. Cylindrical Molecular Brushes of Poly(2-Oxazoline)s from 2-Isopropenyl-2-Oxazoline. *Macromolecules* **2009**, *42*, 2215-2221.

[112] Huber, S.; Jordan, R. Modulation of the Lower Critical Solution Temperature of 2-Alkyl-2-Oxazoline Copolymers. *Colloid. Polym. Sci.* **2008**, *286*, 395-402.

[113] Hoogenboom, R. Poly(2-Oxazoline)s: A Polymer Class with Numerous Potential Applications. *Angew. Chem. Int. Ed.* **2009**, *48*, 7978-7994.

[114] Knop, K.; Hoogenboom, R.; Fischer, D.; Schubert, U. S. Poly(Ethylene Glycol) in Drug Delivery: Pros and Cons as Well as Potential Alternatives. *Angew. Chem. Int. Ed. Engl.* **2010**, *49*, 6288-6308.

[115] Barz, M.; Luxenhofer, R.; Zentel, R.; Vicent, M. J. Overcoming the PEG-Addiction: Well-Defined Alternatives to PEG, from Structure–Property Relationships to Better Defined Therapeutics. *Polym. Chem.* **2011**, *2*, 1900-1918.

[116] Luxenhofer, R.; Han, Y.; Schulz, A.; Tong, J.; He, Z.; Kabanov, A. V.; Jordan, R. Poly(2-Oxazoline)s as Polymer Therapeutics. *Macromol. Rapid Commun.* **2012**, *33*, 1613-1631.

[117] Luxenhofer, R.; Huber, S.; Hytry, J.; Tong, J.; Kabanov, A. V.; Jordan, R. Chiral and Water-Soluble Poly(2-Oxazoline)s. *J. Polym. Sci., Part A: Polym. Chem.* **2013**, *51*, 732-738.

[118] de la Rosa, V. R. Poly(2-Oxazoline)s as Materials for Biomedical Applications. *J. Mater. Sci.: Mater. Med* **2014**, *25*, 1211-1225.

[119] Jerca, F. A.; Jerca, V. V.; Anghelache, A. M.; Vuluga, D. M.; Hoogenboom, R. Poly(2-Isopropenyl-2-Oxazoline) as a Versatile Platform Towards Thermoresponsive Copolymers. *Polymer Chemistry* **2018**, *9*, 3473-3478.

[120] Lorson, T.; Lübtow, M. M.; Wegener, E.; Haider, M. S.; Borova, S.; Nahm, D.; Jordan,

R.; Sokolski-Papkov, M.; Kabanov, A. V.; Luxenhofer, R. Poly(2-Oxazoline)s Based Biomaterials: A Comprehensive and Critical Update. *Biomaterials* **2018**, *178*, 204-280.

[121] Hoogenboom, R.; Thijs, H. M. L.; Jochems, M. J. H. C.; van Lankvelt, B. M.; Fijten, M. W. M.; Schubert, U. S. Tuning the Lcst of Poly(2-Oxazoline)s by Varying Composition and Molecular Weight: Alternatives to Poly(*N*-Isopropylacrylamide)? *Chem. Commun.* **2008**, 5758-5760.

[122] Weber, C.; Becer, C. R.; Hoogenboom, R.; Schubert, U. S. Lower Critical Solution Temperature Behavior of Comb and Graft Shaped Poly[Oligo(2-Ethyl-2-Oxazoline)Methacrylate]s. *Macromolecules* **2009**, *42*, 2965-2971.

[123] Kowalczuk, A.; Kronek, J.; Bosowska, K.; Trzebicka, B.; Dworak, A. Star Poly(2-Ethyl-2-Oxazoline)s—Synthesis and Thermosensitivity. *Polym. Int.* **2011**, *60*, 1001-1009.

[124] Filippov, A.; Tarabukina, E.; Kudryavtseva, A.; Fatullaev, E.; Kurlykin, M.; Tenkovtsev, A. Molecular Brushes with Poly-2-Ethyl-2-Oxazoline Side Chains and Aromatic Polyester Backbone Manifesting Double Stimuli Responsiveness. *Colloid Polym. Sci.* **2019**, *297*, 1445-1454.

[125] Zhou, Y.; Tang, H.; Wu, P. Intra-Molecular Interactions Dominating the Dehydration of a Poly(2-Isopropyl-2-Oxazoline)-Based Densely Grafted Polymer Comb in Aqueous Solution and Hysteretic Liquid–Liquid Phase Separation. *Phys. Chem. Chem. Phys.* **2017**, *19*, 6626-6635.

[126] Log P Value for the Tert-Butyloxycarbonyl End Group. http://www.molbase.com/en/synthesis_57260-71-6-moldata-1516172.html (Accessed Jun 5, 2020)

[127] Mountrichas, G.; Pispas, S. Novel Double Hydrophilic Block Copolymers Based on Poly(*para*-Hydroxystyrene) Derivatives and Poly(Ethylene Oxide). *J. Polym. Sci., Part A: Polym. Chem.* **2007**, *45*, 5790-5799.

[128] Armstrong, J.; Chowdhry, B.; O'Brien, R.; Beezer, A.; Mitchell, J.; Leharne, S. Scanning Microcalorimetric Investigations of Phase Transitions in Dilute Aqueous Solutions of Poly(Oxypropylene). *J. Phys. Chem.* **1995**, *99*, 4590-4598.

[129] Saeki, S.; Kuwahara, N.; Nakata, M.; Kaneko, M. Upper and Lower Critical Solution Ttemperatures in Poly(Ethylene Glycol) Solutions. *Polymer* **1976**, *17*, 685-689.

[130] Zhao, J.; Mountrichas, G.; Zhang, G.; Pispas, S. Thermoresponsive Core−Shell Brush Copolymers with Poly(Propylene Oxide)-*block*-Poly(Ethylene Oxide) Side Chains Via a “Grafting from” Technique. *Macromolecules* **2010**, *43*, 1771-1777.

[131] Zhao, J.; Zhang, G.; Pispas, S. Thermoresponsive Brush Copolymers with Poly(Propylene Oxide-*ran*-Ethylene Oxide) Side Chains Via Metal-Free Anionic Polymerization “Grafting from” Technique. *J. Polym. Sci., Part A: Polym. Chem.* **2010**, *48*, 2320-2328.

[132] Alexandridis, P.; Alan Hatton, T. Poly(Ethylene Oxide)-Poly(Propylene Oxide)-

Poly(Ethylene Oxide) Block Copolymer Surfactants in Aqueous Solutions and at Interfaces: Thermodynamics, Structure, Dynamics, and Modeling. *Colloids Surf. A Physicochem. Eng. Asp.* **1995**, *96*, 1-46.

[133] Batrakova, E. V.; Kabanov, A. V. Pluronic Block Copolymers: Evolution of Drug Delivery Concept from Inert Nanocarriers to Biological Response Modifiers. *J. Control. Release* **2008**, *130*, 98-106.

[134] Kadam, Y.; Yerramilli, U.; Bahadur, A.; Bahadur, P. Micelles from PEO–PPO–PEO Block Copolymers as Nanocontainers for Solubilization of a Poorly Water Soluble Drug Hydrochlorothiazide. *Colloids Surf. B* **2011**, *83*, 49-57.

[135] Pitto-Barry, A.; Barry, N. P. E. Pluronic® Block-Copolymers in Medicine: From Chemical and Biological Versatility to Rationalisation and Clinical Advances. *Polym. Chem.* **2014**, *5*, 3291-3297.

[136] Schulz, A.; Jaksch, S.; Schubel, R.; Wegener, E.; Di, Z.; Han, Y.; Meister, A.; Kressler, J.; Kabanov, A. V.; Luxenhofer, R.; Papadakis, C. M.; Jordan, R. Drug-Induced Morphology Switch in Drug Delivery Systems Based on Poly(2-Oxazoline)s. *ACS nano* **2014**, *8*, 2686-2696.

[137] Jaksch, S.; Schulz, A.; Di, Z.; Luxenhofer, R.; Jordan, R.; Papadakis, C. M. Amphiphilic Triblock Copolymers from Poly(2-Oxazoline) with Different Hydrophobic Blocks: Changes of the Micellar Structures Upon Addition of a Strongly Hydrophobic Cancer Drug. *Macromol. Chem. Phys.* **2016**, *217*, 1448-1456.

[138] Kripotou, S.; Psylla, C.; Kyriakos, K.; Raftopoulos, K. N.; Zhao, J.; Zhang, G.; Pispas, S.; Papadakis, C. M.; Kyritsis, A. Structure and Crystallization Behavior of Poly(Ethylene Oxide) (PEO) Chains in Core–Shell Brush Copolymers with Poly(Propylene Oxide)-*block*-Poly(Ethylene Oxide) Side Chains. *Macromolecules* **2016**, *49*, 5963-5977.

[139] Brown, W., Data Analysis in Dynamic Light Scattering. In *Dynamic Light Scattering : The Method and Some Applications*, Clarendon Press: Oxford 1993.

[140] Štěpánek, P., Data Analysis in Dynamic Light Scattering. In *Dynamic Light Scattering: The Method and Some Applications (Monographs on the Physics and Chemistry of Materials)*, Brown, W., Ed. Clarendon Press: New York, 1993; pp 177–241.

[141] Frisken, B. J. Revisiting the Method of Cumulants for the Analysis of Dynamic Light-Scattering Data. *Appl. Opt.* **2001**, *40*, 4087-4091.

[142] Pecora, R. Doppler Shifts in Light Scattering from Pure Liquids and Polymer Solutions. *J. Chem. Phys.* **1964**, *40*, 1604-1614.

[143] Pecora, R. Doppler Shifts in Light Scattering. II. Flexible Polymer Molecules. *J. Chem. Phys.* **1965**, *43*, 1562-1564.

[144] Bruce J. Berne, R. P., *Dynamic Light Scattering: With Applications to Chemistry, Biology, and Physics*. Dover Publications: New York, 2000.

[145] Schmidt, M.; Stockmayer, W. H. Quasi-Elastic Light Scattering by Semiflexible Chains. *Macromolecules* **1984**, *17*, 509-514.

[146] Burchard, W.; Schmidt, M.; Stockmayer, W. H. Information on Polydispersity and Branching from Combined Quasi-Elastic and Intergrated Scattering. *Macromolecules* **1980**, *13*, 1265-1272.

[147] Burchard, W. In *Static and Dynamic Light Scattering from Branched Polymers and Biopolymers*, Light Scattering from Polymers, Berlin, Heidelberg, Springer Berlin Heidelberg: Berlin, Heidelberg, 1983; pp 1-124.

[148] Galinsky, G.; Burchard, W. Starch Fractions as Examples for Nonrandomly Branched Macromolecules. 4. Angular Dependence in Dynamic Light Scattering. *Macromolecules* **1997**, *30*, 6966-6973.

[149] Glatter, O., Modern Methods of Data Analysis in Small-Angle Scattering and Light Scattering. In *Modern Aspects of Small-Angle Scattering*, Brumberger, H., Ed. 1995; pp 107-180.

[150] Roe, R.-J., Small Angle Scattering. In *Methods of X-Ray and Neutron Scattering in Polymer Science*, Oxford University Press: , 2000; pp 155-210.

[151] Pedersen, J. S., Modelling of Small-Angle Scattering Data from Colloids and Polymer Systems. In *Neutron, X-Rays and Light. Scattering Methods Applied to Soft Condensed Matter*, Lindner, P. a. Z., Th., Ed. North Holland: 2002; pp 391-420.

[152] Svergun, D. I.; Koch, M. H. J. Small-Angle Scattering Studies of Biological Macromolecules in Solution. *Rep. Prog. Phys.* **2003**, *66*, 1735-1782.

[153] Feigin, L. A.; Svergun, D. I., *Structure Analysis by Small-Angle X-Ray and Neutron Scattering*. Springer: 1987.

[154] Fritz, G.; Bergmann, A. Saxs Instruments with Slit Collimation: Investigation of Resolution and Flux. *J. Appl. Cryst.* **2006**, *39*, 64-71.

[155] Hammouda, B. Multidisk Neutron Velocity Selectors. *Nuclear Instruments and Methods in Physics Research Section A* **1992**, *321*, 275-283.

[156] Barker, J. G.; Pedersen, J. S. Instrumental Smearing Effects in Radially Symmetric Small-Angle Neutron Scattering by Numerical and Analytical Methods. *J. Appl. Cryst.* **1995**, *28*, 105-114.

[157] Stieger, M.; Pedersen, J. S.; Lindner, P.; Richtering, W. Are Thermoresponsive Microgels Model Systems for Concentrated Colloidal Suspensions? A Rheology and Small-Angle Neutron Scattering Study. *Langmuir* **2004**, *20*, 7283-7292.

[158] Kotlarchyk, M.; Chen, S. H. Analysis of Small Angle Neutron Scattering Spectra from Polydisperse Interacting Colloids. *J. Chem. Phys.* **1983**, *79*, 2461-2469.

[159] Berr, S. S. Solvent Isotope Effects on Alkytrimethylammonium Bromide Micelles as a Function of Alkyl Chain Length. *J. Phys. Chem.* **1987**, *91*, 4760-4765.

[160] Onsager, L. The Effects of Shape on the Interaction of Colloidal Particles. *Ann. N. Y.*

Acad. Sci. **1949**, *51*, 627-659.

[161] Fournet, G. Ùtude Théorique Et Expérimentale De La Diffusion Des Rayons X Par Les Ensembles Denses De Particules. *Bull. Soc. Fr. Mineral. Cristallogr.* **1951**, *74*, 37-172.

[162] Pedersen, J. S. Analysis of Small-Angle Scattering Data from Colloids and Polymer Solutions: Modeling and Least-Squares Fitting. *Adv. Colloid Interface Sci.* **1997**, *70*, 171-210.

[163] Pedersen, J. S.; Schurtenberger, P. Scattering Functions of Semiflexible Polymers with and without Excluded Volume Effects. *Macromolecules* **1996**, *29*, 7602-7612.

[164] Pedersen, J. S.; Laso, M.; Schurtenberger, P. Monte Carlo Study of Excluded Volume Effects in Wormlike Micelles and Semiflexible Polymers. *Phys. Rev. E* **1996**, *54*, R5917-R5920.

[165] Chen, W.-R.; Butler, P. D.; Magid, L. J. Incorporating Intermicellar Interactions in the Fitting of Sans Data from Cationic Wormlike Micelles. *Langmuir* **2006**, *22*, 6539-6548.

[166] Percus, J. K.; Yevick, G. J. Analysis of Classical Statistical Mechanics by Means of Collective Coordinates. *Phys. Rev.* **1958**, *110*, 1-13.

[167] Jerke, G.; Pedersen, J. S.; Egelhaaf, S. U.; Schurtenberger, P. Static Structure Factor of Polymerlike Micelles: Overall Dimension, Flexibility, and Local Properties of Lecithin Reverse Micelles in Deuterated Isooctane. *Phys. Rev. E* **1997**, *56*, 5772-5788.

[168] Jerke, G.; Pedersen, J. S.; Egelhaaf, S. U.; Schurtenberger, P. Flexibility of Charged and Uncharged Polymer-Like Micelles. *Langmuir* **1998**, *14*, 6013-6024.

[169] Garamus, V. M.; Pedersen, J. S.; Kawasaki, H.; Maeda, H. Scattering from Polymerlike Micelles of TDAO in Salt/Water Solutions at Semidilute Concentrations. *Langmuir* **2000**, *16*, 6431-6437.

[170] Cannavacciuolo, L.; Sommer, C.; Pedersen, J. S.; Schurtenberger, P. Size, Flexibility, and Scattering Functions of Semiflexible Polyelectrolytes with Excluded Volume Effects: Monte Carlo Simulations and Neutron Scattering Experiments. *Phys. Rev. E* **2000**, *62*, 5409-5419.

[171] Cannavacciuolo, L.; Pedersen, J. S.; Schurtenberger, P. Monte Carlo Simulation Study of Concentration Effects and Scattering Functions for Polyelectrolyte Wormlike Micelles. *Langmuir* **2002**, *18*, 2922-2932.

[172] Cannavacciuolo, L.; Pedersen, J. S.; Schurtenberger, P. Single-Coil Properties and Concentration Effects for Polyelectrolyte-Like Wormlike Micelles: A Monte Carlo Study. *J. Phys. Condens. Matter* **2002**, *14*, 2283-2295.

[173] Sommer, C.; Pedersen, J. S.; Egelhaaf, S. U.; Cannavacciuolo, L.; Kohlbrecher, J.; Schurtenberger, P. Wormlike Micelles as "Equilibrium Polyelectrolytes": Light and Neutron Scattering Experiments. *Langmuir* **2002**, *18*, 2495-2505.

[174] Pedersen, J. S.; Schurtenberger, P. Scattering Functions of Semidilute Solutions of Polymers in a Good Solvent. *J. Polym. Sci., Part B: Polym. Phys.* **2004**, *42*, 3081-3094.

[175] Hammouda, B. A New Guinier-Porod Model. *J. Appl. Crystallogr.* **2010**, *43*, 716-719.
[176] Koberstein, J. T.; Morra, B.; Stein, R. S. The Determination of Diffuse-Boundary Thicknesses of Polymers by Small-Angle X-Ray Scattering. *J. Appl. Crystallogr.* **1980**, *13*, 34-45.
[177] Schmidt, P. W. Interpretation of Small-Angle Scattering Curves Proportional to a Negative Power of the Scattering Vector. *J. Appl. Crystallogr.* **1982**, *15*, 567-569.
[178] Hammouda, B.; Ho, D. L.; Kline, S. Insight into Clustering in Poly(Ethylene Oxide) Solutions. *Macromolecules* **2004**, *37*, 6932-6937.
[179] Hammouda, B.; Ho, D. L. Insight into Chain Dimensions in PEO/Water Solutions. *J. Polym. Sci., Part B: Polym. Phys.* **2007**, *45*, 2196-2200.
[180] Blanchet, C. E.; Spilotros, A.; Schwemmer, F.; Graewert, M. A.; Kikhney, A.; Jeffries, C. M.; Franke, D.; Mark, D.; Zengerle, R.; Cipriani, F.; Fiedler, S.; Roessle, M.; Svergun, D. I. Versatile Sample Environments and Automation for Biological Solution X-Ray Scattering Experiments at the P12 Beamline (Petra III, Desy). *J. Appl. Crystallogr.* **2015**, *48*, 431-443.
[181] Round, A.; Felisaz, F.; Fodinger, L.; Gobbo, A.; Huet, J.; Villard, C.; Blanchet, C. E.; Pernot, P.; McSweeney, S.; Roessle, M.; Svergun, D. I.; Cipriani, F. Biosaxs Sample Changer: A Robotic Sample Changer for Rapid and Reliable High-Throughput X-Ray Solution Scattering Experiments. *Acta Crystallogr. D* **2015**, *71*, 67-75.
[182] Franke, D.; Kikhney, A. G.; Svergun, D. I. Automated Acquisition and Analysis of Small Angle X-Ray Scattering Data. *Nucl. Instrum. Methods Phys. Res* **2012**, *689*, 52-59.
[183] Heinz Maier-Leibnitz Zentrum; Frielinghaus, H.; Feoktystov, A. V.; Berts, I.; Mangiapia, G. KWS-1: Small-Angle Scattering Diffractometer. *Journal of large-scale research facilities* **2015**, *1*, A28.
[184] Feoktystov, A. V.; Frielinghaus, H.; Di, Z.; Jaksch, S.; Pipich, V.; Appavou, M.-S.; Babcock, E.; Hanslik, R.; Engels, R.; Kemmerling, G.; Kleines, H.; Ioffe, A.; Richter, D.; Bruckel, T. KWS-1 High-Resolution Small-Angle Neutron Scattering Instrument at JCNS: Current State. *J. Appl. Crystallogr.* **2015**, *48*, 61-70.
[185] Sasview 4.2.2. http://www.sasview.org/ (Accessed March 01, 2020).
[186] Manalastas-Cantos, K.; Konarev, P. V.; Hajizadeh, N. R.; Kikhney, A. G.; Petoukhov, M. V.; Molodenskiy, D. S.; Panjkovich, A.; Mertens, H. D. T.; Gruzinov, A.; Borges, C.; Jeffries, C. M.; Svergun, D. I.; Franke, D. ATSAS 3.0: Expanded Functionality and New Tools for Small-Angle Scattering Data Analysis. *J. Appl. Crystallogr.* **2021**, *54*, 343-355.
[187] Milne, J. L. S.; Borgnia, M. J.; Bartesaghi, A.; Tran, E. E. H.; Earl, L. A.; Schauder, D. M.; Lengyel, J.; Pierson, J.; Patwardhan, A.; Subramaniam, S. *Cryo*-Electron Microscopy--a Primer for the Non-Microscopist. *FEBS J.* **2013**, *280*, 28-45.
[188] *Cryo*-Electron Microscopy. What It Is, How It Works, Pros and Cons.

https://www.microscopemaster.com/cryo-electron-microscopy.html (Accessed Mar 15, 2021)

[189] Peplow, M. *Cryo*-Electron Microscopy Reaches Resolution Milestone. *ACS Cent. Sci.* **2020**, *6*, 1274-1277.

[190] Williams, R. E. A.; McComb, D. W.; Subramaniam, S. *Cryo*-Electron Microscopy Instrumentation and Techniques for Life Sciences and Materials Science. *MRS Bull.* **2019**, *44*, 929-934.

[191] Kimanius, D.; Forsberg, B. O.; Scheres, S. H. W.; Lindahl, E. Accelerated *Cryo*-EM Structure Determination with Parallelisation Using Gpus in Relion-2. *eLife* **2016**, *5*, e18722.

[192] Zivanov, J.; Nakane, T.; Forsberg, B. O.; Kimanius, D.; Hagen, W. J. H.; Lindahl, E.; Scheres, S. H. W. New Tools for Automated High-Resolution *Cryo*-EM Structure Determination in Relion-3. *eLife* **2018**, *7*, e42166.

[193] Zheng, S. Q.; Palovcak, E.; Armache, J.-P.; Verba, K. A.; Cheng, Y.; Agard, D. A. Motioncor2: Anisotropic Correction of Beam-Induced Motion for Improved *Cryo*-Electron Microscopy. *Nat. Methods* **2017**, *14*, 331-332.

[194] Schindelin, J.; Arganda-Carreras, I.; Frise, E.; Kaynig, V.; Longair, M.; Pietzsch, T.; Preibisch, S.; Rueden, C.; Saalfeld, S.; Schmid, B.; Tinevez, J.-Y.; White, D. J.; Hartenstein, V.; Eliceiri, K.; Tomancak, P.; Cardona, A. Fiji: An Open-Source Platform for Biological-Image Analysis. *Nat. Methods* **2012**, *9*, 676-682.

[195] Banc, A.; Charbonneau, C.; Dahesh, M.; Appavou, M. S.; Fu, Z.; Morel, M. H.; Ramos, L. Small Angle Neutron Scattering Contrast Variation Reveals Heterogeneities of Interactions in Protein Gels. *Soft Matter* **2016**, *12*, 5340-5352.

[196] Mortensen, K., Structural Studies of Polymer Systems Using Small-Angle Neutron Scattering. In *Advanced Functional Molecules and Polymers Vol 2: Processing and Spectroscopy*, Nalwa, H. S., Ed. Gordon & Breach Science Publ.: 2001; pp 223-269.

[197] Streitwieser, A.; Heathcock, C. H.; Kosower, E. M.; Corfield, P. J., *Introduction to Organic Chemistry*. Macmillan New York: 1992.

[198] Tande, B. M.; Wagner, N. J.; Mackay, M. E.; Hawker, C. J.; Jeong, M. Viscosimetric, Hydrodynamic, and Conformational Properties of Dendrimers and Dendrons. *Macromolecules* **2001**, *34*, 8580-8585.

[199] Viebke, C.; Williams, P. A. The Influence of Temperature on the Characterization of Water-Soluble Polymers Using Asymmetric Flow Field-Flow-Fractionation Coupled to Multiangle Laser Light Scattering. *Anal. Chem.* **2000**, *72*, 3896-3901.

[200] Ford, N.; Havard, T.; Wallace, P., Analysis of Macromolecules Using Low- and Right-Angle Laser Light Scattering and Photon Correlation Spectroscopy. In *Particle Size Distribution III*, American Chemical Society: 1998; Vol. 693, pp 39-51.

[201] Tsvetkov, V. N., *Rigid-Chain Polymers: Hydrodynamic and Optical Properties in*

Solution. Springer US: New York: Plenum., 1989; p 502.

[202] Amirova, A. I.; Golub, O. V.; Kirila, T. U.; Razina, A. B.; Tenkovtsev, A. V.; Filippov, A. P. Influence of Arm Length and Number on Star-Shaped Poly(2-Isopropyl-2-Oxazoline) Aggregation in Aqueous Solutions near Cloud Point. *Soft Mater.* **2016**, *14*, 15-26.

[203] Grube, M.; Leiske, M. N.; Schubert, U. S.; Nischang, I. POx as an Alternative to PEG? A Hydrodynamic and Light Scattering Study. *Macromolecules* **2018**, *51*, 1905-1916.

[204] Simonova, M. A.; Tarasova, E. V.; Dudkina, M. M.; Tenkovtsev, A. V.; Filippov, A. P. Synthesis and Hydrodynamic and Conformation Properties of Star-Shaped Polystyrene with Calix[8]Arene Core. *Int. J. Polym. Anal. Charact.* **2019**, *24*, 87-95.

[205] Benoit, H. D., P. Light Scattering from Non-Gaussian Chains. *J. Phys. Chem.* **1953**, *57*, 958– 963.

[206] Kang, J.-J.; Shehu, K.; Sachse, C.; Jung, F. A.; Ko, C.-H.; Barnsley, L. C.; Jordan, R.; Papadakis, C. M. A Molecular Brush with Thermoresponsive Poly(2-Ethyl-2-Oxazoline) Side Chains: A Structural Investigation. *Colloid Polym. Sci.* **2021**, *299*, 193-203.

[207] Jakeš, J.; Štěpánek, P. Positive Exponential Sum Method of Inverting Laplace Transform Applied to Photon Correlation Spectroscopy. *Czech. J. Phys.* **1990**, *40*, 972-983.

[208] Jakeš, J. Regularized Positive Exponential Sum (REPES) Program - a Way of Inverting Laplace Transform Data Obtained by Dynamic Light Scattering. *Collect. Czech. Chem. Commun.* **1995**, *60*, 1781–1797.

[209] Pesek, S. L.; Xiang, Q.; Hammouda, B.; Verduzco, R. Small-Angle Neutron Scattering Analysis of Bottlebrush Backbone and Side Chain Flexibility. *J. Polym. Sci., Part B: Polym. Phys.* **2017**, *55*, 104-111.

[210] Dyakonova, M. A.; Gotzamanis, G.; Niebuur, B.-J.; Vishnevetskaya, N. S.; Raftopoulos, K. N.; Di, Z.; Filippov, S. K.; Tsitsilianis, C.; Papadakis, C. M. pH Responsiveness of Hydrogels Formed by Telechelic Polyampholytes. *Soft Matter* **2017**, *13*, 3568-3579.

[211] Vishnevetskaya, N. S.; Hildebrand, V.; Niebuur, B.-J.; Grillo, I.; Filippov, S. K.; Laschewsky, A.; Müller-Buschbaum, P.; Papadakis, C. M. "Schizophrenic" Micelles from Doubly Thermoresponsive Polysulfobetaine-*b*-Poly(*N*-Isopropylmethacrylamide) Diblock Copolymers. *Macromolecules* **2017**, *50*, 3985-3999.

[212] Kang, J.-J.; Jung, F. A.; Ko, C.-H.; Shehu, K.; Barnsley, L. C.; Kohler, F.; Dietz, H.; Zhao, J.; Pispas, S.; Papadakis, C. M. Thermoresponsive Molecular Brushes with Propylene Oxide/Ethylene Oxide Copolymer Side Chains in Aqueous Solution. *Macromolecules* **2020**, *53*, 4068-4081.

[213] Nelson, A.; Cosgrove, T. Small-Angle Neutron Scattering Study of Adsorbed Pluronic Tri-Block Copolymers on Laponite. *Langmuir* **2005**, *21*, 9176-9182.

[214] Israelachvili, J. N.; Mitchell, D. J.; Ninham, B. W. Theory of Self-Assembly of

Hydrocarbon Amphiphiles into Micelles and Bilayers. *J. Chem. Soc. Faraday Trans. 2* **1976**, *72*, 1525-1568.

[215] Ganguly, R.; Choudhury, N.; Aswal, V. K.; Hassan, P. A. Pluronic L64 Micelles near Cloud Point: Investigating the Role of Micellar Growth and Interaction in Critical Concentration Fluctuation and Percolation. *J. Phys. Chem. B* **2009**, *113*, 668-675.

[216] Tanaka, H. Appearance of a Moving Droplet Phase and Unusual Networklike or Spongelike Patterns in a Phase-Separating Polymer Solution with a Double-Well-Shaped Phase Diagram. *Macromolecules* **1992**, *25*, 6377-6380.

[217] Tanaka, H. Viscoelastic Phase Separation. *J. Phys. Condens. Matter* **2000**, *12*, R207-R264.

[218] Niebuur, B.-J.; Claude, K.-L.; Pinzek, S.; Cariker, C.; Raftopoulos, K. N.; Pipich, V.; Appavou, M.-S.; Schulte, A.; Papadakis, C. M. Pressure-Dependence of Poly(*N*-Isopropylacrylamide) Mesoglobule Formation in Aqueous Solution. *ACS Macro Lett.* **2017**, *6*, 1180-1185.

Scientific contributions

Publications related to this thesis.

- Kang, J.-J.; Jung, F. A.; Ko, C.-H.; Shehu, K.; Barnsley, L. C.; Kohler, F.; Dietz, H.; Zhao, J.; Pispas, S.; Papadakis, C. M. Thermoresponsive Molecular Brushes with Propylene Oxide/Ethylene Oxide Copolymer Side Chains in Aqueous Solution. *Macromolecules* **2020**, *53*, 4068-4081
- Kang, J.-J.; Shehu, K.; Sachse, C.; Jung, F. A.; Ko, C.-H.; Barnsley, L. C.; Jordan, R.; Papadakis, C. M. A Molecular Brush with Thermoresponsive Poly(2-Ethyl-2-Oxazoline) Side Chains: A Structural Investigation. *Colloid Polym. Sci* **2021**, *299*, 193-203

Further publications.

- Jung, F. A.; Panteli, P. A.; Ko, C.-H.; Kang, J.-J.; Barnsley, L. C.; Tsitsilianis, C.; Patrickios, C. S.; Papadakis, C. M. Structural Properties of Micelles formed by Telechelic Pentablock Quaterpolymers with pH-responsive Midblocks and Thermo-responsive End Blocks in Aqueous Solution. *Macromolecules* **2019**, *52*, 9746-9758
- Adams F.; Pehl, T. M.; Kränzlein, M.; Kernbichl, S. A.; Kang, J.-J.; Papadakis, C. M.; Rieger, B. (Co)Polymerization of (−)-Menthide and β-Butyrolactone with Yttrium-Bis(Phenolates): Tuning Material Properties of Sustainable Polyesters. *Polym. Chem.* **2020**, *11*, 4426-4437
- Ko, C.-H.; Claude, K.-L.; Niebuur, B.-J.; Jung, F. A.; Kang, J.-J.; Schanzenbach, D.; Frielinghaus, H.; Barnsley, L. C.; Wu, B.; Pipich, V.; Schulte, A.; Müller-Buschbaum, P.; Laschewsky, A.; Papadakis, C. M. Temperature-Dependent Phase Behavior of the Thermoresponsive Polymer Poly(*N*-isopropylmethacrylamide) in an Aqueous Solution. *Macromolecules* **2020**, *53*, 6816-6827

Conference talks.

- S. Xia, C.-H. Ko, J.-J. Kang
  Dynamic Light Scattering and Fluorescence Correlation Spectroscopy: Theoretical Background, Instrument Operation and Data Analysis
  Polymer Physics Summer School, Obertauern, 12 – 15 June 2018

- J.-J. Kang, F. A. Jung, C.-H. Ko, K. Shehu, L. C. Barnsley, F. Kohler, H. Dietz, J. Zhao, S. Pispas, C. M. Papadakis
  Morphology of Thermoresponsive Molecular Brushes with Copolymer Side Arms in Aqueous Solution
  DPG Spring Meeting, Regensburg, 31 Mar – 05 April 2019.
- J.-J. Kang, D. Gieseler, C.-H. Ko, L. C. Barnsley, R. Jordan, C. M. Papadakis
  Structural Investigation on PTX-loaded Poly(2-Oxazoline) Molecular Brushes
  4th Internal Biannual Science Meeting of the MLZ, Grainau, 24 – 27 June 2019

Conference poster presentations.

- J.-J. Kang, J. Zhao, S. Pispas, C. M. Papadakis
  Morphology of Amphiphilic Molecular Brushes in Dilute Aqueous Solution
  DPG Spring Meeting, Berlin, 11 – 16 March 2018
- J.-J. Kang, J. Zhao, H. Frielinghaus, L. C. Barnsley, S. Pispas, C. M. Papadakis
  Morphology of Thermoresponsive Molecular Brushes with Copolymer Side Arms in Dilute Aqueous Solutions
  32th European Colloid and Interface Society Conference, Ljubljana, 2 – 7 September 2018
- J.-J. Kang, J. Zhao, H. Frielinghaus, L. C. Barnsley, S. Pispas, C. M. Papadakis
  Morphology of Thermoresponsive Molecular Brushes with Copolymer Side Arms in Dilute Aqueous Solutions
  4th German SNI Conference, Garching, 17 – 19 September 2018
- J.-J. Kang, J. Zhao, H. Frielinghaus, L. C. Barnsley, S. Pispas, C. M. Papadakis
  Morphology of Thermoresponsive Molecular Brushes with Copolymer Side Arms in Dilute Aqueous Solutions
  12th Hellenic Polymer Society International Conference 2018, Ioannina, 30 September – 3 Octpber 2018
- J.-J. Kang, D. Gieseler, C.-H. Ko, L. C. Barnsley, R. Jordan, C. M. Papadakis
  PTX-loaded Poly(2-Oxazoline) Molecular Brushes: A Structural Investigation
  French-German Opportunities of Cooperation to Fact the European Revolution in Neutron Science, Garching, 14 – 16 May 2019
- J.-J. Kang, F. A. Jung, C.-H. Ko, K. Shehu, L. C. Barnsley, F. Kohler, H. Dietz, J. Zhao, S. Pispas, C. M. Papadakis

Morphology of Thermoresponsive Molecular Brushes with PPO-PEO Copolymer Side Arms in Aqueous Solution

European Polymer Congress, Crete, 9 – 14 June 2019

- J.-J. Kang, D. Gieseler, C.-H. Ko, L. C. Barnsley, R. Jordan, C. M. Papadakis
  Drug-Loaded Poly(2-Oxazoline) Molecular Brushes: A Structural Investigation
  Kolloid-Tagung ”Complex Fluids”/49th Conference of the German Colloid Society, Stuttgart, 23 – 25 September 2019
- J.-J. Kang, D. Gieseler, C.-H. Ko, L. C. Barnsley, R. Jordan, C. M. Papadakis
  Drug-Loaded Poly(2-Oxazoline) Molecular Brushes: A Structural Investigation
  MLZ User Meeting 2019, Munich, 10 – 11 December 2019
- J.-J. Kang, C. Sachse, C.-H. Ko, M.A. Schroer, S. Da Vela, J. Kohlbrecher, R. Jordan, C.M. Papadakis
  Concentration-Conformation Relation of A Poly(2-Oxazoline)-Based Bottlebrush Polymer in Good Solvent
  EMBL Hamburg P12 Virtual User Meeting, 17 – 18 November 2020
- J.-J. Kang, F. A. Jung, C.-H. Ko, K. Shehu, L. C. Barnsley, F. Kohler, H. Dietz, J. Zhao, S. Pispas, C. M. Papadakis
  Dehydration of Thermoresponsive Molecular Brushes with Block or Random Copolymer Side Chains
  MLZ User Meeting 2020, 08 – 09 December 2020
- J.-J. Kang, C. Sachse, J. Allwang, C.-H. Ko, M. A. Schroer, S. Da Vela, D. Molodenskiy, J. Kohlbrecher, R. Jordan, C. M. Papadakis
  Concentration-Conformation Relation of A Poly(2-Oxazoline)-Based Bottlebrush Polymer in Good Solvent
  DESY Photon Science Users´ Meeting, 25 – 29 January 2021

Acknowledgements

In this final chapter, I would like to express my gratitude to the people who have provided help and support to me during my PhD. Without them, I would not have been able to proceed my work fluently and get the achievements.

First of all, I want to thank Prof. Christine M. Papadakis for being my supervisor. With her guidance and useful advises, I was able to deliver my work in a well-structured way and present it in an organized manner, for both scientific writing as well as oral presentations. Also, she provided me the opportunities to perform measurements at the big facilities and to attend conferences worldwide, which are precious experiences and nice trainings for my PhD.

My project was based on the MBs provided by the research groups of Dr. Pispas and Prof. Jordan. Special thanks to Dr. Junpeng Zhao, Dr. Clemens Sachse and Dr. Dan Gieseler who performed the polymer synthesis. The synthesis and the subsequent characterization were professionally done and clearly explained, so that I could work on a solid base. Besides, they are open for scientific discussion, and willing to feedback on my analysis results, from which I have gained fruitful opinions. I would like to thank Dr. Erik Wegener and Sarah Naumann from Prof. Jordan's group, who have joined the meeting and discussion on MBs and kindly contributed their point of view.

Beamline scientists were playing important roles in the success of all my measurements in the large-scale facilities, i.e., the neutron source and the synchrotron radiation source. The SANS measurements at the instrument KWS-1 at MLZ were supported by Dr. Lester C. Barnsley; and the SAXS measurements at beamline P12 at DESY were supported by Dr. Martin A. Schroer, Dr. Stefano Da Vela and Dr. Dmitry Molodenskiy. With their excellent work, the measurements were carried out efficiently. I also would like to thank them for their advises on the data reduction as well as the analysis of the SAS data.

For the bachelor students and working students I have supervised, Michael Ziemba, Michele Lecis and Johannes Allwang, I am thankful for their efforts in the projects and the nice work they have finally achieved. We have had numerous discussions on the details of the experiments, the analysis methods and the interpretation of those experimental results, which are inspiring and full of insights from time to time.

During my PhD, I am deeply thankful for the accompany by all my colleagues in the Soft Matter Physic Group: Dr. Xiaohan Zhang, Dr. Geethu P. Meledam, Dr. Bart-Jan Niebuur, Dr.

Florian A. Jung, Chia-Hsin Ko, Yanan Li, Kaltrina Shehu, Shu-Hsien Huang and Bahar Yazdanshenas, with whom I have shared lots of good memories. These include the joint works in the labs, the cooperation during the beamtime, the city-tours during the conferences, the routine burger-meets in the campus canteen, the nice meals (and drinks) in restaurants, our cooking times, the sporty activities and the countless conversations we have had in the daily office time, scientific or non-scientific. The weekly on-line coffee break with B-J, Florian and Chia-Hsin is definitely a warm company during the home office period and the final stage of the PhD. I will always cherish the joyful moments with them.

It is a great pleasure to join the E13 family with the colleagues of the Chair of Functional Materials. Though the names are too many to list here, I would like to thank everyone for creating the friendly and energetic working atmosphere. Special appreciation to Prof. Peter Müller-Buschbaum for being a very nice group leader and my official mentor. For the organization of the group activities and the administration-related arrangements, many thanks Mrs. Carola Kappauf and Mrs. Marion Waletzki for their nice work and kind help.

Last but not least, I want to express my gratitude to my parents, my sister and my friends in Taiwan, who provide consistent support and have full confidence in me. My boyfriend, Ting-Hui Hsieh, is also someone being there for me all along. I feel very lucky to have their love.